

**MASSACHUSETTS INSTITUTE OF TECHNOLOGY  
LINCOLN LABORATORY**

**SOLID STATE RESEARCH**

**QUARTERLY TECHNICAL REPORT**

**1 MAY — 31 JULY 1989**

**ISSUED 2 FEBRUARY 1990**

**Approved for public release; distribution is unlimited.**

**LEXINGTON**

**MASSACHUSETTS**

## ABSTRACT

This report covers in detail the research work of the Solid State Division at Lincoln Laboratory for the period 1 May through 31 July 1989. The topics covered are Electrooptical Devices, Quantum Electronics, Materials Research, Submicrometer Technology, Microelectronics, and Analog Device Technology. Funding is provided primarily by the Air Force, with additional support provided by the Army, DARPA, Navy, SDIO, NASA, and DOE.



Accession For	
NTIS GRA&I	<input checked="checked" type="checkbox"/>
DTIC TAB	<input type="checkbox"/>
Unannounced	<input type="checkbox"/>
Justification	
By	
Distribution/	
Availability Codes	
Dist	Avail and/or Special
A-1	

# TABLE OF CONTENTS

Abstract	iii
List of Illustrations	vii
Introduction	xiii
Reports on Solid State Research	xv
Organization	xxv

↓  
Partial contents:

1. ELECTROOPTICAL DEVICES	1
1.1 High-Performance Optical Analog Link Using External Modulation,	1
1.2 1-Gb/s Free-Space Optical Interconnection Between Digital Circuits, and	3
1.3 Mass-Transported Buried-Heterostructure GaAs Lasers;	5
2. QUANTUM ELECTRONICS	9
2.1 Single-Frequency Nd:YAG Laser,	9
2.2 Laser Pumping of Solid-State Amplifiers Using Random Binary-Phase Plates,	10
2.3 Passively Mode-Locked $\text{Ti:Al}_2\text{O}_3$ Laser Using a Nonlinear Coupled Cavity, and	13
2.4 Picosecond Nondegenerate Four-Wave Mixing in Semiconductor Waveguides;	15
3. MATERIALS RESEARCH	21
3.1 Total-Dose Radiation Effects on PtSi Schottky-Barrier Infrared Detectors and Focal Plane Arrays;	21
4. SUBMICROMETER TECHNOLOGY	27
4.1 Aluminum Oxides as Imaging Materials for 193-nm Excimer-Laser Lithography,	27
4.2 Planarizing a-C:H and $\text{SiO}_2$ Films Prepared by Bias Electron Cyclotron Resonance Plasma Deposition, and	30
4.3 Electrical, Crystallographic, and Optical Properties of ArF-Laser-Modified Diamond Surfaces;	34
5. MICROELECTRONICS	39
5.1 CCD Camera Developed for Wavefront-Sensor Applications,	39
5.2 Surface-State Dark-Current Suppression in CCDs, and	42
5.3 Permeable Base Transistor Track-and-Hold Circuits; and	45

## LIST OF ILLUSTRATIONS

Figure No.		Page
1-1	Block diagram of the optical analog link.	1
1-2	Performance of the optical analog link with 55-mW optical power input and 10-Hz noise bandwidth. The uncertainty in the noise level measurement is $\pm 2$ dB. Solid lines are theoretical predictions based on the nonlinearity of the interferometric modulator.	2
1-3	Schematic circuit of experimental free-space optical interconnection system. The interconnect consists of a diode laser, two miniature lenses, and a detector.	4
1-4	Upper trace: output from GaAs digital circuit connected directly to detector. Lower trace: 1-Gb/s electrical drive signal to laser on another circuit board separated from detector by 24 cm. Scale: 1 V/div vertical; 2 ns/div horizontal.	5
1-5	Relative light output vs forward current for mass-transported BH GaInP/GaAs/GaInP laser with $\sim 1\text{-}\mu\text{m}$ active-layer width and $\sim 400\text{-}\mu\text{m}$ length.	6
2-1	Sketch of the single-frequency Nd:YAG laser. The Nd:YAG crystal has a curved end ( $R = 1$ cm) with a dichroic coating that is a high reflector at $1.06\text{ }\mu\text{m}$ and transmits the pump radiation at 808 nm. The other end of the crystal is antireflection (AR) coated at $1.06\text{ }\mu\text{m}$ . The output coupler has a radius of curvature of 7.5 cm and a 90-percent reflectivity at $1.06\text{ }\mu\text{m}$ .	9
2-2	Geometry used for pumping amplifiers using transmissive random binary-phase plates. A lens of focal length $f$ is used to produce the far-field intensity distribution within the crystal.	11
2-3	Contour plot of the central peak of the far-field intensity distribution for diffraction from a square aperture. At the $1/e^2$ intensity points, the contour can be approximated by a circle of diameter $D$ shown by the dashed line.	12
2-4	Beam smoothing using a random binary-phase plate with $100\text{-}\mu\text{m}$ square elements. The intensity profile of an unsmoothed beam is shown in (a), and of a smoothed beam is shown in (b). The upper figures are density plots where the highest intensity is shown by the darkest regions; the lower figures are 3-dimensional plots of the same profiles. The large spatial variation shown in (a) is replaced by speckle as shown in (b).	13

## LIST OF ILLUSTRATIONS (Continued)

Figure No.		Page
2-5	Schematic of the passively mode-locked Ti:Al <sub>2</sub> O <sub>3</sub> laser system. The four mirrors around the Ti:Al <sub>2</sub> O <sub>3</sub> crystal constitute the main laser cavity. The mirror M <sub>0</sub> is a 15-percent transmitting mirror. The second cavity consists of the mirror M <sub>0</sub> , a beam splitter (BS) that acts as the output coupler, a GRIN lens to focus light into the optical fiber, and a butt-coupled mirror.	14
2-6	(a) Experimental configuration, (b) a CARS process in which the material is excited at $\omega_1 - \omega_2$ , and (c) a two-photon process in which the material is excited at $2\omega_1$ .	16
2-7	(a) $2\omega_1 - \omega_2$ signal as a function of the time delay between $\omega_1$ and $\omega_2$ pulses. $\hbar\omega_1$ is kept fixed at 1480.7 meV, and $\omega_2$ is varied. (b) Time-integrated $2\omega_1 - \omega_2$ signal vs detuning energy $\hbar(\omega_1 - \omega_2)$ . Curve TM: all waves are in TM modes; curve TE: pump beam $\omega_1$ is in TE mode, $\omega_2$ and $2\omega_1 - \omega_2$ are in TM. The arrows mark the most visible Maker fringes.	17
2-8	Optically induced change in the absorption of probe beam as a function of probe photon energy. The pump frequency is kept fixed as indicated by the arrow. Inset shows the percent change in throughput power of the probe beam as a function of pump-probe time delay.	18
3-1	(a) Forward and (b) reverse current-voltage characteristics of PtSi detector at 80 K before irradiation (solid lines) and after irradiation of 10 Mrad(Si) (dashed lines).	22
3-2	Normalized responsivity vs wavelength for PtSi detector at 80 K before and after irradiation. The normalized responsivity is the ratio of the signal from the PtSi detector to the signal from a pyroelectric detector with a flat spectral response, normalized to the highest measured value of this ratio.	22
3-3	High-frequency C-V characteristics of MOS capacitors at 80 K before irradiation (solid lines) and after irradiation of 1 Mrad(Si) (dashed lines). The gate voltage $V_G$ applied to the capacitors during irradiation and the flat-band voltage shift $\Delta V_{FB}$ are indicated.	23
3-4	CCD transfer inefficiency as a function of total dose for the serial CCD shift register of a $160 \times 244$ array.	24
3-5	Thermal images of 10-K 4-bar test pattern obtained with a $160 \times 244$ PtSi array (a) before irradiation, and after irradiation to a total dose of (b) 0.2 and (c) 0.4 Mrad(Si).	26

## LIST OF ILLUSTRATIONS (Continued)

Figure No.		Page
4-1	Atomic compositions of $\text{AlO}_x$ obtained from Auger measurements as a function of the ratio of oxygen to Al arrival rates. The data include films formed by ion-beam deposition, e-beam evaporation, and sputter deposition. The shaded area represents films that contain a mixture of Al and oxide; these provide good imaging quality at 193 nm.	28
4-2	One-pulse self-development threshold energy $E_{th}$ and reflectivity of ion-beam-deposited $\text{AlO}_x$ films as a function of the partial pressure of $\text{O}_2$ during deposition.	29
4-3	Scanning electron micrograph of $\text{AlO}_x$ on top of a-C:H. The $\text{AlO}_x$ layer was patterned in air with one pulse of $528 \text{ mJ/cm}^2$ using a 193-nm excimer laser. The a-C:H layer was reactive-ion etched in $\text{O}_2$ at 250 V.	30
4-4	Sequence of cross-sectional scanning electron micrographs showing the change in planarization with aspect ratio for an a-C:H film deposited on oxide substrates with step height of (a) 0.34, (b) 0.63, and (c) $0.92 \mu\text{m}$ .	31
4-5	Cross-sectional scanning electron micrographs of planarizing oxides deposited on $0.9\text{-}\mu\text{m}$ silicon steps of varying aspect ratio for three different deposition conditions. For all three films, the ECR power was 750 W and the silane flow was 100 sccm. In (a), the RF power was 300 W, the $\text{N}_2\text{O}$ flow rate was 72 sccm, the Ar flow rate was 58 sccm, and the deposition time was 90 min. In (b), the RF power was increased to 400 W, the Ar flow rate was increased to 87 sccm, and the deposition time was halved to 45 min. In (c), the RF power and Ar flow rate were identical to those in (a), but the $\text{N}_2\text{O}$ flow rate and deposition time were halved to 36 sccm and 45 min, respectively.	32
4-6	Conductance of the modified diamond layer on $\{100\}$ -oriented substrates in the low resistance direction as a function of etch depth. Ion-beam-assisted etching was used to etch the modified layer. The inset shows the typical resistance of the layer as a function of angle relative to one of the in-plane $\langle 110 \rangle$ axes. The solid circles are the data, and the solid lines are guides to the eye.	34
4-7	Ratio of the maximum to minimum transmittance of linearly polarized radiation through the modified layer on $\{100\}$ substrates as a function of photon energy and wavelength. The solid circles are the data, and the solid line is a guide to the eye.	35

## LIST OF ILLUSTRATIONS (Continued)

Figure No.		Page
4-8	Bright- and dark-field transmission electron micrographs of laser-modified $\{100\}$ diamond. The inset in the bright-field micrograph shows the electron diffraction pattern and the portion of that pattern used to form the dark-field image. Transmission electron micrographs of the unmodified diamond used in these experiments show no defects except for a very occasional dislocation.	36
5-1	Photograph of the CCD camera showing the focal-plane board on the left and camera chassis on the right. Both front and back views of the focal-plane board are shown.	39
5-2	Quantum efficiency vs wavelength for the $64 \times 64$ -pixel CCD imager for both back and front illumination.	40
5-3	Configuration of the Hartman sensor.	41
5-4	Tilt noise vs photons per subaperture of the Hartman sensor using the CCD camera.	42
5-5	Normalized surface-state generation rate vs surface-state energy in the forbidden gap for various values of time after the surface is switched from inversion to depletion. Energy is measured from the valence-band edge.	44
5-6	Measured and calculated dark current from a three-phase CCD imager vs time that one phase spends in depletion with the remaining two phases in inversion.	45
5-7	Basic track-and-hold circuit.	46
5-8	Track-and-hold waveforms.	47
5-9	Schematic of track-and-hold circuit H2.	48
5-10	(a) Track-and-hold circuit H2 in cryogenic test fixture, and (b) closeup of H2.	50
5-11	Tracking bandwidth of circuit H2 in sampling mode.	51
5-12	Spectrum-analyzer data for circuit H2.	51
6-1	Relative dielectric constant as a function of frequency for $\text{LaAlO}_3$ and $\text{LaGaO}_3$ measured at 4.2 K with a stripline resonator.	54

## LIST OF ILLUSTRATIONS (Continued)

Figure No.		Page
6-2	Dielectric loss tangent as a function of frequency for $\text{LaAlO}_3$ and $\text{LaGaO}_3$ measured at 4.2 K with a stripline resonator.	54
6-3	Photograph taken in transmitted light of a (100)-oriented $\text{LaGaO}_3$ substrate showing the twin planes perpendicular to the substrate surface.	55
6-4	Schematic of multitarget cosputtering system for deposition of superconducting $\text{Y}_1\text{Ba}_2\text{Cu}_3\text{O}_x$ films.	56
6-5	Resistivity vs temperature ( $\rho$ vs $T$ ) curve for Y-Ba-Cu-O film deposited at a substrate temperature of $680^\circ\text{C}$ . The semiconductor-like trend above the transition is attributed to the presence of the $\text{Y}_2\text{Ba}_1\text{Cu}_1\text{O}_5$ "green" phase.	57
6-6	$\rho$ vs $T$ curve for a Y-Ba-Cu-O film deposited at $600^\circ\text{C}$ .	58
6-7	$\rho$ vs $T$ curve for a Y-Ba-Cu-O film deposited at $460^\circ\text{C}$ . Lower substrate temperatures prevent the formation of unwanted phases.	58
6-8	$J_c$ and $\rho$ vs $T$ curves for a Y-Ba-Cu-O film deposited at $495^\circ\text{C}$ . $J_c \approx 10^6 \text{ A/cm}^2$ at 4 K.	59
6-9	Critical oxygen partial pressure for the decomposition of the perovskite structure. The horizontal line marks the maximum oxygen pressure tolerable for sputtering from elemental Ba and Y targets. (Adapted from Reference 7.)	60



## INTRODUCTION

### 1. ELECTROOPTICAL DEVICES

A high-dynamic-range fiber-optic analog link has been built with a noise figure of only 6 dB and an RF-to-RF gain of 11 dB at 50 MHz. This was achieved without electronic amplification by using a very sensitive bandpass impedance-matched Ti:LiNbO<sub>3</sub> interferometric modulator and an input optical power of 55 mW at 1.32  $\mu\text{m}$ .

A simple free-space optical interconnect containing only a laser, two miniature lenses, and a detector has linked two GaAs digital integrated circuits at a data rate of 1 Gb/s. The link demonstrates the feasibility of directly connecting digital circuits at high data rates with no external driver, preamplifier or interface circuitry.

A new type of GaAs diode laser has been demonstrated. The laser consists of an OMVPE-grown GaInP/GaAs double heterostructure with buried stripes produced by mass transport of the GaInP alloy.

### 2. QUANTUM ELECTRONICS

A standing-wave Nd:YAG laser has been demonstrated to operate at a single frequency at pump powers up to three times threshold with no frequency-selective devices in the cavity. Single-frequency operation occurs even though the 8.5-cm-long cavity has of the order of 100 axial modes within the gain peak.

Transmissive random binary-phase plates have been fabricated using standard microlithographic techniques. The plates have been used to smooth out large-scale spatial variations ("hot spots") in frequency-doubled Nd:YAG laser beams (532 nm) used for pumping Ti:Al<sub>2</sub>O<sub>3</sub> amplifiers.

A Ti:Al<sub>2</sub>O<sub>3</sub> laser has been passively mode locked with the use of a second, coupled cavity containing an optical fiber that produced self-phase modulation. The output was an 80-MHz train of chirped 1.5-ps pulses which were dispersively compensated with an external grating pair to obtain 220-fs pulses.

Nonresonant, nondegenerate four-wave mixing in an AlGaAs waveguide has been observed using picosecond laser pulses. A conversion efficiency of 0.4 percent was obtained with an intensity of  $2 \times 10^8 \text{ W/cm}^2$  which, for the waveguide area of  $2 \mu\text{m}^2$ , corresponds to 20 pJ in the 5-ps laser pulse.

### 3. MATERIALS RESEARCH

Total-dose radiation testing has been performed at 80 K on PtSi Schottky-barrier infrared detectors and on  $160 \times 244$ -element focal plane arrays with monolithic CCD readout circuitry. The detectors showed excellent radiation hardness, with essentially no change in dark current and quantum efficiency after exposure to 5 Mrad(Si), and the focal plane arrays continued to operate after exposure to 0.8 Mrad(Si), yielding thermal imagery of reasonable quality with small degradation in pixel uniformity.

#### 4. SUBMICROMETER TECHNOLOGY

Substoichiometric aluminum oxide thin films have been investigated as imaging layers for 193-nm excimer lithography. Features as small as  $0.1\ \mu\text{m}$  were obtained in single-pulse, self-developing exposures.

The method of bias electron cyclotron resonance plasma deposition has been used to deposit planarizing layers of amorphous carbon or  $\text{SiO}_2$  near room temperature. With both materials,  $1\text{-}\mu\text{m}$ -high,  $2\text{-}\mu\text{m}$ -wide features are planarized to  $<50\ \text{nm}$ .

Pulsed, 193-nm irradiation has been shown to modify the electrical, optical, and crystallographic properties of diamond surfaces, apparently by inducing the formation of graphite-like phases in the diamond matrix. The modified layers have resistivity in the  $10^{-4}\ \Omega\ \text{cm}$  range, polarize light, and are thermally and chemically stable.

#### 5. MICROELECTRONICS

Charge-coupled-device (CCD) cameras have been built for use in a wavefront sensor in a real-time adaptive optics system. The cameras satisfied the dual requirements of low noise level at high frame rates (35 electrons rms at 2000 f/s) and near-reflection-limited quantum efficiency (88 percent).

The surface-state dark current in a buried-channel CCD has been suppressed by periodically inverting the surfaces under the gates as a function of time during the integration period. The dark current at room temperature was reduced to as low as  $20\ \text{pA}/\text{cm}^2$ .

A permeable-base transistor (PBT) track-and-hold circuit has been developed that is designed to operate with high- $T_c$  superconductors in a chirp-transform spectrum analyzer. A microstrip hybrid circuit using discrete PBTs has demonstrated a tracking bandwidth of 2.4 GHz with over 30 dB of dynamic range.

#### 6. ANALOG DEVICE TECHNOLOGY

Dielectric properties of the perovskites  $\text{LaAlO}_3$  and  $\text{LaGaO}_3$  have been measured at microwave frequencies and the results indicate that both materials can be utilized as low-loss substrates for high-temperature superconductors. The structural instabilities and twin formation inherent in these perovskites should not prevent fabrication of thin-film superconductor circuits.

Superconducting films of  $\text{Y}_1\text{Ba}_2\text{Cu}_3\text{O}_x$  cosputtered from elemental targets of Y, Ba, and Cu in an  $\text{Ar}/\text{O}_2$  ambient and crystallized by annealing in  $\text{O}_2$  at  $850^\circ\text{C}$  have shown transition temperatures exceeding 80 K and critical currents of  $\sim 10^6\ \text{A}/\text{cm}^2$ . Higher oxygen pressure during sputtering is needed to stabilize the crystalline  $\text{Y}_1\text{Ba}_2\text{Cu}_3\text{O}_x$  phase if postannealing is not used.

## REPORTS ON SOLID STATE RESEARCH

1 May Through 31 July 1989

### PUBLISHED REPORTS

#### Journal Articles

##### JA No.

- |       |   |   |   |
|-------|---|---|---|
| 6059A | Lateral Confinement of Microchemical Surface Reactions: Effects on Mass Diffusion and Kinetics  | H.J. Zeiger<br>D.J. Ehrlich                             | J. Vac. Sci. Technol. B 7, 466 (1989)                         |
| 6082  | Wide-Band Superconductive Chirp Filters   | M.S. DiIorio<br>R.S. Withers<br>A.C. Anderson           | IEEE Trans. Microwave Theory Tech. 37, 706 (1989), AD-A209960 |
| 6112  | Hydrodynamic Dispersion in Rotating-Disk OMVPE Reactors: Numerical Simulation and Experimental Measurements                                   | S. Patnaik*<br>R.A. Brown*<br>C.A. Wang                 | J. Cryst. Growth 96, 153 (1989)                               |
| 6164  | The Extinction Ratio in Optical Two-Guide Coupler $\Delta\beta$ Switches  | J.P. Donnelly<br>L.A. Molter*<br>H.A. Haus*             | IEEE J. Quantum Electron. 25, 924 (1989)                      |
| 6201  | Validation of Model of External-Cavity Semiconductor Laser and Extrapolation from Five-Element to Multielement Fiber-Coupled High-Power Laser | R.H. Rediker<br>C.J. Corcoran<br>L.Y. Pang<br>S.K. Liew | IEEE J. Quantum Electron. 25, 1547 (1989)                     |
| 6202  | Linewidth and Offset Frequency Locking of External Cavity GaAlAs Lasers   | J. Harrison<br>A. Mooradian                             | IEEE J. Quantum Electron. 25, 1152 (1989)                     |
| 6204  | Luminescence of (AlGa)As and GaAs Grown on the Vicinal (511)B-GaAs Surface by Molecular Beam Epitaxy  | E. Towe*<br>H.Q. Le<br>J.V. Hryniewicz<br>C.G. Fonstad* | J. Vac. Sci. Technol. B 7, 395 (1989)                         |

---

\* Author not at Lincoln Laboratory.

**JA No.**

- |      |   |  |  |
|------|---|--|--|
| 6218 | Structural Properties of As-Rich GaAs Grown by MBE at Low Temperature   | M. Kaminska*<br>Z. Liliental-Weber*<br>E.R. Weber*<br>T. George*<br>J.B. Kortright*<br>F.W. Smith<br>B-Y. Tsaur<br>A.R. Calawa | Appl. Phys. Lett. <b>54</b> , 1881 (1989)                              |
| 6232 | A New Approach to Modeling Heteroepitaxy, as Illustrated by GaAs on Si(100)                                     | E. Kaxiras*<br>O.L. Alerhand*<br>J.D. Joannopoulos*<br>G.W. Turner   | Phys. Rev. Lett. <b>62</b> , 2484 (1989)                               |
| 6235 | High-Power, Diffraction-Limited, Narrow-Band, External-Cavity Diode Laser                                       | W.F. Sharfin<br>J. Seppala<br>A. Mooradian<br>B.A. Soltz*<br>R.G. Waters*<br>B.J. Vollmer*<br>K.J. Bystrom*                    | Appl. Phys. Lett. <b>54</b> , 1731 (1989) AD-A208493                   |
| 6249 | Relative Performance of Impedance-Matched Lumped-Element and Traveling-Wave Integrated-Optical Phase Modulators | L.M. Johnson   | IEEE Photon. Technol. Lett. <b>1</b> , 102 (1989)                      |
| 6260 | Lamp Shop Hint  | D.L. Hovey<br>J.N. McMillan  | Fusion, J. Amer. Scientific Glassblowers Society <b>36</b> , 62 (1989) |
| 6269 | Gallium Phosphide Microlenses by Mass Transport   | Z.L. Liao<br>V. Diadiuk<br>J.N. Walpole<br>D.E. Mull   | Appl. Phys. Lett. <b>55</b> , 97 (1989)                                |
| 6273 | Frequency-Modulated Nd:YAG Microchip Lasers   | J.J. Zaynowski<br>A. Mooradian   | Opt. Lett. <b>14</b> , 618 (1989)                                      |

---

\* Author not at Lincoln Laboratory.

# Meeting Speeches

## MS No.

- |      |   |  |   |
|------|---|--|---|
| 8110 | Low-Background Application of Schottky-Barrier IR Sensors   | M.J. Cantella<br>N.C. Davison, III<br>C.H. Gylfphe<br>J.P. Mattia<br>B-Y. Tsaor                      | <i>Optical Sensors and Photography</i> , Proc. SPIE 1071 12 (1989)                            |
| 8170 | Two-Dimensional Surface-Emitting Arrays of GaAs/AlGaAs Diode Lasers                                       | J.P. Donnelly<br>K. Rauschenbach<br>C.A. Wang<br>W.D. Goodhue<br>R.J. Bailey                         | <i>Laser Diode Technology and Applications</i> , L. Figueroa, Ed., Proc. SPIE 1043, 92 (1989) |
| 8253 | Large-Signal Characterization of Millimeter-Wave Transistors Using an Active Load-Pull Measurement System | R. Actis<br>R.A. McMorran<br>R.A. Murphy<br>M.A. Hollis<br>R.W. Chick<br>C.O. Bozler<br>K.B. Nichols | 1989 IEEE MTT-S Intl. Microwave Symposium Digest, 13-15 June 1989, p. 835, AD-A209964         |
| 8260 | Superconducting Stripline Resonators and High- $T_c$ Materials  | D.E. Oates<br>A.C. Anderson<br>B.S. Shih   | 1989 IEEE MTT-S Intl. Microwave Symposium Digest, 13-15 June 1989, p. 627, AD-A209965         |
| 8265 | A Theoretical and Experimental Comparison of Directly and Externally Modulated Fiber-Optic Links          | C.H. Cox, III<br>L.M. Johnson<br>G.E. Betts  | 1989 IEEE MTT-S Intl. Microwave Symposium Digest, 13-15 June 1989, p. 689, AD-A209967         |
| 8305 | High-Performance Wideband Infrared Photomixers  | D.L. Spears  | Proc. Fifth Conference on Coherent Laser Radar, Munich, FRG, 5-9 June 1989, p. 137            |

# UNPUBLISHED REPORTS

## Journal Articles

### JA No.

6222	Possible Observation of a Spin Density Wave in $\text{La}_2\text{CuO}_4$ by Raman Scattering	H.J. Zeiger A.J. Strauss G. Dresselhaus* Y.C. Liu* P.J. Picone* M.S. Dresselhaus*	Accepted by Phys. Rev. B
6223	Zone-Melting Recrystallization with Enhanced Radiative Heating for Preparation of Subboundary-Free Silicon-on-Insulator Thin Films	C.K. Chen J.S. Im	Accepted by Appl. Phys. Lett.
6250	High-Sensitivity Lumped-Element Bandpass Modulators in $\text{LiNbO}_3$	G.E. Betts L.M. Johnson C.H. Cox, III	Accepted by J. Lightwave Technol.
6275	Operation of SOI CMOS Devices at Liquid Nitrogen Temperature	K.K. Young B-Y. Tsaur	Accepted by IEEE Electron Device Lett.
6277	Wavelength-Independent Faraday Isolator	P.A. Schulz	Accepted by Appl. Opt.
6284	New OMVPE Reactor for Large-Area Uniform Deposition of InP and Related Alloys	S.C. Palmateer S.H. Groves J.W. Caunt D.L. Hovey	Accepted by J. Electron. Mater.
6309	Highly Uniform GaAs/AlGaAs GRIN-SCH SQW Diode Lasers Grown by Organometallic Vapor Phase Epitaxy	C.A. Wang H.K. Choi M.K. Connors	Accepted by IEEE Photon. Technol. Lett.
6311	Aluminum Oxides as Imaging Materials for 193-nm Excimer Laser Lithography	S.W. Pang R.R. Kunz M. Rothschild R.B. Goodman M.W. Horn	Accepted by J. Vac. Sci. Technol. B

---

\* Author not at Lincoln Laboratory.

### Meeting Speeches\*

#### MS No.

7553C	Advanced Device Fabrication Using Chlorine Ion-Beam-Assisted Etching	W.D. Goodhue	MIT Electrical Engineering and Computer Science Seminar, Cambridge, Massachusetts, 8 May 1989
7654C	Device Applications of Diamonds	M.W. Geis	Electrochemical Society Meeting, Los Angeles, California, 7 May 1989
7718A	Masked Ion Beam Lithography for the Fabrication of Sub- micrometer Devices	S.W. Pang	1989 Intl. MicroProcess Conference, Kobe, Japan, 2-5 July 1989
7812	CCD Retina and Neural Net Processor	A.M. Chiang	NATO Workshop on Robots and Biological Systems, Ciocco, Italy, 26-30 June 1989
7863B	Laser Microchemical Processing	J.G. Black	25th Annual Symposium of New Mexico Chapter, American Vacuum Society, Albuquerque, New Mexico, 8-11 May 1989
8076A	A New Process for Thinned Back-Illuminated CCD Imager Devices	C.M. Huang B.E. Burke B.B. Kosicki R.W. Mountain P.J. Daniels D.C. Harrison G.A. Lincoln N. Usiak M.A. Kaplan A.R. Forte	1989 Intl. Symposium on VLSI Technical Systems and Applications, Taipei, Taiwan, 17-19 May 1989
8185C	Progress in Diode Pumped Solid State Lasers	T.Y. Fan	Seminar Series on Optics and Quantum Electronics, MIT, Cambridge, Massachusetts, 10 May 1989

---

\* Titles of Meeting Speeches are listed for information only. No copies are available for distribution.

**MS No.**

8208	MNOS/CCD Circuits for Neural Network Implementations	J.P. Sage R.S. Withers K.E. Thompson	1989 IEEE Intl. Symposium on Circuits and Systems, Portland, Oregon, 9-11 May 1989
8252A	High-Speed Resonant Tunneling	E.R. Brown	AT&T Device Seminar, Murray Hill, New Jersey, 2 June 1989
8252B	High-Speed Resonant Tunneling	E.R. Brown	Cornell University Electrical Engineering Symposium, Ithaca, New York, 31 May 1989
8255	Continuously Tunable Single-Frequency Nd:YAG Microchip Lasers	J.J. Zayhowski A. Mooradian	Topical Meeting on Tunable Solid State Lasers, Falmouth, Massachusetts, 1-3 May 1989
8262A	Mode-Locked Ti:Al <sub>2</sub> O <sub>3</sub> Laser with a Nonlinear Coupled External Cavity	J. Goodberlet* J. Wang* J.C. Fujimoto* P.A. Schulz S.R. Henion	
8312	Efficient, High-Average-Power, Liquid-Nitrogen-Cooled Ti:Al <sub>2</sub> O <sub>3</sub> Lasers	S.R. Henion P.A. Schulz	
8314	Spectroscopic and Laser Studies of Nd-Doped Materials for Diode-Pumped Lasers	T.Y. Fan M.R. Kokta* D.S. Knowles* A. Cassanho*	
8317	Excited-State Absorption in Ti:YAlO <sub>3</sub>	K.F. Wall R.L. Aggarwal C.P. Khattak*	
8384	Suppression of Laser Spiking by Intracavity Second-Harmonic Generation	T.H. Jeys	
8394A	Scalable, End-Pumped, Diode Laser Pumped Nd:YAG Laser	T.Y. Fan	

---

\* Author not at Lincoln Laboratory.



**MS No.**

8260A	Superconducting Stripline Resonators and High- $T_c$ Materials	D.E. Oates	Workshop on High Temperature Superconductors, Huntsville, Alabama, 23-25 May 1989
8278	Preparation and Patterning of $YBa_2Cu_3O_x$ Thin Films	M. Bhushan A.J. Strauss	} Intl. Cryogenics Material Conference, Los Angeles, California, 25 July 1989
8514	Preparation of $YBa_2Cu_3O_x$ Thin Films by Multisource Deposition	M. Bhushan	
8292	Aluminum Oxides as Imaging Materials for 193-nm Excimer Laser Lithography	S.W. Pang R.R. Kunz M. Rothschild R.B. Goodman M.W. Horn D.J. Ehrlich	} 33rd Intl. Symposium on Electron, Ion, and Photon Beams, Monterey, California, 30 May — 2 June 1989
8293	Controlled-Ambient Exposure of Polysilane Resists at 193 nm	R.R. Kunz S.P. Sawan* M. Rothschild Y.G. Tsai* D.J. Ehrlich	
8294	45°-Mirror Surface-Emitting Diode Lasers and High-Power Arrays	Z.L. Liao J.N. Walpole J.P. Donnelly K. Rauschenbach V. Diadiuk W.D. Goodhue C.A. Wang R.J. Bailey L.J. Missaggia D.E. Mull	IOOC'89, Kobe, Japan, 18-21 July 1989
8310	Monolithic Two-Dimensional GaAs/AlGaAs Laser Arrays Fabricated by Chlorine Ion-Beam Assisted Micromachining	W.D. Goodhue K. Rauschenbach C.A. Wang J.P. Donnelly G.D. Johnson	31st Electronic Materials Conference, Cambridge, Massachusetts, 21-23 June 1989

\* Author not at Lincoln Laboratory.

**MS No.**

8321	Large-Area Uniform OMVPE Growth for GaAs/AlGaAs Quantum-Well Diode Lasers with Controlled Emission Wavelength	C.A. Wang H.K. Choi M.K. Connors	} 31st Electronic Materials Conference, Cambridge, Massachusetts, 21-23 June 1989
8324	Surface Energy Minimization Process in Etched Compound Semiconductor Structures: Mass Transport Kinetics and Microlens Fabrication	Z.L. Liao H.J. Zeiger V. Diadiuk J.N. Walpole D.E. Mull	
8318	Current Status of III-V Opto-electronic Devices on Si	H.K. Choi C.A. Wang G.W. Turner J.P. Mattia S.J. Eglash B-Y. Tsaur	State-of-the-Art Program on Compound Semiconductors, Los Angeles, California, 7-12 May 1989
8321A	Large-Area Uniform OMVPE Growth for GaAs/AlGaAs Quantum-Well Diode Lasers with Controlled Emission Wavelength	C.A. Wang	Seminar, Kopin Corporation, Taunton, Massachusetts, 27 June 1989
8348	Two-Dimensional Diode Laser Arrays	R.C. Williamson	SDI Technical Achievement Symposium, Washington, DC, 29-30 June 1989
8349	Planarizing SiO <sub>2</sub> and a-C:H Films Prepared by Electron Cyclotron Resonance Plasma Deposition	M.W. Horn S.W. Pang M. Rothschild G.A. Ditrner*	VLSI Multilevel Interconnect Conference, Santa Clara, California, 12-14 June 1989
8360	Plasma Etching and Applications of Multilayer Resists	M.A. Hartney	TEGAL Plasma Technology Seminar, San Francisco, California, 22 May 1989
8361	Optoelectronic Device Integration for Q-Switched Pulse Generation	D.Z. Tsang	IEEE LEOS Seminar Series, Waltham, Massachusetts, 11 May 1989
8394B	Scalable, End-Pumped, Diode Laser Pumped Nd:YAG Laser	T.Y. Fan	Seminar, Candela Laser Corporation, Wayland, Massachusetts, 18 May 1989

---

\* Author not at Lincoln Laboratory.

**MS No.**

8402	Homoepitaxial Diamond Films	M.W. Geis	Diamond Technology Initiative Symposium, Crystal City, Virginia, 11-13 July 1989
8416	Recent Advances in Tunable Solid State Lasers	P.L. Kelley	EOCM Colloquium V and Workshops, Farnborough, United Kingdom, 8 June 1989
8418	Hot Electrons in Resonant-Tunneling Diodes	E.R. Brown	Sixth Intl. Conference, Hot Carriers in Semiconductors, Scottsdale, Arizona, 23-28 July 1989
8498	Gallium Arsenide Heteroepitaxial Growth on Silicon	G.W. Turner	NATO Advanced Study Institute, Boca Raton, Florida, 17-28 July 1989
8506	Sputtering of Y-Ba-Cu-O Thin Films	A.C. Anderson	Gordon Research Conference, Tilton, New Hampshire, 19 July 1989

# ORGANIZATION

## SCLID STATE DIVISION

A.L. McWhorter, *Head*  
I. Melngailis, *Associate Head*  
E. Stern, *Associate Head*  
J.F. Goodwin, *Assistant*

D.J. Ehrlich, *Senior Staff*  
N.L. DeMeo, Jr., *Associate Staff*  
J.W. Caunt, *Assistant Staff*

## SUBMICROMETER TECHNOLOGY

D.C. Shaver, *Leader*  
M. Rothschild, *Assistant Leader*

Astolfi, D.K.  
Black, J.G.  
Dennis, C.L.  
Doran, S.P.  
Efremow, N.N., Jr.  
Forte, A.R.  
Gajar, S.A.\*  
Geis, M.W.  
Goodman, R.B.

Hartney, M.A.  
Horn, M.W.  
Kunz, R.R.  
Lyszcza, T.M.  
Maki, P.A.  
Melngailis, J.<sup>†</sup>  
Pang, S.W.  
Sedlacek, J.H.C.  
Uttaro, R.S.

## QUANTUM ELECTRONICS

A. Mooradian, *Leader*  
P.L. Kelley, *Associate Leader*  
A. Sanchez-Rubio, *Assistant Leader*

Aggarwal, R.L.  
Barch, W.E.  
Belanger, L.J.  
Cook, C.C.  
Daneu, V.  
DeFeo, W.E.  
Fan, T.Y.  
Hancock, R.C.  
Henion, S.R.  
Hotaling, T.C.  
Jeys, T.H.

Korn, J.A.  
Lacovara, P.  
Le, H.Q.  
Menyuk, N.<sup>†</sup>  
Ochoa, J.R.  
Schulz, P.A.  
Seppala, J.P.  
Sharfin, W.F.  
Sullivan, D.J.  
Wall, K.F.  
Zayhowski, J.J.

## ELECTRONIC MATERIALS

A.J. Strauss, *Leader*  
B-Y. Tsaur, *Associate Leader*  
H.J. Zeiger, *Senior Staff*

Anderson, C.H., Jr.  
Button, M.J.  
Chen, C.K.  
Choi, H.K.  
Clark, H.R., Jr.  
Connors, M.K.  
Delaney, E.J.

Eglash, S.J.  
Fahey, R.E.  
Finn, M.C.  
Iseler, G.W.  
Kolesar, D.F.  
Krohn, L., Jr.  
Mastromattei, E.L.  
Mattia, J.P.

McGilvary, W.L.  
Nechay, B.A.  
Nitishin, P.M.  
Pantano, J.V.  
Tracy, D.M.  
Turner, G.W.  
Wang, C.A.

---

\* Research Assistant

† Part Time

## APPLIED PHYSICS

R.C. Williamson, *Leader*  
D.L. Spears, *Assistant Leader*  
R.H. Rediker, *Senior Staff*

Aull, B.F.	Lind, T.A.
Bailey, R.J.	Missaggia, L.J.
Betts, G.E.	Mull, D.E.
Bossi, D.E.*	O'Donnell, F.J.
Corcoran, C.J.*	Palmacci, S.T.
Cox, C.H., III	Palmateer, S.C.
Diadiuk, V.	Rauschenbach, K.
Donnelly, J.P.	Reeder, R.E.
Ferrante, G.A.	Roussell, H.V.
Groves, S.H.	Shiple, S.D.*
Harman, T.C.	Tsang, D.Z.
Hovey, D.L.	Walpole, J.N.
Johnson, L.M.	Woodhouse, J.D.
Lau, K.M.†	Yee, A.C.
Liau, Z.L.	

## ANALOG DEVICE TECHNOLOGY

R.W. Ralston, *Leader*  
R.S. Withers, *Associate Leader*  
R.M. Lerner, *Senior Staff*†

Anderson, A.C.	Lattes, A.L.
Arsenault, D.R.	Lichtenwalner, D.J.*
Bhushan, M.	Lyons, W.G.
Boisvert, R.R.	Macedo, E.M., Jr.
Brogan, W.T.	Munroe, S.C.
Deanen, A.P.	Oates, D.E.
Fitch, G.L.	Sage, J.P.
Green, J.B.	Slattery, R.L.
Hamm, J.M.	Thompson, K.E.
Holtham, J.H.	Yu-Jahnes, L.S.*

## MICROELECTRONICS

R.A. Murphy, *Leader*  
E.D. Savoye, *Associate Leader*  
B.B. Kosicki, *Assistant Leader*  
R.W. Chick, *Senior Staff*

Actis, R.	Donahue, T.Y.	Mathews, R.H.
Bales, J.W.*	Durant, G.L.	McGonagle, W.H.
Bennett, P.C.	Felton, B.J.	McIntosh, K.A.
Bergeron, N.J.	Gladden, D.B.§	Mountain, R.W.
Bozler, C.O.	Goodhue, W.D.	Nichols, K.B.
Brown, E.R.	Gray, R.V.	Parker, C.D.
Burke, B.E.	Gregory, J.A.	Percival, K.A.
Calawa, A.R.	Hollis, M.A.	Pichler, H.H.
Chen, C.L.	Huang, J.C.M.	Rabe, S.
Chiang, A.M.	Hurley, E.T.	Rathman, D.D.
Chuang, M.L.*	Johnson, B.W.	Reich, R.K.
Clifton, B.J.	Johnson, K.F.	Reinold, J.H., Jr.
Cooper, M.J.	LaFranchise, J.R.	Smith, F.W.*
Daniels, P.J.	Lincoln, G.A., Jr.	Sollner, T.C.L.G.
Doherty, C.L., Jr.	Mahoney, L.J.	Vera, A.
Dolat, V.S.	Manfra, M.J.	Wilde, R.E.

---

\* Research Assistant

† Visiting Staff

‡ Part Time

§ Staff Associate

# 1. ELECTROOPTICAL DEVICES

## 1.1 HIGH-PERFORMANCE OPTICAL ANALOG LINK USING EXTERNAL MODULATION

Optical analog links are attractive for many applications ranging from cable TV distribution to radar-signal transmission at microwave frequencies. These systems often require a link with low noise figure, low RF insertion loss, and high dynamic range. This has been difficult to achieve, especially for links using direct laser modulation. We describe here an optical analog link which utilizes a high-sensitivity external modulator and a high-power low-noise CW laser to achieve significantly higher performance than in previously reported links.<sup>1,2</sup>

The optical link, shown in Figure 1-1, consists of a CW laser, an external modulator, an optical fiber, and a PIN detector. Optical transmission loss was negligible in our experimental arrangement because the fiber length was short (several meters). It has been shown<sup>3</sup> that link gain, noise figure, and dynamic range all improve with increasing laser power and that link gain and noise figure improve with increasing modulator response.

High modulator response was obtained by impedance matching a Ti-indiffused lithium niobate waveguide interferometer with 55-mm-long electrodes to the RF input with a loosely coupled double-tuned transformer.<sup>4</sup> The secondary of the transformer resonated with the modulator capacitance in this double-tuned circuit. At the resonant frequency of 50 MHz, this passive circuit gave the modulator about 10 dB higher response than with the usual baseband resistive termination. The peak

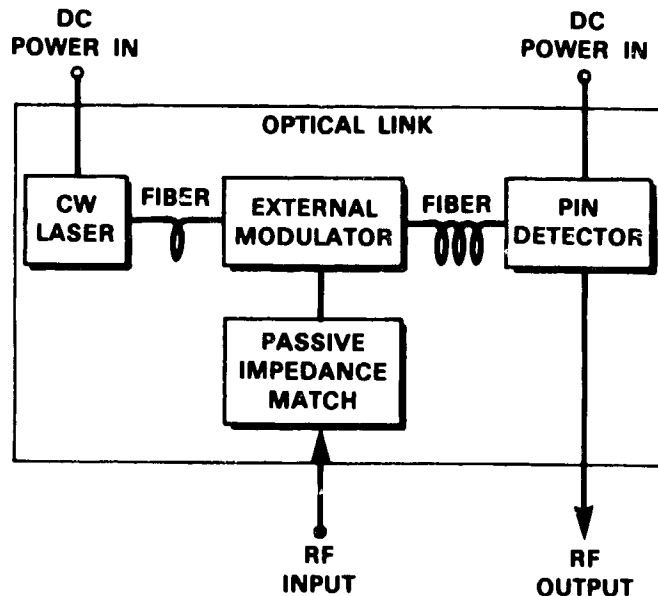


Figure 1-1. Block diagram of the optical analog link.

response was equivalent to a  $\bar{V}_\pi$  of 300 mV at 50  $\Omega$ . This impedance-matched modulator had a bandpass response with a 3-dB bandwidth of 30 MHz. The fiber-device-fiber optical insertion loss was 4.5 dB when the interferometer was biased for maximum transmission. However, in our link experiments the modulator was biased at the half-power point to maximize sensitivity and to eliminate even harmonics and even intermodulation products.

A diode-pumped 1.32- $\mu\text{m}$  Nd:YAG laser was used as the optical source because it offered the important advantages of high output power and low relative intensity noise (RIN). The particular laser used here had a  $\text{RIN} < -165 \text{ dB/Hz}$  near 50 MHz and provided 55 mW of optical power in the input fiber.

The RF output of the link was measured at the output of the reverse-biased InGaAs PIN photodetector. No electronic RF amplification was used in the link. The high laser power and high modulator response resulted in a small-signal RF-to-RF gain of 11 dB at 50 MHz.

Although dynamic range can be defined in many different ways,<sup>5</sup> we used the more stringent intermodulation-free dynamic range, which is the difference between the noise level at a specified bandwidth and the maximum input signal that produces no third-order intermodulation signals above that noise level. The third-order intermodulation signal is the largest spurious signal produced by an interferometric modulator when it is biased at the half-power point.

To measure link intermodulation performance, two signals of equal amplitude but different frequency (51 and 52 MHz) were applied to the RF input, and the amplitudes of the fundamental signals and the intermodulation signals were measured at the RF output.<sup>1,5</sup> The results are shown in Figure 1-2. When third-order terms are the dominant spurious signal, the intermodulation-free

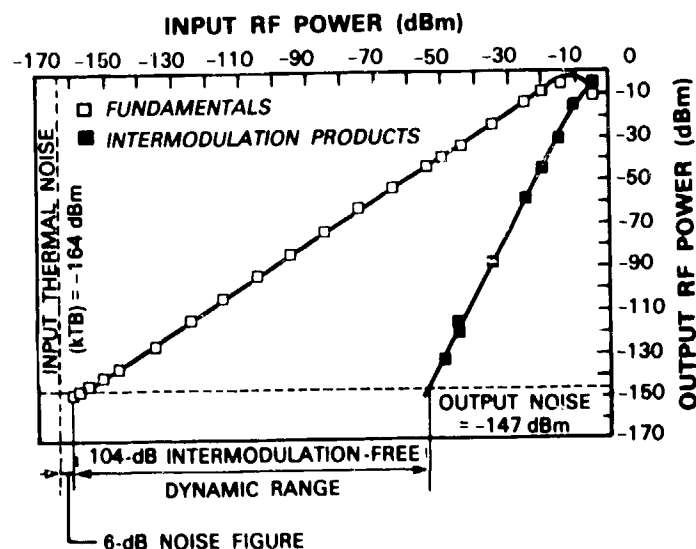


Figure 1-2. Performance of the optical analog link with 55-mW optical power input and 10-Hz noise bandwidth. The uncertainty in the noise level measurement is  $\pm 2 \text{ dB}$ . Solid lines are theoretical predictions based on the nonlinearity of the interferometric modulator.

dynamic range varies inversely as the  $2/3$  power of the noise bandwidth. The measured dynamic range of 104 dB at 10-Hz noise bandwidth corresponds to  $111 \text{ dB-Hz}^{2/3}$ . Another measure of link performance sometimes used is the "maximum signal-to-noise ratio,"<sup>6</sup> which ignores spurious signals. This ratio for our link was 155 dB-Hz. The nonlinearity in the link that produces the third-order intermodulation signal results almost entirely from the nonlinearity of the interferometric modulator. The solid lines in Figure 1-2 are the calculated theoretical performance based upon the measured modulator response, optical power, and detector responsivity, and using the electrical-to-optical transfer function of the interferometric modulator as the only nonlinearity in the link. It can be seen that the measured link performance closely matches this theoretical calculation over the entire 150-dB range of input power used in the experiment.

The measured noise figure of 6 dB ( $\pm 2$  dB) is only 3 dB above the best possible with a passive input impedance match at room temperature. Thermal noise from the resistance of the modulator and/or matching resistors is amplified by the link gain and limits the noise figure to 3 dB at large gains. In this experiment, the noise figure was larger than the 3-dB limit because the modest link gain was not quite sufficient for the amplified thermal noise to dominate shot noise.

No photorefractive problems were detected during the link performance measurements. Photo-voltaic drift was measured more precisely in a separate experiment using the same modulator and applying an optical power of 36 mW (at  $\lambda = 1.32 \mu\text{m}$ ) to the interferometer input. With no dc bias voltage on the electrodes, the drift in the interferometer phase bias point over a measurement time of 47 h was  $< 9^\circ$ , and even this small drift seemed to be caused by effects unrelated to optical power. Optical power limiting caused by stimulated Brillouin scattering in the fibers was also not observed because of the short fiber length.

G.E. Betts	K.G. Ray
L.M. Johnson	R.D. Glenn
C.H. Cox, III	A.C. Yee

## 1.2 1-Gb/s FREE-SPACE OPTICAL INTERCONNECTION BETWEEN DIGITAL CIRCUITS

Optical interconnections are of interest as a high-speed alternative to electrical interconnections between digital circuits.<sup>7,8</sup> A major obstacle to the use of optical interconnections over short distances has been high optoelectronic conversion losses. With high conversion losses, optical interconnections require transmitter circuits in order to drive the optical source and receiver circuits to restore the signal to digital-logic voltage levels. These circuits increase the complexity, cost, power requirement, and area for each of the thousands of interconnections in an advanced computer. We describe here an efficient, simple free-space optical interconnection between two digital circuits which operates at a clock rate of 1 GHz. The interconnection includes a diode laser, two miniature lenses, and a detector. The diode laser is connected directly to the output of one digital circuit, and the detector is connected directly to the input of another digital circuit without external drivers, preamplifiers, or other interface circuits.



Characteristics of the laser, the optics, and the detector are important in the achievement of an efficient optical interconnect that can link digital logic circuits without additional amplification. The diode laser must have a low threshold current ( $<20$  mA) so that it can be driven directly by logic circuits, and a high differential efficiency for efficient electrical-to-optical power conversion. The optics must be antireflection coated and have a large numerical aperture to collect and collimate all diode output radiation. The detector must have high quantum efficiency and be able to handle the large incident power levels ( $>1$  mW).

The experimental high-speed free-space optical interconnection made between two circuit boards is shown schematically in Figure 1-3. A  $1.3\text{-}\mu\text{m}$  GaInAsP laser with a threshold current of 5 mA and a differential quantum efficiency of 35 percent per facet was connected directly to a commercial GaAs code generator with a 1-GHz clock frequency capability. The laser was biased below threshold for a logic "0". An aspheric  $0.55\text{-NA}$ , 5-mm-diam. compact disc lens collected and collimated the laser output, while an identical lens focused the beam onto the detector. The separation between lenses was 24 cm. A  $100\text{-}\mu\text{m}$ -diam. PIN photodiode with  $\sim 70$ -percent quantum efficiency was connected directly to the input of a commercial GaAs D-type flip-flop. The flip-flop contained an internal comparator, as noted in Figure 1-3.

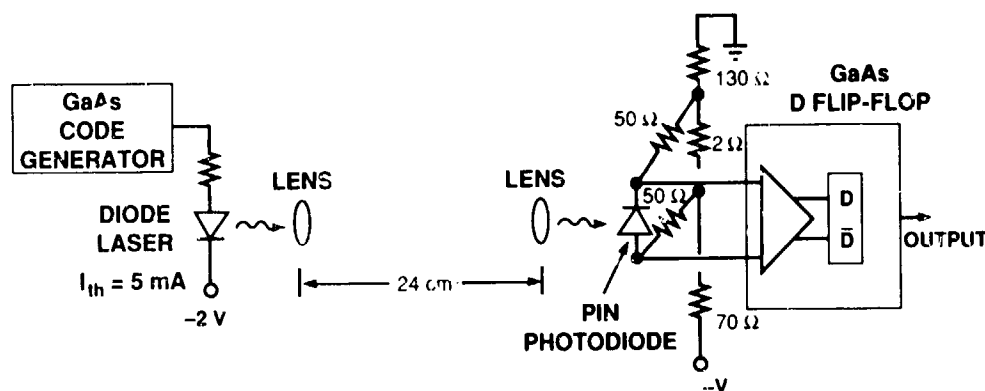


Figure 1-3. Schematic circuit of experimental free-space optical interconnection system. The interconnect consists of a diode laser, two miniature lenses, and a detector.

When the optical components were aligned, the current efficiency (defined as the ratio of the differential current out of the detector to the differential current into the laser) was as high as 12.5 percent and significantly better than the 1 to 3 percent characteristic of many high-speed fiber-optic systems. This link was operated at clock frequencies from 100 MHz to the 1-GHz limit of the code generator, which corresponds to a 1-Gb/s data rate. The recovered signal at the output of the D-type flip-flop is shown in Figure 1-4 along with the laser electrical drive signal for a clock frequency of 1 GHz. These results show that simple high-performance optical interconnections are possible and that considerable reduction in optical interconnection complexity can be achieved with

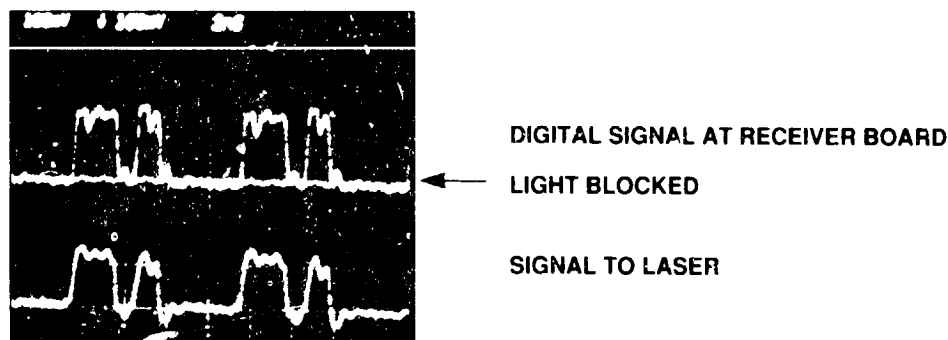


Figure 1-4. Upper trace: output from GaAs digital circuit connected directly to detector. Lower trace: 1-Gb/s electrical drive signal to laser on another circuit board separated from detector by 24 cm. Scale: 1 V/div vertical; 2 ns/div horizontal.

efficient components. Simple optical interconnections of this type could be applied, in either free-space or fiber-optic form, between computer mainframes, modules, and boards.

D.Z. Tsang

### 1.3 MASS-TRANSPORTED BURIED-HETEROSTRUCTURE GaAs LASERS

Successful operation has been achieved of GaAs buried-heterostructure (BH) lasers fabricated for the first time by the mass-transport technique. In these devices, the usual AlGaAs cladding material is replaced by  $\text{Ga}_{0.51}\text{In}_{0.49}\text{P}$  (abbreviated as GaInP). This alloy is lattice matched to GaAs and, as reported recently,<sup>9</sup> maintains the ratio of group III elements during mass transport.

GaInP/GaAs double-heterostructure (DH) lasers, grown by hydride vapor phase epitaxy, were first reported by Nuese *et al.*<sup>10</sup> Recently, quantum-well lasers of these GaInAsP/GaAs materials with state-of-the-art power-conversion efficiencies (66 percent) and threshold current densities ( $<100 \text{ A/cm}^2$ ) have been reported by Alferov and coworkers at the Ioffe Institute.<sup>11,12</sup> These structures were grown using liquid phase epitaxy.

In comparison with AlGaAs/GaAs, GaInP/GaAs requires more demanding crystal growth for several reasons, including lattice-matching constraints. However, special fabrication techniques, which are difficult to use with reactive aluminum compounds, can be fully exploited in the GaInP/GaAs system and should lead to new and improved devices. In our case, the epitaxial growth was done in an organometallic vapor phase epitaxial reactor designed for growth of abrupt interfaces<sup>13</sup> and the mass-transport technique was used for fabrication. That fabrication technique has led to the development of BH lasers and surface-emitting laser arrays for InGaAsP/InP materials.<sup>14</sup>

The heterostructure investigated in our experiments consisted of six layers grown on a GaAs substrate, which was Si doped ( $n \sim 1 \times 10^{18} \text{ cm}^{-3}$ ) and oriented  $2^\circ$  off (100) toward (110). The layers in order of growth were: 0.2- $\mu\text{m}$ -thick n-GaAs buffer layer, 1- $\mu\text{m}$ -thick n-GaInP cladding

layer, 0.1- $\mu\text{m}$ -thick undoped GaAs active layer, 1- $\mu\text{m}$ -thick p-GaInP cladding layer, 0.2- $\mu\text{m}$ -thick p-GaAs contacting layer, and a 0.3- $\mu\text{m}$ -thick p-GaInP cap layer. The GaInP cap layer is needed to facilitate the mass transport as described in Reference 9. Silicon (silane) and Zn (dimethylzinc) were used as dopants at concentrations of  $\sim 1 \times 10^{18} \text{ cm}^{-3}$ .

Broad-area devices were fabricated on a portion of the wafer in which the top GaInP cap layer was removed by chemical etching. On a portion with the top GaInP cap layer, a two-step mass-transport fabrication of buried-stripe devices was undertaken as described in Reference 9. The material was held at  $\sim 750^\circ\text{C}$  for 1 h during each of the mass-transport steps.

Figure 1-5 shows light output vs the diode forward current in pulsed operation for a device with a buried-active-layer width of  $\sim 1 \mu\text{m}$  and a cleaved-cavity length of  $\sim 400 \mu\text{m}$ . Lasing occurred at a threshold current of  $\sim 33 \text{ mA}$ . The differential quantum efficiency was about 15 percent per facet. The threshold current density for broad-area devices was  $\sim 1300 \text{ A/cm}^2$ . This is about  $6\times$  lower than that for the BH stripe devices. When heat sunk, the stripe devices operated continuously at room temperature with threshold currents about the same as the pulsed threshold currents. Both broad-area and stripe devices emit at  $\sim 0.89\text{-}\mu\text{m}$  wavelength at room temperature. This is somewhat longer than the wavelength corresponding to the room-temperature energy gap of undoped GaAs, and is probably indicative of band tails caused by inadvertent impurity doping in the active region.

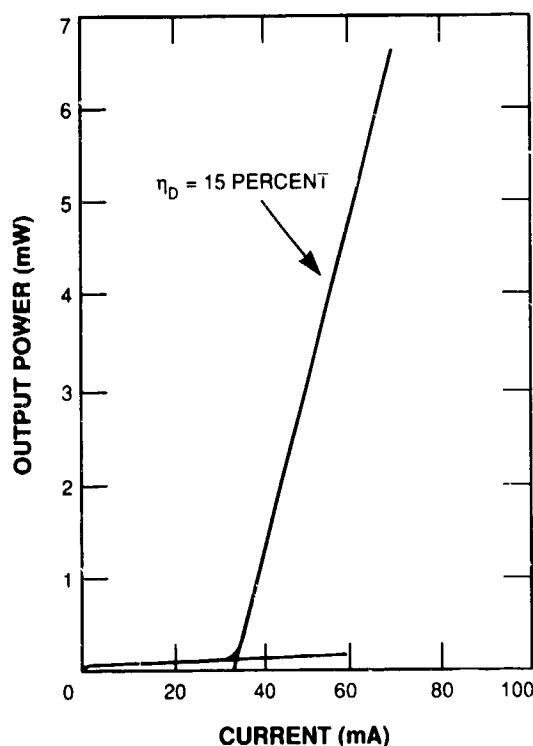


Figure 1-5. Relative light output vs forward current for mass-transported BH GaInP/GaAs/GaInP laser with  $\sim 1\text{-}\mu\text{m}$  active-layer width and  $\sim 400\text{-}\mu\text{m}$  length.

These initial results on the first mass-transported GaAs BH lasers are extremely encouraging. Future refinements in both crystal growth and fabrication techniques are expected to yield major improvements in device performance.

S.H. Groves	S.C. Palmateer
Z.L. Liao	J.N. Walpole
L.J. Missaggia	

## REFERENCES

1. W.E. Stephens and T.R. Joseph, *J. Lightwave Technol.* **LT-5**, 380 (1987).
2. C.H. Bulmer, *Appl. Phys. Lett.* **53**, 2368 (1988).
3. C.H. Cox, III, L.M. Johnson, and G.E. Betts, in *1989 IEEE MTT-S International Microwave Symposium Digest* (IEEE, New York, 1989), pp. 689-692.
4. G.E. Betts, L.M. Johnson, and C.H. Cox, III, to be published in *J. Lightwave Technol.* (December 1989).
5. B.H. Kolner and D.W. Dolfi, *Appl. Opt.* **26**, 3676 (1987).
6. H. Blauvelt and K. Lau, *Proc. SPIE* **995**, 106 (1988).
7. J.W. Goodman, F.J. Leonberger, S.-Y. Kung, and R.A. Athale, *Proc. IEEE* **72**, 850 (1984).
8. See, for example, *Opt. Eng.* **25**, 1075 (1986).
9. Solid State Research Report, Lincoln Laboratory, MIT (1989:2), pp. 11-13.
10. C.J. Nuese, G.H. Olsen, and M. Ettenberg, *Appl. Phys. Lett.* **29**, 54 (1976).
11. Zh.I. Alferov, N.Yu. Antonishkis, I.N. Arsent'ev, D.Z. Garbuzov, V.I. Kolyshkin, T.A. Nalet, N.A. Strugov, and A.V. Tikunov, *Fiz. Tekh. Poluprovodn.* **22**, 1031 (1988) [*Sov. Phys. Semicond.* **22**, 650 (1988)].
12. N.Yu. Antonishkis, I.N. Arsent'ev, D.Z. Garbuzov, V.I. Kolyshkin, A.B. Komissarov, A.V. Kochergin, T.A. Nalet, and N.A. Strugov, *Pis'ma Zh. Tekh. Fiz.* **14**, 699 (1988) [*Sov. Tech. Phys. Lett.* **14**, 310 (1988)].
13. S.C. Palmateer, S.H. Groves, J.W. Caunt, and D.L. Hovey, *J. Electron. Mater.* **18**, 645 (1989).
14. Z.L. Liao and J.N. Walpole, *Appl. Phys. Lett.* **50**, 528 (1987), DTIC AD-A180887.

## 2. QUANTUM ELECTRONICS

### 2.1 SINGLE-FREQUENCY Nd:YAG LASER

A standing-wave Nd:YAG laser has been demonstrated to operate at a single frequency up to 1.4 times threshold with no frequency-selecting devices. This laser contains only two optical elements: a Nd:YAG crystal with one end coated for high reflectivity, and a mirror which serves as the output coupler. The total cavity length was 8.5 cm, more than 100 times the length of the single-frequency microchip laser.<sup>1</sup> The long cavity allows the insertion of intracavity devices.

Several techniques exist for obtaining single-frequency operation of a Nd:YAG laser with no intracavity elements. In a unidirectional ring cavity, spatial hole burning does not exist because of the traveling-wave nature of the field distribution. The ring cavity requires a unidirectional device to force stable unidirectional operation. Such lasers are more complicated (and more expensive) than a standing-wave Nd:YAG laser.

Another single-frequency Nd:YAG laser, the microchip laser,<sup>1</sup> relies on short cavity length to force single-frequency operation. With a 0.73-mm-long cavity, the next longitudinal mode lies 113 GHz away ( $c/2L$ ). The gain profile of Nd:YAG has a half-width at half-maximum of 75 GHz. The next longitudinal mode therefore sees less than half of the peak gain and is strongly suppressed at pump powers up to 40 times threshold.

The Nd:YAG laser used in this experiment (shown in Figure 2-1) was optically pumped by a  $\text{Ti:Al}_2\text{O}_3$  laser which was tuned with a birefringent tuner to 808 nm. The 1-cm-long Nd:YAG rod was doped with 1-percent  $\text{Nd}^{3+}$ . One end of the crystal was flat and antireflection coated for 1.064  $\mu\text{m}$ . The other end was polished to have a 1-cm radius and coated to be a high reflector at 1.064  $\mu\text{m}$  and antireflection coated for 808 nm. The radius of curvature of the output coupler was 7.5 cm with 10-percent transmission. The Nd:YAG laser threshold was 46 mW. With 54 mW of pump light, the laser operated at a single frequency with an output power of 1.2 mW.

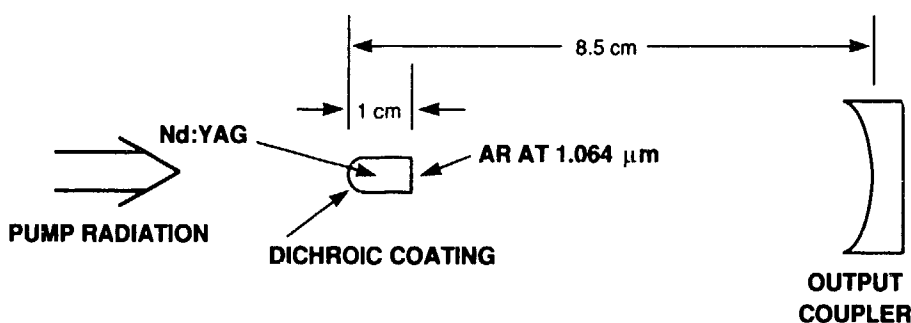


Figure 2-1. Sketch of the single-frequency Nd:YAG laser. The Nd:YAG crystal has a curved end ( $R = 1$  cm) with a dichroic coating that is a high reflector at 1.06  $\mu\text{m}$  and transmits the pump radiation at 808 nm. The other end of the crystal is antireflection (AR) coated at 1.06  $\mu\text{m}$ . The output coupler has a radius of curvature of 7.5 cm and a 90-percent reflectivity at 1.06  $\mu\text{m}$ .

The surprising result is that this relatively long cavity will run at a single frequency at 1.4 times threshold. There appear to be three properties of the Nd:YAG laser that help to overcome spatial hole burning so that the laser operates at a single frequency: (1) diffusion of the population inversion, (2) a large output coupling, and (3) a short gain region abutting the high reflector at one end of the cavity.

That the diffusion of the population inversion helps can be deduced from the fact that the excitation of a  $\text{Nd}^{3+}$  ion in 1-percent-doped Nd:YAG migrates to a nearest neighbor with a transfer time of  $3 \times 10^{-7}$  s (Reference 2). The corresponding diffusion distance is 50 nm in one radiative lifetime. This distance is less than, but comparable to, the 146-nm ( $=\lambda/4n$ ) distance from minimum to maximum intensity for a standing wave in the Nd:YAG crystal; therefore, spatial hole burning is reduced but not eliminated.

The large output coupling contributes because the more the ratio of intensities of the two counterpropagating waves deviates from unity, the smaller is the contrast between maximum and minimum axial intensity and the smaller the spatial hole-burning effect. When a 5-percent output coupler was substituted for the 10-percent output coupler, the laser operated in several longitudinal modes, even near threshold. The laser ran at a single frequency in this case only by including an etalon in the cavity.

The third aspect of this laser that helps single-frequency operation is the short gain region abutting the high reflector through which the crystal is pumped. The gain region is short because the high doping causes most of the pump radiation to be absorbed near the end of the crystal. Since all standing-wave modes have a node at the high reflector, all modes within the narrow gain bandwidth remain in spatial phase through the gain region and, hence, must compete for the same population inversion. In contrast, for a gain medium in the center of the cavity, two modes access different population inversion when the nodes of one mode overlap the antinodes of the second mode, and vice versa. The theory<sup>3</sup> of this effect has been worked out and experimentally<sup>4</sup> realized.

S.R. Henion

P.A. Schulz

## **2.2 LASER PUMPING OF SOLID-STATE AMPLIFIERS USING RANDOM BINARY-PHASE PLATES**

Laser pumping of solid-state amplifiers requires good spatial overlap between the pump and signal beams. This can be difficult to achieve with a nonuniform pump intensity profile. The presence of large spatial variations (hot spots) in the intensity of the pump beam can result in even larger spatial variations in the amplified intensity of the signal beam, because small-signal gain is an exponential function of the pump intensity. These large spatial variations in the output signal intensity will lead to increased beam divergence and possible damage to optical components. Damage to the amplifier medium may also result from hot spots in the pump beams.

We have used transmissive random binary-phase plates<sup>5</sup> (RBPP) to smooth out hot spots in frequency-doubled Nd:YAG laser radiation used to pump  $\text{Ti:Al}_2\text{O}_3$  amplifiers. Random phase plates have been used in laser fusion experiments to obtain uniform illumination of fusion targets.

A transmissive RBPP consists of a two-dimensional array of transmissive elements, each of which introduces a phase shift randomly chosen to be either  $\theta_0$  or  $\theta_0 + 180^\circ$ , where  $\theta_0$  is an arbitrary constant. For ease of fabrication, we have chosen the elements of the array to be squares having sides of length  $a$ . The phase shift is achieved by etching elements of depth  $t$  on a transparent substrate, where  $t$  is given by

$$t = \frac{\lambda}{2(n-1)}, \quad (2-1)$$

in which  $\lambda$  is the wavelength of the laser, and  $n$  is the index of refraction of the substrate. The approximate size of the elements is chosen so that they are small compared with the scale of spatial intensity variations in the laser beam. In the far-field, the RBPP removes hot spots at the expense of introducing speckle. A lens following the RBPP is used to produce the far-field intensity distribution of the pump beam in the amplifier, as shown schematically in Figure 2-2. For an array consisting of

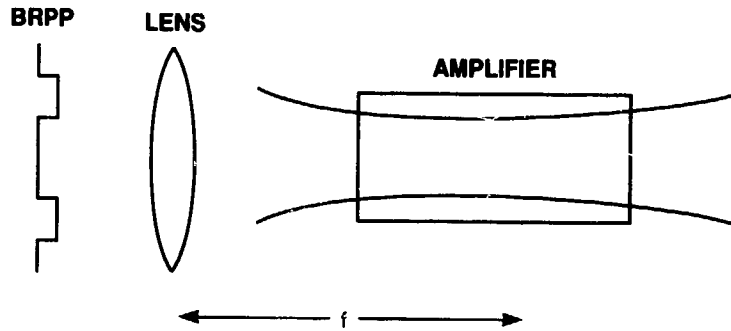


Figure 2-2. Geometry used for pumping amplifiers using transmissive random binary-phase plates. A lens of focal length  $f$  is used to produce the far-field intensity distribution within the crystal.

square elements, the envelope of the far-field intensity distribution is that of a single square aperture. Figure 2-3 is a contour plot of the central peak of the far-field intensity distribution for diffraction from a square aperture. At the  $1/e^2$  intensity points, the contour can be approximated by a circle of diameter  $D$  which is given by

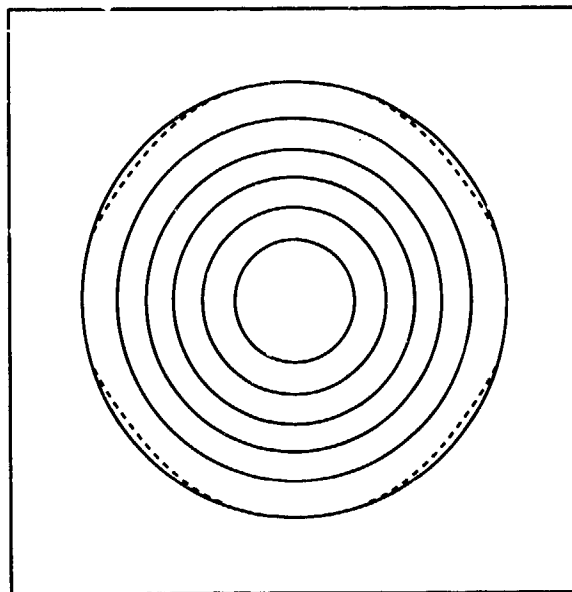
$$D = 1.4 \frac{f\lambda}{a}, \quad (2-2)$$

where  $f$  is the focal length of the lens. The diameter  $d$  of the speckle is approximately

$$d \approx 2 \frac{f\lambda}{A}, \quad (2-3)$$

where  $A$  is the characteristic diameter of the beam. The longitudinal length  $L$  of a speckle has the value

$$L = 4\lambda \left( \frac{f}{A} \right)^2. \quad (2-4)$$



131808-6

*Figure 2-3. Contour plot of the central peak of the far-field intensity distribution for diffraction from a square aperture. At the  $1/e^2$  intensity points, the contour can be approximated by a circle of diameter  $D$  shown by the dashed line.*

The plates used in this work were prepared from fused silica flats by processing techniques common to the semiconductor industry. The flats were cleaned and degreased, coated with a  $0.5\text{-}\mu\text{m}$  layer of photoresist, and prebaked at  $90^\circ\text{C}$  for 30 min. A mask with the desired pattern was prepared using a random-number generation program to assign the binary phase-shift values to each square. The photoresist was exposed to the mask pattern and developed. Finally, the plates were ion-etched in a carbon tetrafluoride plasma for about 20 min. Using this process, we obtained random phase plates with a tolerance in the etched depth of  $\pm 5$  percent.

Figure 2-4 illustrates smoothing of a 532-nm pump beam using a RBPP with  $100\text{-}\mu\text{m}$  square elements. The upper portion of Figure 2-4(a) is a density plot of the intensity profile, where the highest intensity corresponds to the darkest region. In addition to a localized hot spot 2 to 3 times the average intensity, diffraction rings are also apparent. The intensity of the hot spot relative to the rest of the profile is apparent in the lower, three-dimensional plot. Figure 2-4(b) shows the same beam after passage through a RBPP and a lens of 20-cm focal length. The large-scale spatial variations in the pump beam shown in Figure 2-4(a) are clearly removed by the RBPP at the expense of speckle. However, appropriate choice of pump- and signal-beam geometry allows the speckle in the amplified signal beam to be averaged out.



WITHOUT PHASE PLATE

WITH PHASE PLATE

→ 1.5 mm ←

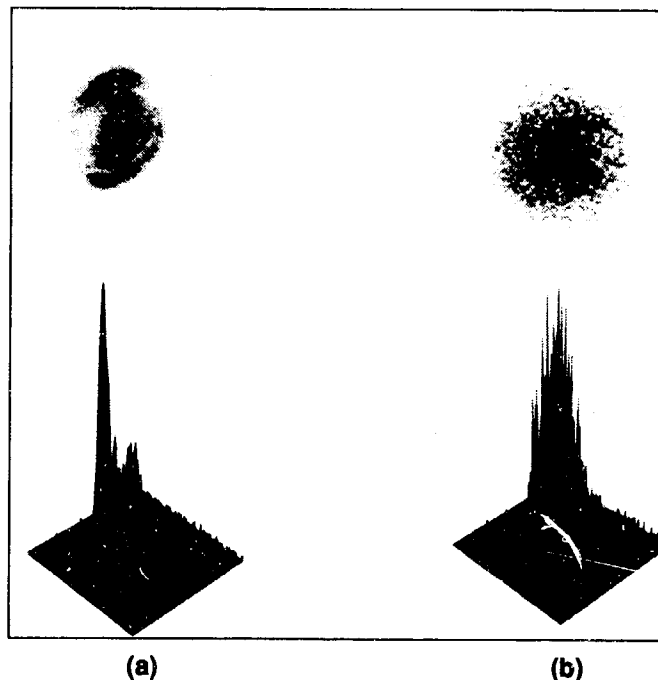


Figure 2-4. Beam smoothing using a random binary-phase plate with 100- $\mu\text{m}$  square elements. The intensity profile of an unsmoothed beam is shown in (a), and of a smoothed beam is shown in (b). The upper figures are density plots where the highest intensity is shown by the darkest regions; the lower figures are 3-dimensional plots of the same profiles. The large spatial variation shown in (a) is replaced by speckle as shown in (b).

One disadvantage of using RBPPs in the present configuration is that only  $\sim 80$  percent of the incident energy is present in the central peak of the far-field pattern as a result of the step profile of the elements. This percentage may be increased by using properly shaped profiles. Also, the intensity in a given speckle can be several times larger than the average intensity at the location of the speckle, leading to pump-induced damage.

P. Lacovara	M. Geiss
K.F. Wall	K. Krohn
R.L. Aggarwal	B.J. Felton

### 2.3 PASSIVELY MODE-LOCKED $\text{Ti}:\text{Al}_2\text{O}_3$ LASER USING A NONLINEAR COUPLED CAVITY

Short-pulse generation in a passive  $\text{Ti}:\text{Al}_2\text{O}_3$  laser has been demonstrated.<sup>6</sup> The laser consisted of a cavity containing the gain medium and frequency-selective optics coupled to a second cavity of equal length containing an optical fiber. The interferometric pulse-combining effect of the two

cavities plus the self-phase modulation in the optical fiber gave stable, short-pulsed operation and no other modulation was required.

Coupled-cavity lasers compare favorably with other lasers<sup>7</sup> for subpicosecond pulse generation, including colliding-pulse mode-locked lasers, hybrid mode-locked lasers, synchronously pumped lasers, and compression of picosecond pulsed-laser output using self-phase modulation followed by a dispersive delay. The colliding-pulse laser operates at only one wavelength. The hybrid and synchronously pumped lasers are used exclusively with dye lasers. Pulse compression works well with solid-state lasers, but results in a complicated short-pulse generation scheme.

The coupled-cavity laser was predicted<sup>8</sup> to shorten the pulses of a mode-locked laser, and several groups have confirmed this prediction.<sup>9</sup> This technique of additive-pulse mode locking<sup>9</sup> using the coupled cavity is a generalization of the soliton laser.<sup>10</sup> In principle, the technique is relatively simple because a nonlinear optical element can be placed in a second cavity that is coupled to the main laser cavity, allowing optimization of the main laser cavity independent of the second cavity. Previous work with coupled-cavity lasers had required auxiliary<sup>8-10</sup> modulation (i.e., synchronous pumping or active mode locking), which decreased stability and increased complexity. In the present case, short pulses are generated spontaneously without external modulation.

The coupled-cavity  $\text{Ti:Al}_2\text{O}_3$  laser is shown schematically in Figure 2-5. The laser without the second cavity typically runs with a 15-percent output coupler and had an output power of 1 W, with 8 W of argon-ion laser pump radiation. In order to obtain the short pulses, the length difference

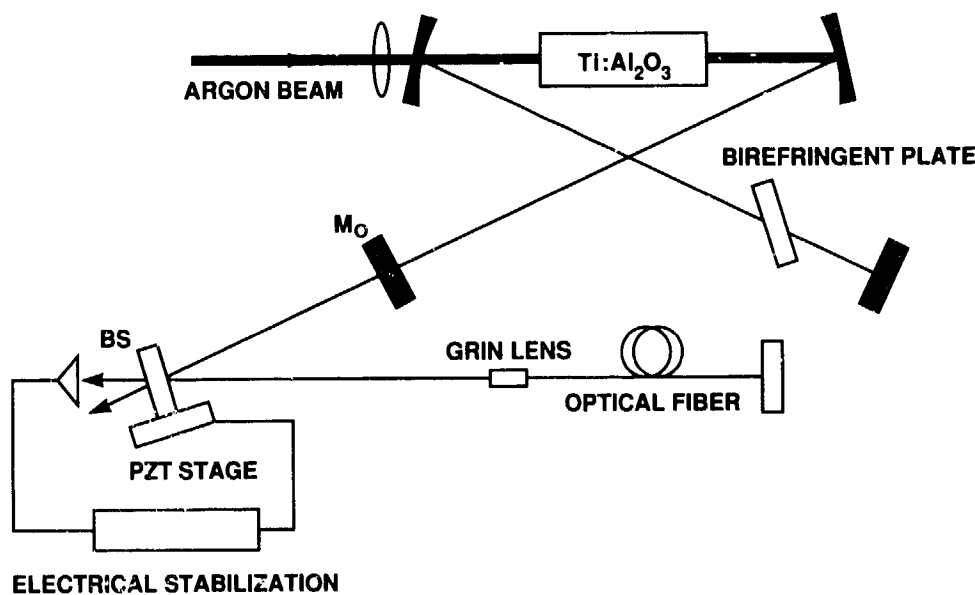


Figure 2-5. Schematic of the passively mode-locked  $\text{Ti:Al}_2\text{O}_3$  laser system. The four mirrors around the  $\text{Ti:Al}_2\text{O}_3$  crystal constitute the main laser cavity. The mirror  $M_o$  is a 15-percent transmitting mirror. The second cavity consists of the mirror  $M_o$ , a beam splitter (BS) that acts as the output coupler, a GRIN lens to focus light into the optical fiber, and a butt-coupled mirror.

between the two cavities must be maintained within one-quarter of a wavelength. The length difference was stabilized by adjusting a piezoelectric transducer to maintain a constant power in the second cavity.

The laser generated an 80-MHz pulse train of 1.5-ps pulses with an average power of 0.25 W. The spectrum of the pulses was significantly broader than inferred from the Fourier transform of the pulse duration. Therefore, a grating pair was used as a dispersive delay line to shorten the pulses down to 220 fs, which gave a pulse-bandwidth product within 20 percent of the value for a transform-limited Gaussian pulse. The laser was tuned from 740 to 800 nm, a range restricted by the output coupler. In principle, the laser should be tunable over the entire lasing range, from 660 nm to 1.1  $\mu\text{m}$ . The laser was very stable, with its stability limited by intensity noise on the argon-ion laser and the feedback circuit.

A novel aspect of this work is the self-starting behavior of the mode locking. Self-starting implies that intensity spikes occur which produce sufficient self-phase modulation in the optical fiber to allow the laser to access the region of short-pulse operation. The likely cause of the intensity spike is either longitudinal mode beating or the spontaneous generation of intensity spikes in the coupled cavities,<sup>11</sup> or both.

J. Goodberlet*	S.R. Henion
J. Wan *	P.A. Schulz
J.G. Fujimoto*	

## 2.4 PICOSECOND NONDEGENERATE FOUR-WAVE MIXING IN SEMICONDUCTOR WAVEGUIDES

Optical nonlinearities in GaAs-based heterostructures are being considered for applications in integrated optoelectronics and all-optical information-processing devices. In general, these applications involve the propagation of one or several beams through the device, often in waveguide configuration whose geometry can affect the phenomena significantly.<sup>12</sup> This work is an experimental investigation of the effects of nonlinear optical processes on the propagation of radiation in GaAs/AlGaAs waveguides, utilizing picosecond laser pulses with peak intensity up to  $10^8 \text{ W/cm}^2$ .

Two ultrafast  $\chi^{(3)}$  optical nonlinear phenomena are observed in this study which involves the propagation of two picosecond light pulses with frequencies  $\omega_1$  and  $\omega_2$ , both below the absorption edge, in an AlGaAs single-mode waveguide [Figure 2-6(a)]. The most prominent nonlinear effects are the generation of four-wave-mixing signals at  $2\omega_1 - \omega_2$  (and  $2\omega_2 - \omega_1$ ). The other nonlinearity is the phenomenon of optically induced loss of optical throughput. The four-wave-mixing process can be hypothesized as arising from either one of two mechanisms [Figure 2-6(b,c)]: a nonresonant coherent anti-Stokes Raman scattering (CARS), or virtual two-photon absorption with difference-frequency generation.<sup>13,14</sup> The conversion efficiency of the four-wave-mixing process is as large as 0.5 percent. Time-resolved spectra, shown in Figure 2-7(a), indicate a truly ultrafast process with zero background and complete recovery. When the four-wave-mixing amplitude is plotted vs the detuning

---

\* MIT Department of Electrical Engineering and Computer Science and Research Laboratory of Electronics.

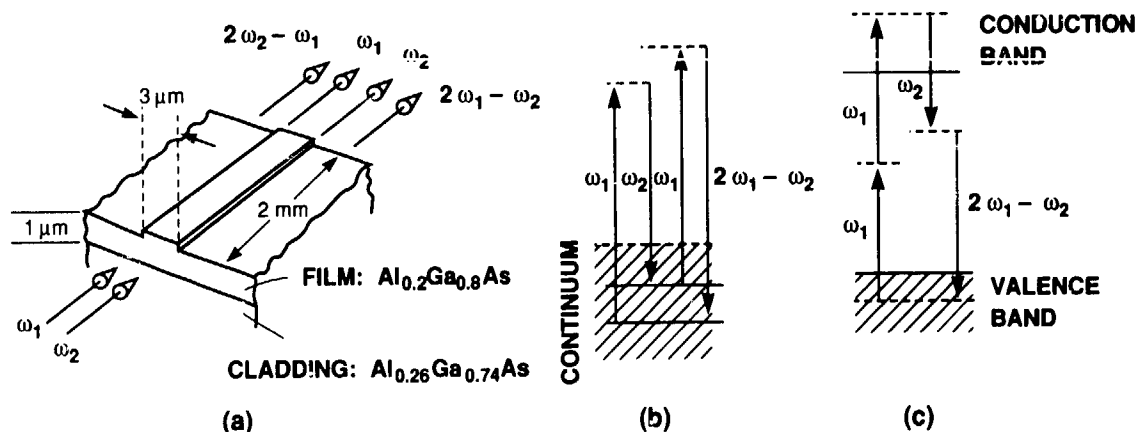


Figure 2-6. (a) Experimental configuration, (b) a CARS process in which the material is excited at  $\omega_1 - \omega_2$ , and (c) a two-photon process in which the material is excited at  $2\omega_1$ .

energy  $\hbar(\omega_1 - \omega_2)$  for the case where all waves are in TM modes [Figure 2-7(b), curve TM], there are no prominent resonance features, and the curve appears to be determined by the phase-matching term  $\Delta kL = (2n_1\omega_1 - n_2\omega_2 - n_3\omega_3)L/c$ , where  $n_i$  is the waveguide effective index at frequency  $\omega_i$ ,  $\omega_3 = 2\omega_1 - \omega_2$ , and  $L$  is the length of the waveguide. The peak at  $\omega_1 - \omega_2 \approx 0$  corresponds to  $\Delta k \approx 0$ , and the dip indicated by the arrow marks the first Maker fringe when  $\Delta kL \approx 2\pi$ . In contrast to the bulk, for a single-mode waveguide there is no angle tuning available to achieve phase matching. However, these waveguides are birefringent due to their geometry and this effect can result in phase matching for nonvanishing  $\omega_1 - \omega_2$ . This is shown in Figure 2-7(b), curve TE, where  $\omega_2$  and  $\omega_3$  are in TM modes, but  $\omega_1$  is changed to a TE mode. The new phase-matching term is given by  $\Delta k'L = (2\nu_1\omega_1/c + \Delta k)L$ , where  $\nu_1$  is the index difference between TE and TM modes. As a result,  $\Delta k'$  vanishes for nonvanishing  $\omega_1 - \omega_2$ , in this case when  $\hbar(\omega_1 - \omega_2) = 29.4\ \text{meV}$ . Calculation using  $\nu_1 = 7.7 \times 10^{-4}$  and  $n(\omega) = n(\omega_1) + a\hbar(\omega - \omega_1)$ , where  $a = 1.3 \times 10^{-3}\ \text{meV}^{-1}$  yields a good fit to the results.

By monitoring the throughput power and polarization of the probe beam  $\omega_2$ , pump-beam-induced absorption and birefringence were also observed in this study. Two-photon absorption was cited as the dominant mechanism in a recent observation of ultrafast optically induced change of refractive index.<sup>15</sup> In the present case, the optically induced loss of throughput causes probe-beam amplitude modulation up to 8 percent and is shown vs probe photon energy in Figure 2-8. The effect is predominantly ultrafast, with zero thermal background, but it also has a weak long-lived tail as shown in the inset of Figure 2-8, probably as a result of optically induced free-carrier absorption.

The strength, speed, and complete absence of any long-lived tail in the observed frequency-mixing processes are sufficient to make an ultrafast optical AND gate. Although the signal output is low in absolute power, the signal-to-noise ratio is excellent. On the other hand, if semiconductor

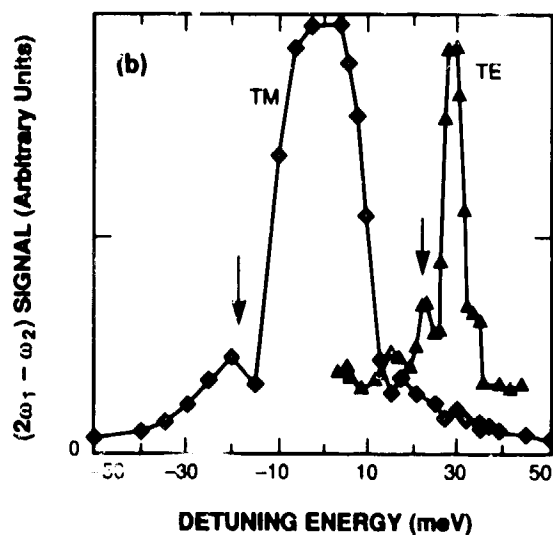
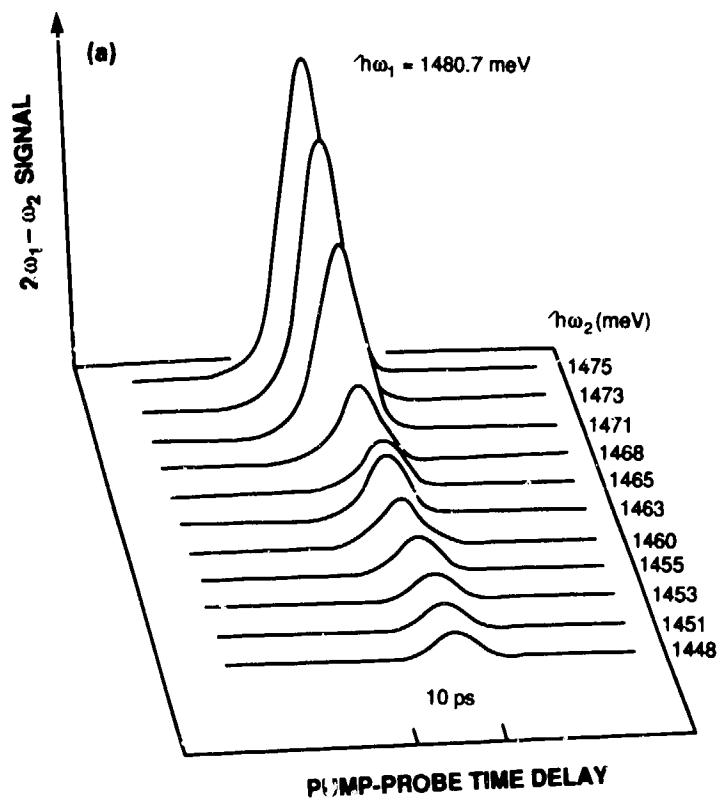


Figure 2-7. (a)  $2\omega_1 - \omega_2$  signal as a function of the time delay between  $\omega_1$  and  $\omega_2$  pulses.  $\hbar\omega_1$  is kept fixed at 1480.7 meV, and  $\omega_2$  is varied. (b) Time-integrated  $2\omega_1 - \omega_2$  signal vs detuning energy  $\hbar(\omega_1 - \omega_2)$ . Curve TM: all waves are in TM modes; curve TE: pump beam  $\omega_1$  is in TE mode,  $\omega_2$  and  $2\omega_1 - \omega_2$  are in TM. The arrows mark the most visible Maker fringes.

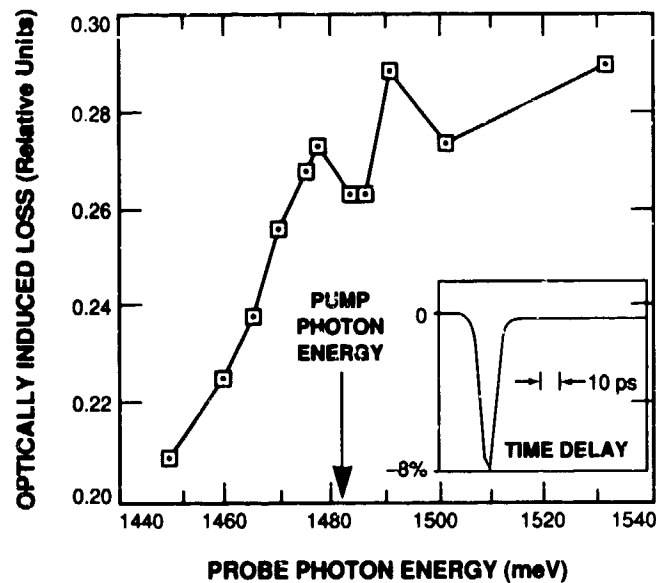


Figure 2-8. Optically induced change in the absorption of probe beam as a function of probe photon energy. The pump frequency is kept fixed as indicated by the arrow. Inset shows the percent change in throughput power of the probe beam as a function of pump-probe time delay.

waveguides are to be used for intrachip multifrequency interconnects, four-wave mixing and optically induced loss must be considered as potential noise sources. These optical nonlinearities must also be considered in designing high-power diode lasers. Device geometries more complex than single-mode waveguide are presently being studied for their influence on nonlinear optical processes.

H.Q. Le	K.B. Nichols
D.E. Bossi	W.D. Goodhue

## REFERENCES

1. J.J. Zayhowski and A. Mooradian, *Opt. Lett.* **14**, 24 (1989).
2. H.G. Danielmeyer, in *Lasers*, Vol. 4, A.K. Levine and A.J. DeMaria, Eds. (Marcel Dekker, New York, 1976), pp. 22-23.
3. J.J. Zayhowski, submitted to *Opt. Lett.*
4. G. Kintz and T. Baer, submitted to *Opt. Lett.*
5. Y. Kato, M. Mima, N. Miyanaga, S. Arinaga, Y. Kitagawa, M. Nakatsuka, and C. Yamanaka, *Phys. Rev. Lett.* **53**, 1057 (1984).
6. J. Goodberlet, J. Wang, J.G. Fujimoto, and P.A. Schulz, submitted to *Opt. Lett.*
7. J.D. Kafka, A.J. Alfrey, and T. Baer, in *Ultrafast Phenomena VI*, T. Yajima, K. Yoshihara, C.B. Harris, and S. Shionoya, Eds. (Springer-Verlag, Berlin, 1988), p. 64.
8. K.J. Blow and D. Wood, *J. Opt. Soc. Am. B* **5**, 629 (1988).
9. K.J. Blow and B.P. Nelson, *Opt. Lett.* **13**, 1026 (1988); P.N. Kean, X. Zhu, D.W. Crust, R.S. Grant, N. Langford, and W. Sibbett, *Opt. Lett.* **14**, 39 (1989); J. Mark, L.Y. Liu, K.L. Hall, H.A. Haus, and E.P. Ippen, *Opt. Lett.* **14**, 48 (1989); C.P. Yakymyshyn, J.F. Pinto, and C.R. Pollock, *Opt. Lett.* **14**, 621 (1989); P.M.W. French, J.A.R. Williams, and R. Taylor, *Opt. Lett.* **14**, 686 (1989).
10. L.F. Mollenauer and R.H. Stolen, *Opt. Lett.* **9**, 13 (1984); F.M. Mitschke and L.F. Mollenauer, *IEEE J. Quantum Elec.* **QE-22**, 2242 (1986).
11. S.M.J. Kelly, *Opt. Commun.* **70**, 495 (1989).
12. G.I. Stegeman, J.J. Burke, and C.T. Seaton, in *Integrated Optical Circuits and Components*, L.D. Hutcheson, Ed. (Marcel Dekker, New York, 1987), pp. 317-396.
13. D.C. Hanna, M.A. Yuratich, and D. Cotter, in *Nonlinear Optics of Free Atoms and Molecules* (Springer-Verlag, Berlin, 1979), Chapter 5.
14. Y.R. Shen, in *The Principles of Nonlinear Optics* (Wiley, New York, 1984), Chapters 14 and 15.
15. K.K. Anderson, M.J. Lagasse, H.A. Haus, and J. Fujimoto, *Appl. Phys. Lett.* (to be published).

### 3. MATERIALS RESEARCH

#### 3.1 TOTAL-DOSE RADIATION EFFECTS ON PtSi SCHOTTKY-BARRIER INFRARED DETECTORS AND FOCAL PLANE ARRAYS

Focal plane arrays consisting of monolithically integrated PtSi Schottky-barrier detectors and CCD readout circuitry are attracting increasing interest for thermal imaging in the 3- to 5- $\mu\text{m}$  spectral band. Although many potential applications would require operation in a radiation-threatened environment, the survivability of such arrays has not been investigated in any detail. In this report we describe a study of total-dose radiation effects on the characteristics of PtSi Schottky-barrier detectors and  $160 \times 244$ -element focal plane arrays operated at 80 K. The excellent total-dose hardness expected for these detectors has been confirmed, and operation of the imager arrays after exposure to total-dose radiation of 0.8 Mrad(Si) has been demonstrated.

The array design is a slightly modified version of one originally developed at David Sarnoff Research Center, which uses a buried-channel CCD structure.<sup>1</sup> Charges generated in each detector by infrared radiation are shifted via a transfer gate to the channel of a parallel CCD shift register and then read out through a serial CCD register. The buried-channel structure reduces the effects of interface-state trapping at the Si/gate-insulator interface because carrier transfer occurs close to the metallurgical junction of the buried channel and substrate, far from the interface. To further reduce radiation effects, the  $\text{SiO}_2$  gate insulator of the MOS devices used in the CCD circuitry has been replaced by a three-layer stack consisting of  $\text{SiO}_2$ ,  $\text{Si}_3\text{N}_4$ , and  $\text{SiO}_2$  layers with thicknesses of about 15, 60, and 10 nm, respectively.

For testing purposes, individual PtSi detectors that had been fabricated on the same wafers as the arrays were cooled to  $\sim 80$  K in a specially designed liquid-nitrogen dewar with a window permitting exposure to X-ray radiation from a tungsten source in a commercial ARACOR system. The forward and reverse current-voltage characteristics of a typical detector measured before irradiation are shown as solid curves in Figures 3-1(a) and (b), respectively. The detector exhibits ideal Schottky-barrier-diode behavior with a near-unity diode  $n$  factor. The reverse leakage current is low, and the breakdown voltage exceeds 20 V. The device was then irradiated and remeasured at  $\sim 80$  K without being allowed to warm up to a higher temperature. The dashed curves in Figures 3-1(a) and (b) represent the current-voltage characteristics measured after exposure to total-dose radiation of 10 Mrad(Si). The characteristics are essentially unchanged. For comparison, the detector photocurrent resulting from exposure to 300-K background, both before and after irradiation, is shown by the dotted curve in Figure 3-1(b). The dark current is about two orders of magnitude lower than the photocurrent, indicative of background-limited performance.

In determining the effect of radiation on detector responsivity, a prism spectrometer was used for measurements as a function of wavelength from 1 to 7  $\mu\text{m}$ , with the detector again maintained at  $\sim 80$  K throughout initial measurement, irradiation, and remeasurement. Figure 3-2 shows normalized responsivity vs spectrometer wavelength settings for a detector before and after irradiation to a total dose of 5 Mrad(Si). Within the experimental uncertainty of 1 percent (relative), there is no change in responsivity.



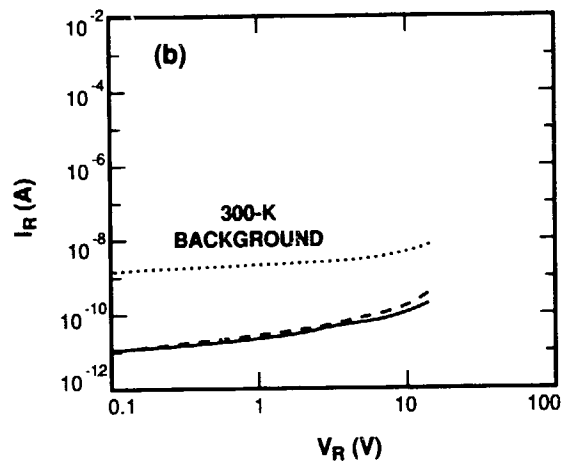
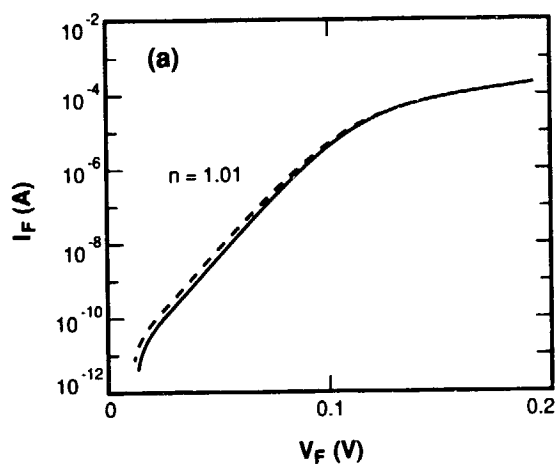


Figure 3-1. (a) Forward and (b) reverse current-voltage characteristics of PtSi detector at 80 K before irradiation (solid lines) and after irradiation of 10 Mrad(Si) (dashed lines).

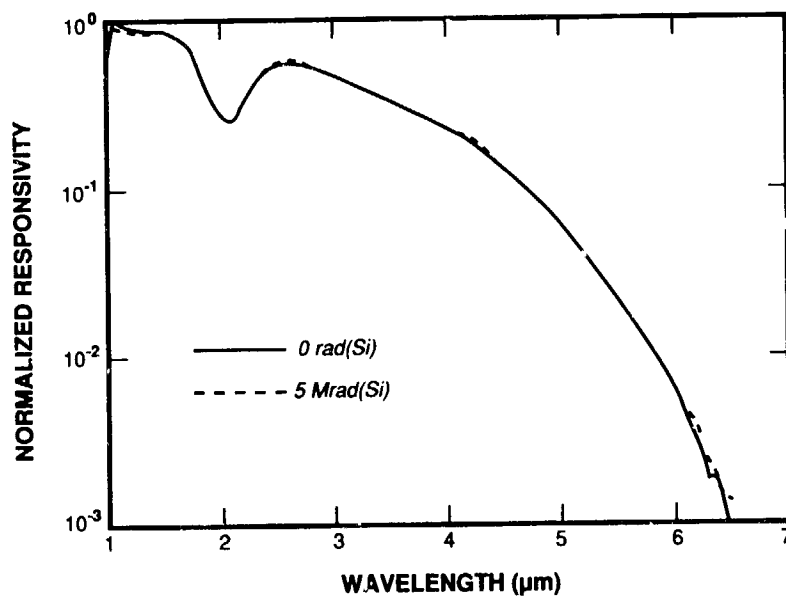


Figure 3-2. Normalized responsivity vs wavelength for PtSi detector at 80 K before and after irradiation. The normalized responsivity is the ratio of the signal from the PtSi detector to the signal from a pyroelectric detector with a flat spectral response, normalized to the highest measured value of this ratio.

The observed insensitivity of the PtSi detectors to total-dose radiation appears to be an intrinsic property of Schottky-barrier diodes. The PtSi, which is metallic, is expected to be unaffected by radiation because defect annealing occurs readily in metallically bonded structures.<sup>2</sup> Although radiation produces defects in the Si substrate that can significantly degrade the minority-carrier lifetime, these defects will not have an appreciable effect on detector performance because generation-recombination current in the space-charge region of Schottky-barrier diodes is many orders of magnitude lower than the thermionic emission current.

Total-dose radiation has a much stronger effect on MOS devices than on the PtSi detectors. Figures 3-3(a) through (c) show the results of high-frequency capacitance-voltage (C-V) measurements made before and after irradiation to a total dose of 1 Mrad(Si) on MOS capacitor structures fabricated together with the focal plane arrays. The capacitors were tested, irradiated, and retested at 80 K without being warmed to higher temperature. The poly-Si gate for the MOS devices was biased at  $V_G$  of either -10, 0, or +10 V during irradiation. As shown in Figure 3-3, the flat-band voltage shift  $\Delta V_{FB}$  is largest for  $V_G = -10$  V and smallest for  $V_G = 0$  V. In all cases, the  $\Delta V_{FB}$  values are substantially less than the shifts observed for capacitors fabricated with conventional nonhardened  $\text{SiO}_2$  gate insulators or  $\text{SiO}_2/\text{Si}_3\text{N}_4$  insulators with relatively thick (>40 nm)  $\text{SiO}_2$ .

The radiation sensitivity of conventional MOS devices results primarily because the probability of carrier trapping in the gate oxide is much higher for holes than for electrons, so that the generation of hole-electron pairs by radiation results in the trapping of net positive charge. There are three principal reasons for the reduction in radiation sensitivity achieved by using the  $\text{SiO}_2/\text{Si}_3\text{N}_4/\text{SiO}_2$  gate dielectric. First, reducing the thickness of the oxide layer decreases the number of hole-electron pairs, and therefore the concentration of trapped holes, produced by a given dose of radiation. Second, a significant fraction of the radiation-generated electrons are trapped at the  $\text{Si}_3\text{N}_4/\text{SiO}_2$  interface, where they partially neutralize the holes trapped in the  $\text{SiO}_2$ . Application of a negative gate bias during irradiation tends to sweep electrons into the underlying Si, and therefore reduces electron trapping at the interface. Consequently, the magnitude of  $\Delta V_{FB}$  produced by

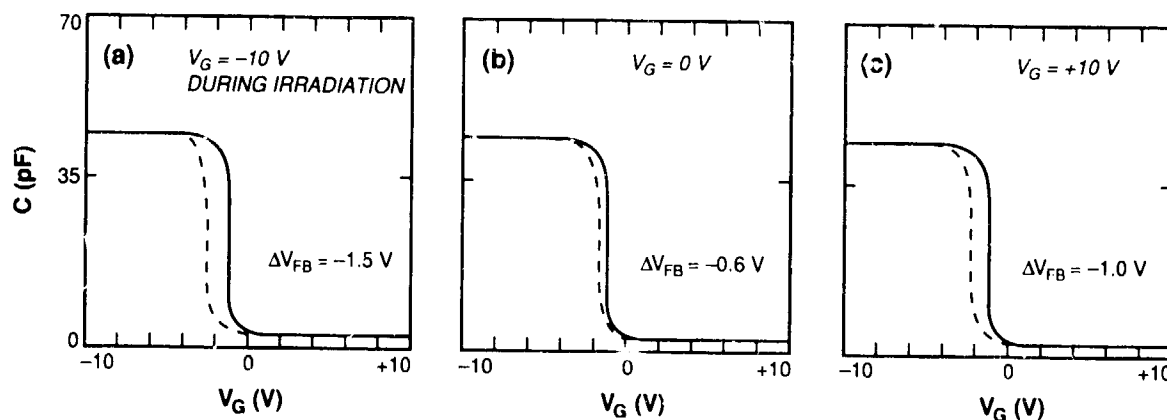


Figure 3-3. High-frequency C-V characteristics of MOS capacitors at 80 K before irradiation (solid lines) and after irradiation of 1 Mrad(Si) (dashed lines). The gate voltage  $V_G$  applied to the capacitors during irradiation and the flat-band voltage shift  $\Delta V_{FB}$  are indicated.

irradiation is larger for a negative bias than for zero bias, as shown in Figure 3-3. Third, the net charge that is trapped in the  $\text{Si}_3\text{N}_4$  is relatively small, because the probabilities of electron and hole trapping are approximately equal, so that the trapped holes and electrons neutralize each other.

To study the effect of total-dose radiation on CCD operation, the serial-channel CCDs of  $160 \times 244$  arrays were irradiated and tested at 80 K. The CCDs have an electrical input for injection of a bias charge or "fat zero."<sup>3</sup> To simulate the 300-K background signal, a bias charge corresponding to ~20 percent of the full well capacity was injected, and charge transfer efficiency (CTE) was measured with this level of bias charge. Because of carrier freezeout, the CTE is reduced to 0.9998 at 80 K compared with the room-temperature value of 0.99995. Figure 3-4 shows CCD transfer inefficiency, defined as  $(1-\text{CTE})$ , as a function of total dose. The transfer inefficiency remains nearly constant at dose levels below 0.1 Mrad(Si) but increases somewhat at higher levels. This increase is probably caused by effective changes in the operating points due to the threshold voltage shift. For an exposure of 0.8 Mrad(Si), a reduction of 30 to 40 percent in output signal level was observed, but the CCDs remained operational without any changes in operating bias.

For radiation testing of the  $160 \times 244$  imager arrays, each array is mounted in a 32-pin ceramic package with a hole in the base to permit back-side illumination. The packaged array is mounted in the liquid-nitrogen dewar and cooled to 80 K during irradiation. However, the array must be warmed up to room temperature before being transferred to a benchtop system and cooled to 80 K for imager testing. Since annealing of radiation-induced damage may occur at room temperature, the imager performance results should be considered as preliminary.

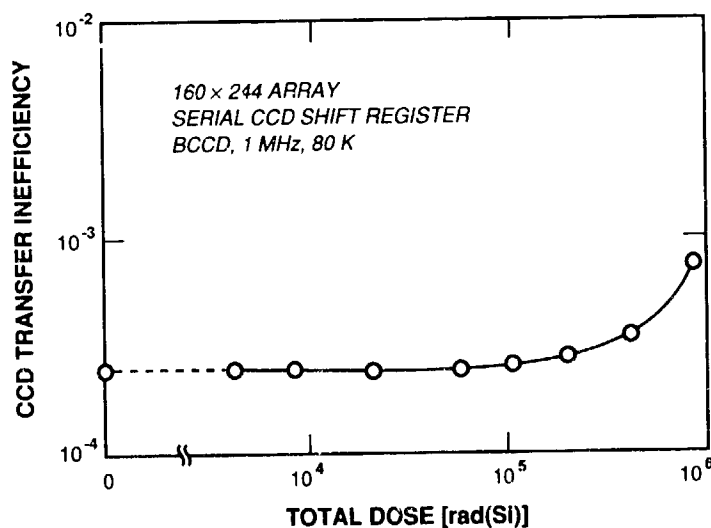


Figure 3-4. CCD transfer inefficiency as a function of total dose for the serial CCD shift register of a  $160 \times 244$  array.

Figure 3-5(a) is a high-contrast photograph of the thermal image of a 10-K 4-bar test pattern obtained, without any uniformity correction, with an array before irradiation. The imager was operated at a frame rate of 60 Hz with an f/2.35 lens. Figures 3-5(b) and (c) are images of the same pattern after the array had been irradiated to total doses of 0.2 and 0.4 Mrad(Si), respectively. These images were obtained without any adjustment of bias voltages in the CCD readout circuit. The image quality degrades somewhat at 0.4 Mrad(Si) because of degradation in CTE and background uniformity. Following 0.8-Mrad(Si) exposure, the 4-bar pattern (not shown) is still discernible although the signal is considerably reduced. These initial results encourage us to believe that high-performance PtSi imagers survivable in natural and certain enhanced radiation environments can be developed for many system applications.

B-Y. Tsaur	G.A. Lincoln
J.P. Mattia	D.F. Kolesar
C.K. Chen	R.W. Mountain

## REFERENCES

1. W.F. Kosonocky, F.V. Shallcross, T.S. Villani, and J.V. Groppe, IEEE Trans. Electron Devices **ED-32**, 1564 (1985).
2. See, for example, R.S. Nelson, *The Observation of Atomic Collisions in Crystalline Solids* (North-Holland, Amsterdam, 1968).
3. J.E. Carnes and W.F. Kosonocky, Appl. Phys. Lett. **20**, 261 (1972).

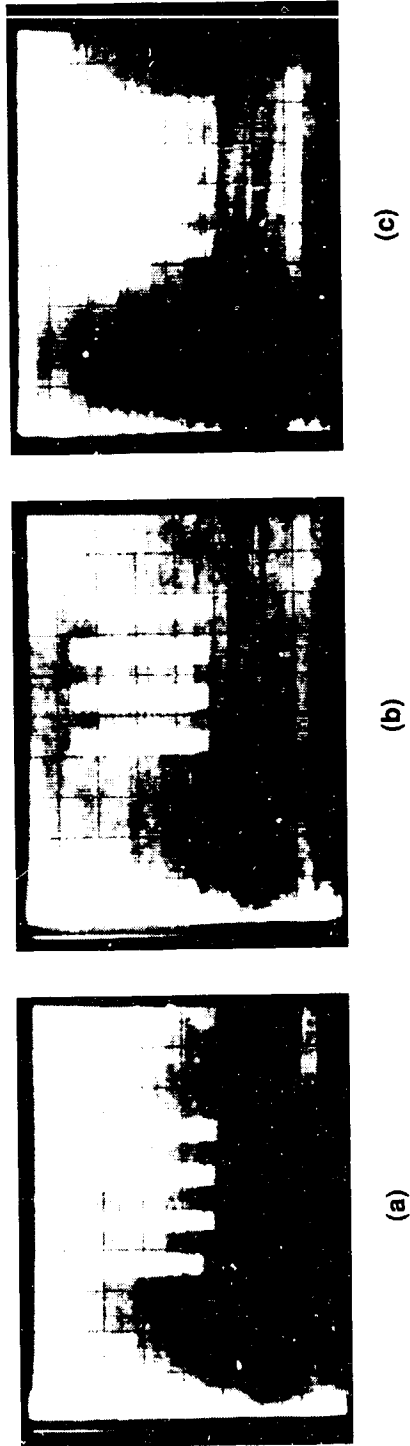


Figure 3-5. Thermal images of 10-K 4-bar test pattern obtained with a  $160 \times 244$  PtSi array (a) before irradiation, and after irradiation to a total dose of (b) 0.2 and (c) 0.4 Mrad(Si).

## 4. SUBMICROMETER TECHNOLOGY

### 4.1 ALUMINUM OXIDES AS IMAGING MATERIALS FOR 193-nm EXCIMER-LASER LITHOGRAPHY

The unique properties of excimer lasers, namely their short wavelength and high peak power, will allow many new materials to be used as photoresists for excimer lithography.<sup>1</sup> For instance, inorganic thin films such as metal oxides are candidate resists, and their extremely high etch resistance in an oxygen plasma allows even very thin (less than 100 nm) films to be used as masking layers in bilayer schemes. In this work we examine the suitability of one such compound,  $\text{AlO}_x$ , as a self-developing material for 193-nm excimer lithography.

For our bilayer resist scheme,  $\text{AlO}_x$  films are deposited on top of amorphous carbon (a-C:H) planarizing layers. Typically, a 1- $\mu\text{m}$ -thick carbon layer is deposited in a parallel-plate plasma reactor using 1-butene as the source gas.<sup>2</sup> These layers can be etched by reactive ion etching (RIE) in oxygen with a selectivity better than 40 to 1 with respect to an  $\text{AlO}_x$  etch mask.

The  $\text{AlO}_x$  films are deposited by ion-beam deposition, e-beam evaporation, or sputter deposition. The film composition is analyzed by Auger electron spectroscopy and X-ray photoelectron spectroscopy (XPS). Because of uncertainty in the Al and O sensitivity factors for these  $\text{AlO}_x$  films, the x's obtained from the data should be viewed as relative values rather than absolute atomic concentration ratios.

The film composition is independent of the deposition technique, and depends only on the rates of arrival of the deposited material and the reactive gas species at the substrate surface. By controlling the oxygen background pressure and the deposition rate,  $\text{AlO}_x$  films with compositions varying from metallic to fully oxidized Al can be formed, as shown in Figure 4-1. The arrival rates of oxygen and Al are calculated from the oxygen partial pressure and the  $\text{AlO}_x$  deposition rate, respectively. The amount of oxygen incorporated in the film increases with the ratio of oxygen to Al arrival rates at the surface. With a low partial pressure of oxygen and/or fast deposition rate, the film is metallic Al. With a high oxygen partial pressure and/or low deposition rate, fully oxidized  $\text{AlO}_x$  is formed as long as the oxygen arrival rate is more than 20 times the  $\text{AlO}_x$  deposition rate.

In the intermediate range where the oxygen arrival rate is between 1 and 15 times the  $\text{AlO}_x$  deposition rate, partially oxidized Al films are generated. The  $\text{AlO}_x$  films deposited under these conditions show two Al Auger peaks, with the metallic Al peak at 67 eV and the oxide peak at 55 eV. The ratio of the peak heights of oxidized to metallic Al varies depending on the ratio of oxygen to Al arrival rates. The presence of both metallic Al and oxide in the films is also verified by XPS which shows an Al peak at 71 eV and an oxide peak at 74 eV. Such films also act as good imaging layers when exposed to 193-nm excimer laser light.

The  $\text{AlO}_x$  films are exposed in a self-developing mode with a 193-nm excimer laser in projection. The single-pulse self-development fluence in air varies from 20 to 1000  $\text{mJ}/\text{cm}^2$ , depending on the film thickness, the hardness of the a-C:H layer underneath, and the composition of the film. The

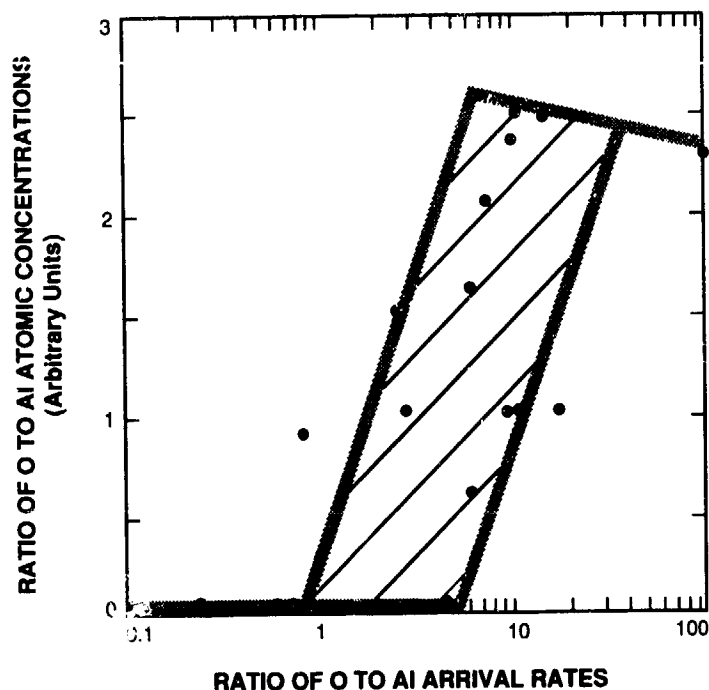


Figure 4-1. Atomic compositions of  $\text{AlO}_x$  obtained from Auger measurements as a function of the ratio of oxygen to Al arrival rates. The data include films formed by ion-beam deposition, e-beam evaporation, and sputter deposition. The shaded area represents films that contain a mixture of Al and oxide; these provide good imaging quality at 193 nm.

effect of the film composition on the fluence necessary for self-development is attributed mainly to changes in the optical properties of the films. As shown in Figure 4-2, the one-pulse self-development threshold energy  $E_{th}$  is similar for films with different compositions when the film reflectivity is taken into account. These  $\text{AlO}_x$  layers are typically 50 nm thick and are prepared by ion-beam deposition with a partial pressure of  $\text{O}_2$  varying from  $2 \times 10^{-6}$  to  $9 \times 10^{-5}$  Torr. The  $\text{AlO}_x$  film reflectivity at 193 nm varies from 60 to 6 percent as the film composition is changed from Al to fully oxidized  $\text{AlO}_x$ . Although the *absorbed* fluence (after correction for the film reflectivity) required for self-development does not change much with film composition, other lithographic properties are strongly dependent on the composition. In particular, good adhesion and submicrometer resolution are obtained only with partially oxidized  $\text{AlO}_x$ . The self-development process of  $\text{AlO}_x$  is highly nonlinear with fluence, and these films cannot be patterned by using multiple pulses at a lower fluence. The imaging contrast of  $\text{AlO}_x$  at 193 nm is found to be around 4.3 for one-pulse exposures. Dreyfus *et al.* suggested<sup>3,4</sup> that self-development of sapphire using 193-nm excimer laser is a photochemical etching process as it takes place at about 600 K, a temperature well below that necessary for thermal evaporation. Our estimates of the temperature rise at threshold for self-developing  $\text{AlO}_x$  thin films on a-C:H yield similar results. Taking into account the absorptivity of  $\text{AlO}_x$  and the absorption length of a-C:H at 193 nm, we calculate a temperature rise of about 500 K. This value is

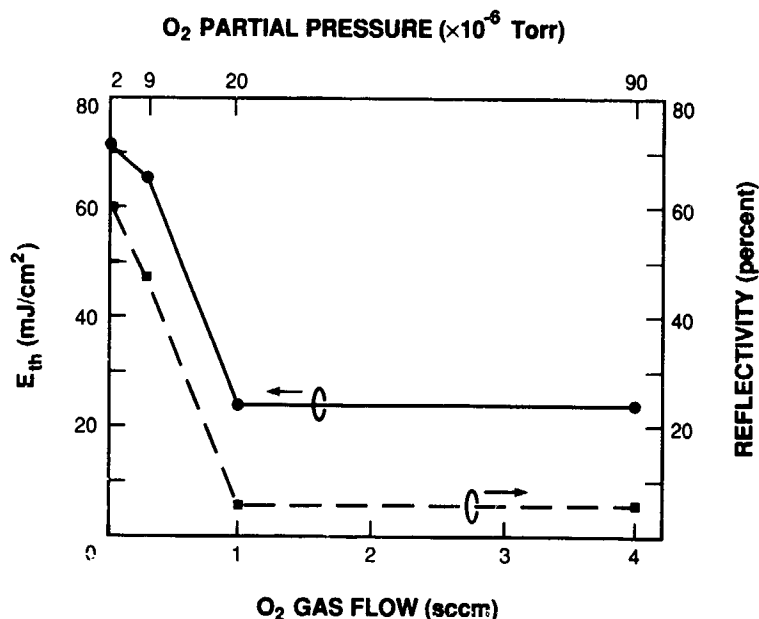


Figure 4-2. One-pulse self-development threshold energy  $E_{th}$  and reflectivity of ion-beam-deposited  $AlO_x$  films as a function of the partial pressure of  $O_2$  during deposition.

an upper limit, since our calculations neglect the thermal diffusivity of the a-C:H film. We conclude that the mechanism of 193-nm-induced etching of  $AlO_x$  thin films has a dominant photochemical component over a wide range of stoichiometries.

Figure 4-3 shows the patterning of an  $AlO_x$ /a-C:H bilayer resist. A 60-nm-thick  $AlO_x$  film is deposited on top of the 1.3- $\mu$ m-thick a-C:H layer by ion-beam deposition. The  $AlO_x$  imaging layer is self-developed using 193-nm excimer laser projection exposure with 36 $\times$  reduction and a numerical aperture of 0.5. The fluence is 528 mJ/cm<sup>2</sup>. Following exposure, the pattern is transferred into the a-C:H layer by  $O_2$  RIE, producing posts typically 0.25  $\mu$ m wide and 0.5  $\mu$ m deep, but some as narrow as 0.1  $\mu$ m.

In summary, the  $AlO_x$  layers that provide good imaging quality have a mixture of metallic Al and oxide. The single-pulse self-development fluence is similar for films with different compositions when the film reflectivity is taken into account. Features as small as 0.1  $\mu$ m can be patterned on these films in projection, and transferred through a 1- $\mu$ m-thick a-C:H underlayer with vertical profiles.

S.W. Pang

R.R. Kunz

M. Rothschild

R.B. Goodman

M.W. Horn



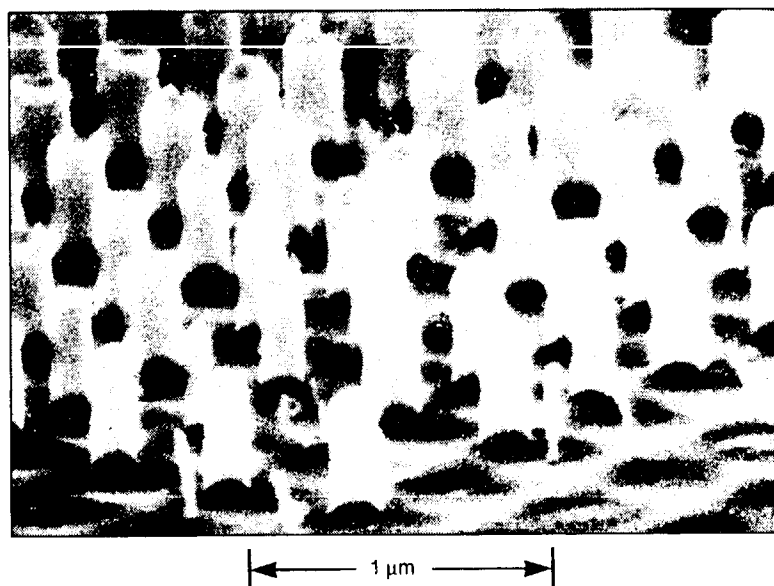


Figure 4-3. Scanning electron micrograph of  $\text{AlO}_x$  on top of a-C:H. The  $\text{AlO}_x$  layer was patterned in air with one pulse of  $528 \text{ mJ/cm}^2$  using a 193-nm excimer laser. The a-C:H layer was reactive-ion etched in  $\text{O}_2$  at 250 V.

#### 4.2 PLANARIZING a-C:H AND $\text{SiO}_2$ FILMS PREPARED BY BIAS ELECTRON CYCLOTRON RESONANCE PLASMA DEPOSITION

The topography introduced by multilevel interconnection schemes has been shown to cause problems both because of depth-of-field limitations during lithography and because of step-coverage requirements in metallization. Low-temperature ( $<400^\circ\text{C}$ ) dry planarization techniques are advantageous owing to the need to use aluminum and, more generally, the desire to minimize the thermal budget, as well as reliability and environmental concerns associated with wet processing. We report here the room-temperature bias electron cyclotron resonance (bias-ECR) plasma deposition<sup>5,6</sup> of both carbon- and silicon-based planarization materials.

The bias-ECR system consists of a 2.45-GHz microwave power supply, an ECR cavity, two electromagnets with adjustable spacing and power, and a substrate stage connected to a 13.56-MHz RF power source. Gases can be introduced into the cavity directly and just above the substrate through a dispersing ring. For the films described in this report, Ar and  $\text{N}_2\text{O}$  are introduced directly into the ECR cavity, while the hydrocarbon gases and the 5-percent  $\text{SiH}_4$  diluted in  $\text{N}_2$  are introduced through the dispersing ring.

The flexibility of the bias-ECR planarization technique is demonstrated by depositing planarizing amorphous hydrogenated carbon (a-C:H) films from both 1-butene ( $\text{C}_4\text{H}_8$ ) and 1,3-butadiene ( $\text{C}_4\text{H}_6$ ). Figures 4-4(a) through (c) show a sequence of cross-sectional scanning electron micrographs

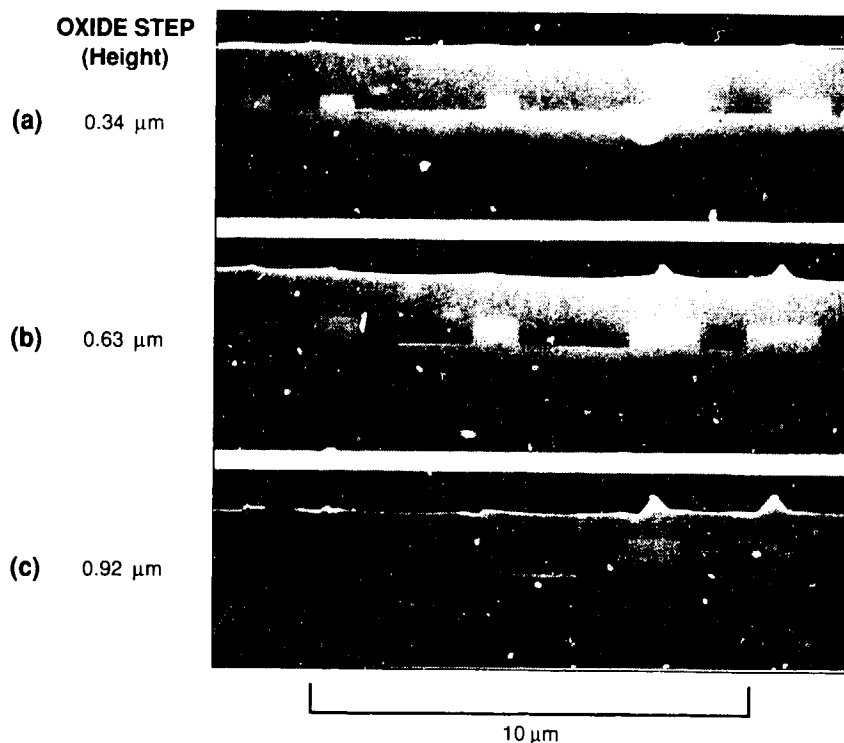
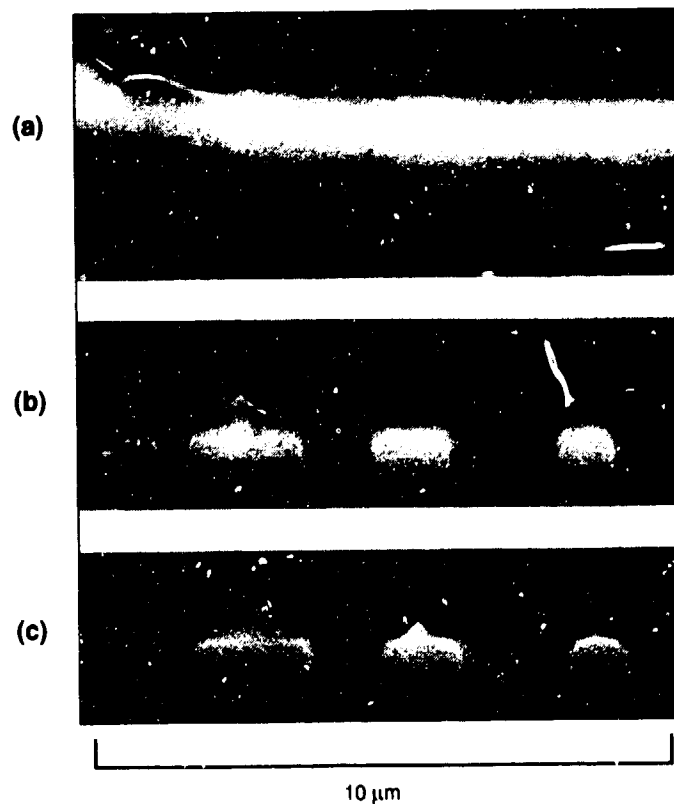


Figure 4-4. Sequence of cross-sectional scanning electron micrographs showing the change in planarization with aspect ratio for an a-C:H film deposited on oxide substrates with step height of (a) 0.34, (b) 0.63, and (c) 0.92  $\mu\text{m}$ .

which illustrate how oxide features with various aspect ratios are planarized. Thermal oxide grown on silicon substrates to a thickness of 2  $\mu\text{m}$  is patterned by RIE in  $\text{CF}_4$ . For a 1.6- $\mu\text{m}$ -thick a-C:H film, planarization is nearly complete for steps 0.34  $\mu\text{m}$  deep and 1.5  $\mu\text{m}$  wide, as shown in Figure 4-4(a). Figure 4-4(c) shows better than 95-percent planarization for the features with aspect ratios of approximately 1. This particular film is deposited using 10-sccm  $\text{C}_4\text{H}_8$  and 144-sccm Ar at a total pressure of 5.7 mTorr. The RF power is 300 W and the dc bias is 300 V. The microwave power is 750 W, and the electromagnet power is 3 kW for the top magnet and 2 kW for the bottom magnet. For these conditions, the deposition rate is 40 nm/min. The etch rates of these a-C:H films in  $\text{O}_2$  RIE at 250 V are about 20 nm/min, comparable to hard-baked photoresist. Planarizing a-C:H layers could be deposited on top of a high-quality ECR-plasma-deposited conformal dielectric ( $\text{SiO}_2$  or  $\text{Si}_3\text{N}_4$ ) as a dry alternative to spin-on-polymer/etchback planarization techniques.

$\text{SiO}_2$  planarizing layers are deposited from Ar,  $\text{N}_2\text{O}$ , and 5-percent  $\text{SiH}_4$  diluted in  $\text{N}_2$ . The film thickness and index of refraction are measured ellipsometrically at 632.8 nm. The deposition rate increases and the refractive index decreases with increasing  $\text{N}_2\text{O}$  and Ar flow rate. The increase in deposition rate with  $\text{N}_2\text{O}$  seems to indicate that an increase in available oxygen results in a faster deposition rate, and that the rate limiting factor for oxide deposition at a preset dilute  $\text{SiH}_4$  flow rate



**Figure 4-5.** Cross-sectional scanning electron micrographs of planarizing oxides deposited on 0.9- $\mu\text{m}$  silicon steps of varying aspect ratio for three different deposition conditions. For all three films, the ECR power was 150 W and the silane flow was 100 sccm. In (a), the RF power was 300 W, the  $\text{N}_2\text{O}$  flow rate was 72 sccm, the Ar flow rate was 58 sccm, and the deposition time was 90 min. In (b), the RF power was increased to 400 W, the Ar flow rate was increased to 87 sccm, and the deposition time was halved to 45 min. In (c), the RF power and Ar flow rate were identical to those in (a), but the  $\text{N}_2\text{O}$  flow rate and deposition time were halved to 36 sccm and 45 min, respectively.

is the availability of atomic oxygen. The increase in deposition rate with Ar could be due to an increase in ionization efficiency for  $N_2O$  or  $SiH_4$  caused by collisions with excited or ionized Ar atoms. For films with a refractive index close to that of thermal oxide (1.465), there is a decrease in refractive index with increasing deposition rate. This is tentatively attributed to a small decrease in film density.

Figures 4-5(a) through (c) illustrate oxide planarization for films deposited on top of 0.9- $\mu$ m-deep silicon steps of varying aspect ratios under three different deposition conditions. For all three films, the microwave power is 750 W and the 5-percent  $SiH_4$  flow rate is 100 sccm. Figure 4-5(a) shows >95-percent planarization for Si features 0.9  $\mu$ m deep and <1.5  $\mu$ m wide using a film 2.3  $\mu$ m thick. For this film, the Ar flow rate is 58 sccm, the  $N_2O$  flow rate is 72 sccm, the RF power is 300 W, and the deposition time is 90 min. The film thickness needed for planarization can be adjusted by carefully balancing the etch rate with the deposition rate, as illustrated in Figures 4-5(b) and (c). The planarization in Figure 4-5(b) is accomplished using the conditions described for the oxide of Figure 4-5(a) except that the Ar flow rate and the RF power are increased. The result is a thinner oxide and a shorter planarization time (45 min). Figure 4-5(c) shows an even thinner planarizing film deposited for 45 min under the same conditions as listed for Figure 4-5(a) except with a lower  $N_2O$  flow rate. These films are characterized using Auger electron spectroscopy and found to have stoichiometry indistinguishable from that of a thermally grown gate oxide. The index of refraction for these films ranges from 1.43 to 1.47 as measured by an ellipsometer, and the etch rates in buffered HF are found to be about 21 nm/min as compared with a thermal oxide whose etch rate is 15 nm/min.

Bias-ECR plasma deposition offers several advantages over bias-sputtered deposition<sup>7</sup> or bias chemical vapor deposition (bias-CVD)<sup>8</sup> for planarization. As demonstrated in Figures 4-4 and 4-5, bias-ECR plasma deposition is able to planarize submicrometer surface topography containing features of both high and low aspect ratio without void formation, which is much more difficult to achieve with the other two techniques. The absence of voids in the ECR-deposited films is a consequence of the narrow divergence of ions and depositing species resulting from low deposition pressures. Another advantage of bias-ECR plasma deposition is that the time required for planarization is shorter than that in bias-sputter deposition or bias-CVD planarization techniques because of the enhanced dissociation of reactive species and the increased flux of ions available for etching. In addition, as shown in this report, bias-ECR plasma deposition enables planarization of a wide range of materials, even as different structurally and chemically as a-C:H and  $SiO_2$ .

In summary, a-C:H planarization layers have been deposited at room temperature. Oxide and aluminum features 1  $\mu$ m deep by 2  $\mu$ m wide are planarized to less than 50 nm in height using 1.2- $\mu$ m-thick films. Planarizing  $SiO_2$  layers have been deposited over a variety of substrates, with the same stoichiometry as thermally grown gate oxide. Films nominally 1.5  $\mu$ m thick can reduce 800-nm-deep topography to less than 50 nm for lines as wide as 3  $\mu$ m. The deposition time and film thickness necessary for planarization of a feature of given aspect ratio can be tailored by varying the deposition conditions, including gas composition, pressure, microwave power and coupling, electron-magnet power and position, and RF power applied to the substrate stage.

M.W. Horn  
S.W. Pang

M. Rothschild  
G.A. Ditmer

### 4.3 ELECTRICAL, CRYSTALLOGRAPHIC, AND OPTICAL PROPERTIES OF ArF-LASER-MODIFIED DIAMOND SURFACES

Carbon can exist in several condensed phases. One phase, diamond, is transparent, insulating, and chemically inert.<sup>9</sup> In contrast, graphite and graphite-like phases are opaque, conductive, and chemically more reactive.<sup>10</sup> Carbon can be transformed between these phases by the application of heat and pressure. Laser radiation has been used to produce these transformations. This report contains a discussion of ArF-laser modification of a diamond layer into a composite structure of diamond and graphite-like phases which has some of the characteristics of both diamond and graphite.

These layers have been characterized using electrical, optical, and crystallographic techniques. The thickness of the layers was determined to be 40 to 60 nm from conductance measurements as a function of etch depth, as shown in Figure 4-6. The resistance was found to be anisotropic. The low resistance was measured to be  $4$  to  $10 \times 10^{-4} \Omega \text{ cm}$  along one of the  $\langle 110 \rangle$  in-plane axes, and the high in-plane resistance was found to be  $90^\circ$  from the direction of low resistance, as shown by the inset in Figure 4-6. The  $\langle 110 \rangle$  axes are expected to be equivalent for  $\{100\}$ -oriented substrates, but this is not the case experimentally. The axis of low resistance is not defined by polarization or angle

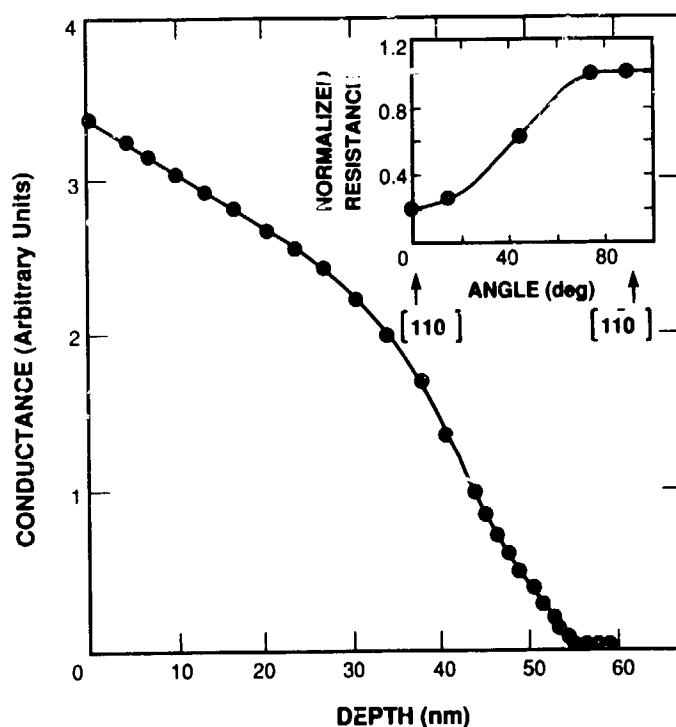


Figure 4-6. Conductance of the modified diamond layer on  $\{100\}$ -oriented substrates in the low resistance direction as a function of etch depth. Ion-beam-assisted etching was used to etch the modified layer. The inset shows the typical resistance of the layer as a function of angle relative to one of the in-plane  $\langle 110 \rangle$  axes. The solid circles are the data, and the solid lines are guides to the eye.

of incidence of the laser radiation, but presumably is determined by some property of the substrate. When the surface of type IIb (semiconducting) diamond is modified, the layer forms an ohmic contact to the diamond.

The modified surface of natural type IIa or IIb diamond will polarize both the transmitted and reflected radiation. A minimum in transmittance is obtained when the electric vector of the incident optical radiation coincides with the direction of minimum dc resistance. The ratio of maximum to minimum transmittance as a function of photon energy is shown in Figure 4-7. When the modified regions are examined under polarized visible light, maximum reflectance is observed when the polarization is adjusted for minimum transmittance. These results are consistent with the transmittance and reflectance of wire-grid and graphite polarizers. However, wire-grid polarizers become inefficient for wavelengths less than  $1\text{ }\mu\text{m}$  (see Reference 11), while the degree of polarization of modified diamond layers increases toward shorter wavelengths down to  $250\text{ nm}$ . Backscattering Raman spectroscopy, using  $514\text{-nm}$  radiation from an argon-ion laser, shows only the  $1332\text{-cm}^{-1}$  Raman line of diamond, which is thought to originate primarily from the diamond substrate.

ArF-laser-modified layers on  $\{100\}$  substrates have been characterized by transmission and reflection electron diffraction as well as transmission electron microscopy. For the transmission experiments, the substrates with modified layers were thinned from the back by laser ablation and

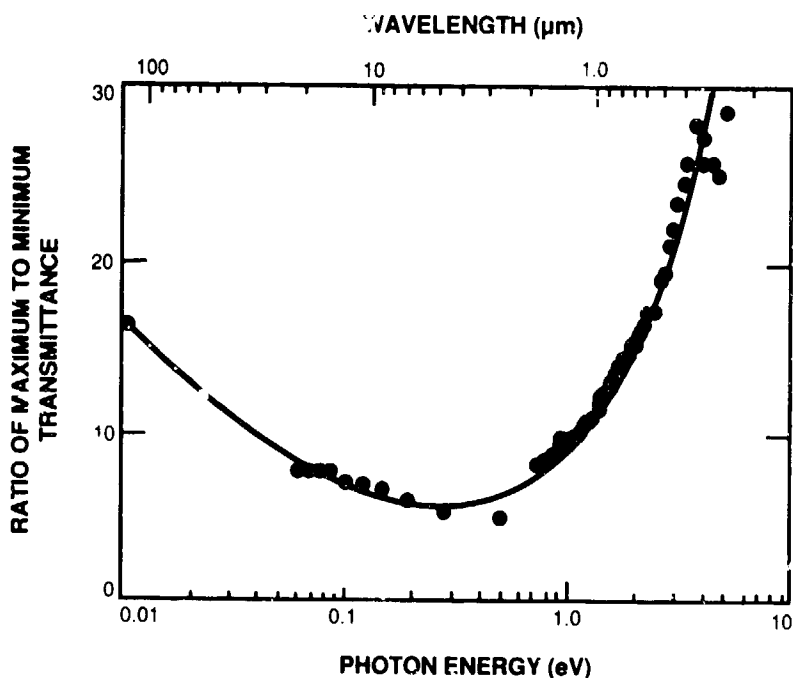
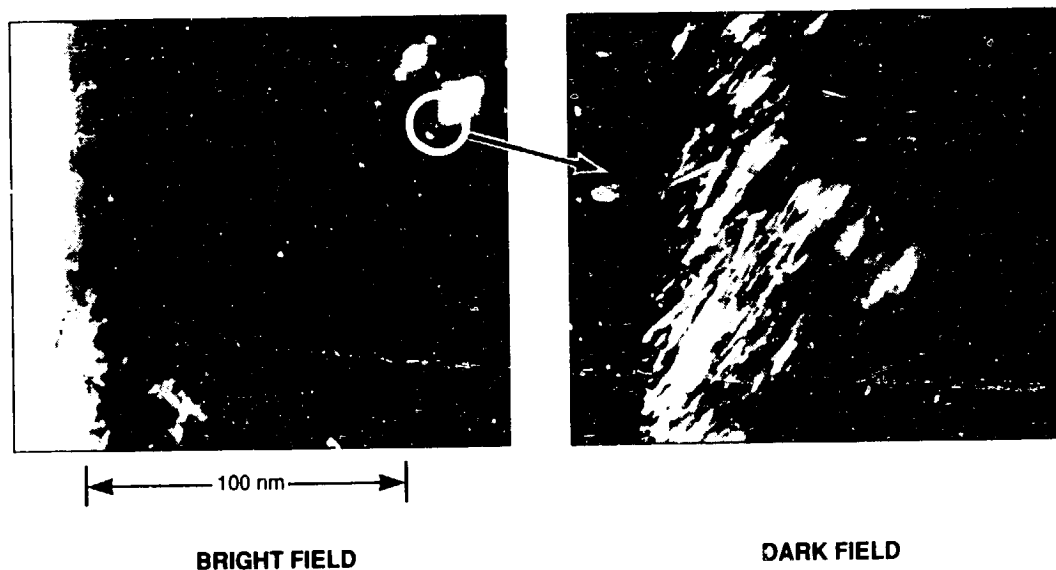


Figure 4-7. Ratio of the maximum to minimum transmittance of linearly polarized radiation through the modified layer on  $\{100\}$  substrates as a function of photon energy and wavelength. The solid circles are the data, and the solid line is a guide to the eye.

ion-beam-assisted etching. Electron-diffraction patterns indicate that the modified layers are a mixture of diamond and unidentified carbon phases. The first-order diffraction patterns from the modified material correspond to lattice spacings of 0.123, 0.305, and 0.334 nm, with a  $\pm 0.003$ -nm uncertainty. The diffraction patterns of the diamond, the other phases, and double diffraction of this mixture always appear together when the electron beam is normal to the  $\{100\}$  diamond planes. This implies that the modified layer is a composite structure of diamond and other phases. When the sample is rotated about the  $[110]$  axis, diffraction of the other phases disappears, indicating that these phases are epitaxial to the diamond. In some of the laser-modified samples examined by transmission electron diffraction, the 0.334-nm lattice spacing was not present. Reflection-electron diffraction, which probes only the first few nanometers of the surface, shows the diffraction pattern of only diamond. This suggests that the first few nanometers of the modified surface consist primarily of diamond. Bright- and dark-field transmission electron micrographs of a laser-modified diamond surface are shown in Figure 4-8. In dark field, the modified regions appear as lines parallel to one of the in-plane  $\langle 110 \rangle$  axes and perpendicular to the direction of lowest resistance.

The non-diamond phases are believed to consist primarily of a compressed epitaxial graphite-like material that is stabilized by the presence of diamond. It is unaffected by additional ArF-laser radiation. Even when encased in a protective polymer layer and held at  $1200^{\circ}\text{C}$  for 1 h or at  $1800^{\circ}\text{C}$  for 10 s, the modified layer is still present after the carbonized polymer is removed in hot  $\text{H}_2\text{SO}_4$  and  $\text{CrO}_3$  solution.



*Figure 4-8. Bright- and dark-field transmission electron micrographs of laser-modified  $\{100\}$  diamond. The inset in the bright-field micrograph shows the electron diffraction pattern and the portion of that pattern used to form the dark-field image. Transmission electron micrographs of the unmodified diamond used in these experiments show no defects except for a very occasional dislocation.*

In summary, the laser-modified layers can be important as stable ohmic contacts to type IIb diamond. They can withstand 1800°C, and are not attacked by either helium-oxygen plasma or hot H<sub>2</sub>SO<sub>4</sub> and CrO<sub>3</sub> solution. The modified layers have resistivity of the order of 10<sup>-4</sup> Ω cm and will polarize light. Transmission electron diffraction indicates that they are composed of diamond and graphite-like material.

M.W. Geis	K.A. McIntosh
M. Rothschild	N.N. Efremow
R.R. Kunz	J.J. Zayhowski
R.L. Aggarwal	D.J. Ehrlich
K.F. Wall	J.E. Butler
C.D. Parker	

### REFERENCES

1. M. Rothschild and D.J. Ehrlich, J. Vac. Sci. Technol. B 6, 1 (1988), DTIC AD-A194633.
2. Solid State Research Report, Lincoln Laboratory, MIT (1989:1), p. 43.
3. R.W. Dreyfus, R. Kelly, and R.E. Walkup, Appl. Phys. Lett. 49, 1478 (1986).
4. R.W. Dreyfus, F.A. McDonald, and R.J. von Gutfeld, J. Vac. Sci. Technol. B 5, 1521 (1987).
5. K. Machida and H. Oikawa, J. Vac. Sci. Technol. B 4, 818 (1986).
6. K. Machida and H. Oikawa, in *1987 Symposium on VLSI Technology, Digest of Technical Papers* (Japan Society of Applied Physics, Tokyo, Japan, 1987), p. 69.
7. C.Y. Ting, V.J. Vivalda, and H.G. Schaefer, J. Vac. Sci. Technol. 15, 1105 (1978).
8. E.J. McInerney and S.C. Avanzino, IEEE Trans. Electron Devices ED-34, 615 (1987).
9. J.E. Field, *The Properties of Diamond* (Academic Press, New York, 1979).
10. C.L. Mantell, *Carbon and Graphite Handbook* (Robert I. Krieger Publishing, Huntington, New York, 1979).
11. W.G. Driscoll and W. Vaughan, *Handbook of Optics* (McGraw-Hill, New York, 1978), Chapter 10, pp. 71-77.



## 5. MICROELECTRONICS

### 5.1 CCD CAMERA DEVELOPED FOR WAVEFRONT-SENSOR APPLICATIONS

Charge-coupled-device (CCD) cameras have been built for use in a Hartman<sup>1</sup> wavefront sensor in an adaptive optics system. This particular application required two important camera characteristics: low noise level at high frame rates, and near-reflection-limited quantum efficiency for low-light-level detection. A pair of such CCD cameras enabled the adaptive optics system to perform real-time atmospheric compensation with photon-limited noise statistics down to light levels as low as 3000 photons per pixel at 488 nm.

Figure 5-1 is a photograph of the CCD camera. The camera consists of a focal-plane board and a camera chassis. Separation of the camera into two parts allows the focal-plane board to be inserted easily into the optical path of the signal. Also, the camera chassis containing the heat-generating

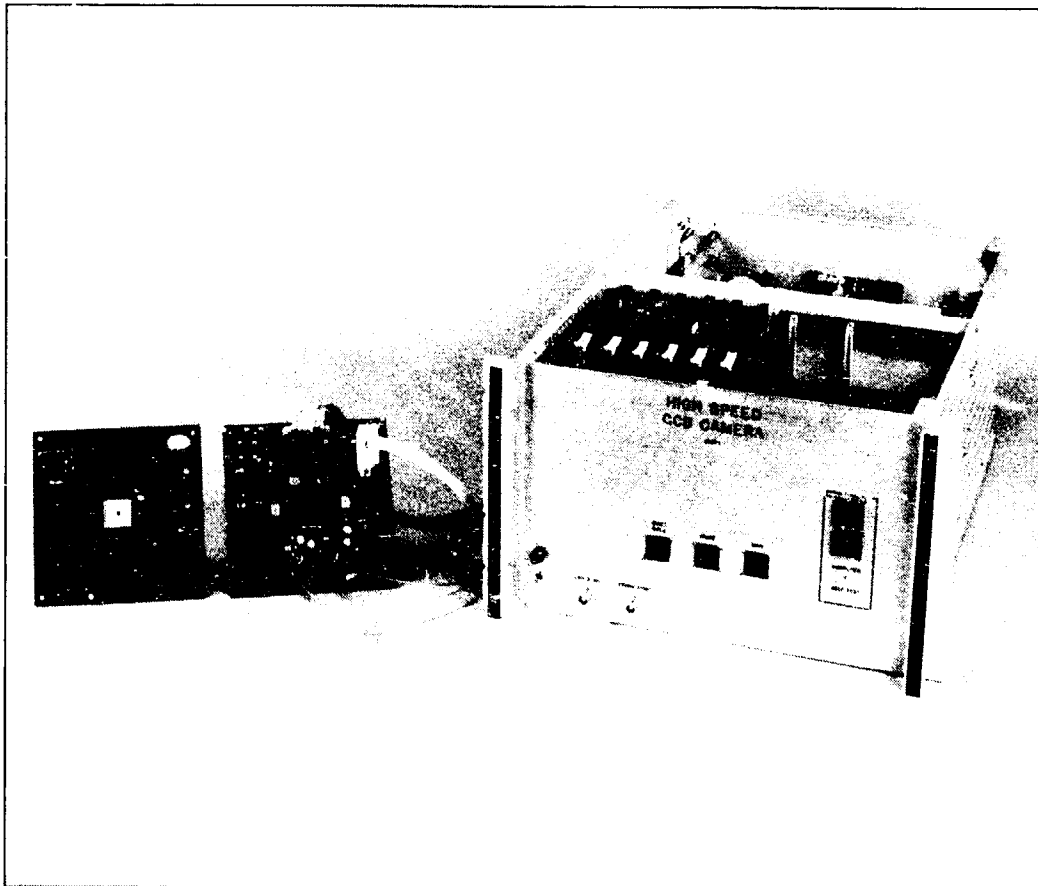


Figure 5-1. Photograph of the CCD camera showing the focal-plane board on the left and camera chassis on the right. Both front and back views of the focal-plane board are shown.

electronics can be placed far enough away to avoid unwanted distortion to the incoming wavefront. The focal-plane board contains a back-illuminated  $64 \times 64$ -pixel frame-transfer CCD imager<sup>2</sup> for signal detection. Also on the board are clock drivers for the imaging, frame-store, and output register arrays, output preamplifiers to raise the signal above the noise level of following electronics, and a thermoelectric cooler to stabilize the CCD temperature. Contained in the camera chassis are the timing logic, correlated double-samplers, A/D converters, reformatting memory, power supplies, and variable-gain amplifiers. The camera system is able to drive the CCD at 2000 frames per second while keeping the noise low at 35 noise-equivalent electrons rms. This frame rate allows the optics to adapt to distortions of a wavefront with response times of the order of a few milliseconds.

Back illumination maximizes quantum efficiency by giving essentially a 100-percent fill factor for photon capture and providing a planar surface for efficient application of antireflection (AR) coatings to minimize reflection losses. Details of the processing necessary to fabricate thinned back-illuminated imagers have been described previously.<sup>3,4</sup> Figure 5-2 shows the quantum efficiency vs wavelength for a back-illuminated CCD imager with an AR coating optimized for wavelengths between 600 and 700 nm. The maximum quantum efficiency achieved (88 percent) is influenced by the AR coating chosen. Sputtered silicon dioxide was used for the AR coating on the present device because of availability and ease of processing. An ideal coating would have an index of refraction of 2.0, which is the geometric mean of silicon and air. The index of refraction of silicon dioxide is approximately 1.49 over the wavelengths of interest.

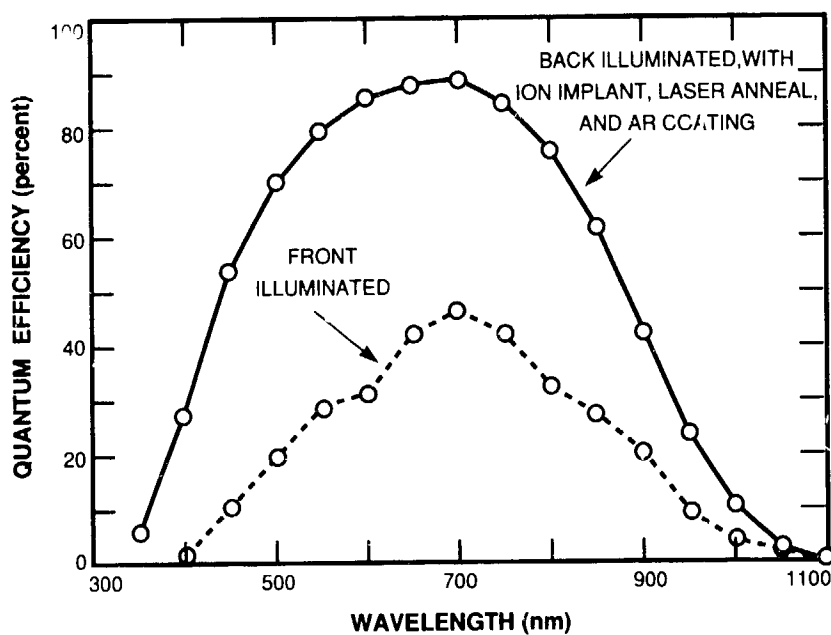


Figure 5-2. Quantum efficiency vs wavelength for the  $64 \times 64$ -pixel CCD imager for both back and front illumination.

One further advantage of back-illuminated CCDs for a Hartman-sensor application is the smooth interpixel and intrapixel spatial response to a point source of light. The smooth response is the result of an unobstructed optical path to the point of detection and a planar surface for entry of the light signal into the CCD, and is required for the implementation of the piecewise-linear fitting algorithm used for the Hartman-sensor output data. Interpixel signal variation is less than  $\pm 4$  percent for an imager uniformly illuminated by 500-nm-wavelength light.

Figure 5-3 shows the configuration of a Hartman sensor.<sup>1</sup> The CCD camera serves as the two-dimensional detector array in the sensor. The local wavefront at each lenslet of a  $16 \times 16$  array is focused onto a  $4 \times 4$ -pixel subaperture on the CCD imaging array. A change in phase gradient of

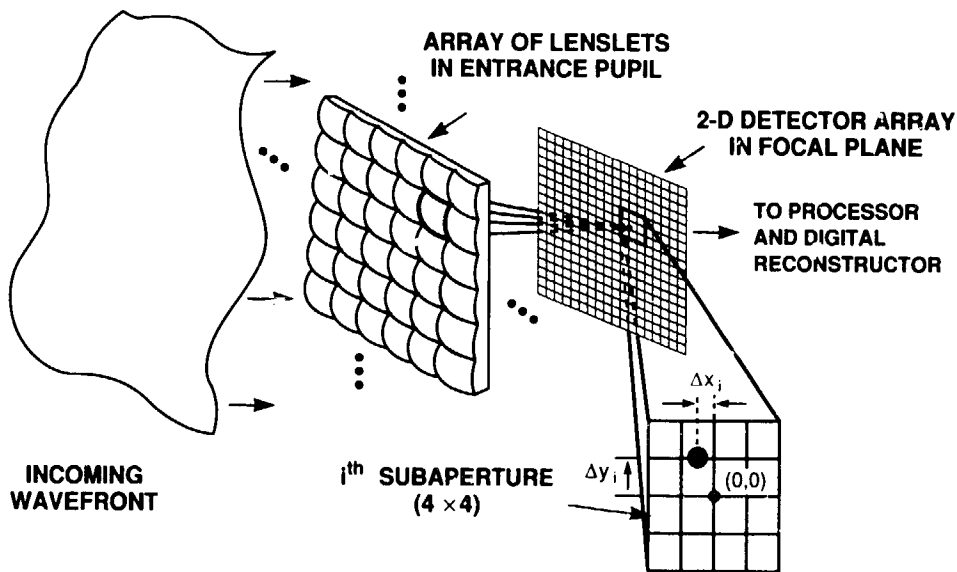


Figure 5-3. Configuration of the Hartman sensor.

the incoming wavefront across the lenslet array is detected by the displacement of the focused spot centroid from the center of the  $4 \times 4$ -pixel subaperture. The focused spot position is used to calculate a local phase gradient from which the phase can then be extracted. The x and y phase gradients are measured simultaneously on separate cameras in order to increase the frame rate by a factor of four. In each camera, the  $4 \times 4$ -pixel subaperture is reduced to a  $4 \times 1$ -pixel array by summing together the pixels in the direction opposite to the measured phase gradient. Output from the Hartman sensor is used in an adaptive optics system to correct for disturbances in the incoming wavefront. Figure 5-4 gives the tilt noise vs photons per subaperture for the Hartman sensor. Local distortion in the wavefront can be detected only if it is above the tilt noise, which is a function of the camera noise and the Poisson noise of the light signal.

R.K. Reich	B.W. Johnson
W.H. McGonagle	J.C. Twichell
C.M. Huang	H.T. Barclay

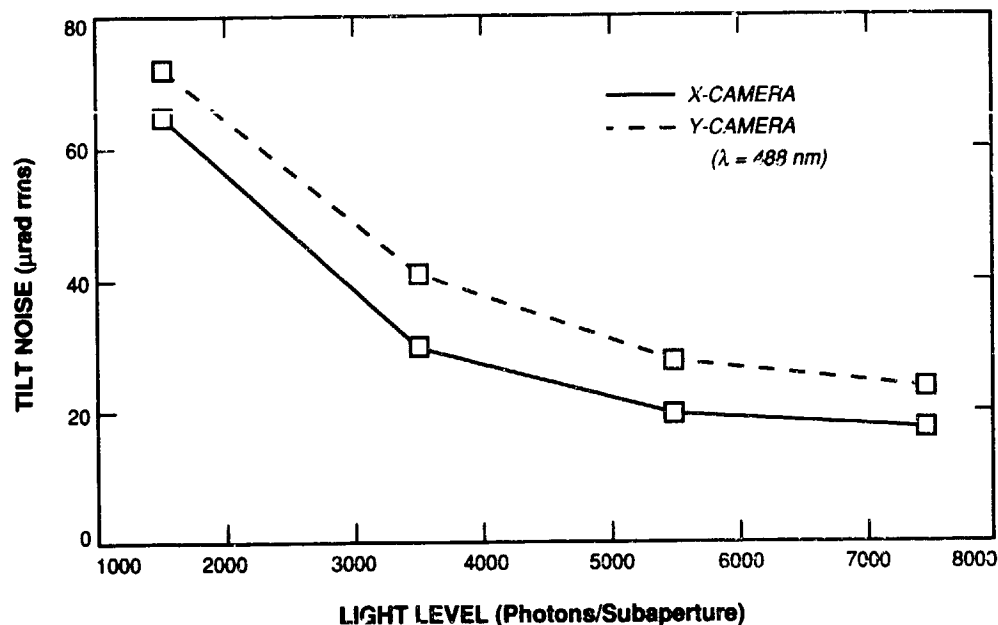


Figure 5-4. Tilt noise vs photons per subaperture of the Hartman sensor using the CCD camera.

## 5.2 SURFACE-STATE DARK-CURRENT SUPPRESSION IN CCDs

The major contributor to dark current in CCDs is often the generation current produced by surface states at the oxide-silicon interface. One method for suppressing this current in an n-channel buried-channel CCD is to set the low level of the gate clock voltage to a value that causes the surface to invert.<sup>5</sup> This means that a layer of holes is formed at the surface under those gates that are set to their low state. A high density of surface holes suppresses the emission of electrons into the conduction band from midgap states. However, in three- and four-phase CCDs at least one gate must be at a high level (and the surface under it therefore not inverted) in order to store charge packets. Because of this, it is widely believed that complete suppression of surface-state dark current is not possible in these devices without resorting to special techniques such as selective implants.<sup>6</sup> We will describe here a new technique for suppression of surface-state dark current which relies on the dynamical properties of the semiconductor surface and can be applied to a CCD without physically modifying the device.

The technique to be described is based on the time dependence of the generation rate at surface states after a surface has been switched from inversion to depletion.<sup>7</sup> For a depleted surface, the electron generation rate for states at energy  $E$  in the forbidden gap  $G(E,t)$  is given by

$$G(E,t) = e_n(E) n_{ss}(E,t) \quad (5-1)$$

where  $n_{ss}(E,t)$  is the density per unit energy per unit area of filled surface states, and  $e_n(E)$  is the electron emission rate for a state at energy  $E$ . When the surface is inverted,  $n_{ss} = 0$  over essentially

the entire bandgap, and the generation current is negligible. However, for a depleted surface,  $n_{ss}$  is determined by electron and hole emission by the surface states, and the following rate equation applies:

$$\frac{dn_{ss}}{dt} = e_p(N_{ss} - n_{ss}) - e_n n_{ss} \quad (5-2)$$

where  $N_{ss}$  is the density per unit energy per unit area of surface states at energy  $E$ , and the electron and hole emission rates  $e_n$  and  $e_p$  are given by

$$e_n = \sigma_n v_{th} n_i \exp[(E - E_i)/kT] \quad (5-3)$$

$$e_p = \sigma_p v_{th} n_i \exp[-(E - E_i)/kT] \quad (5-4)$$

In these expressions,  $\sigma_n$  and  $\sigma_p$  are the electron and hole capture cross sections,  $v_{th}$  is the carrier thermal velocity,  $n_i$  is the intrinsic carrier concentration, and  $E_i$  is the intrinsic energy. The energy scale is chosen such that  $E = 0$  corresponds to the valence band edge. Equation (5-2) is solved subject to the initial condition that  $n_{ss}(E, 0) = 0$ , and the resulting expression for  $G$  is

$$G(E, t) = \sigma_n \sigma_p v_{th}^2 n_i^2 N_{ss} \frac{[1 - \exp(-Pt)]}{P} \quad (5-5)$$

where

$$P(E) = n_i v_{th} \{ \sigma_p \exp[-(E - E_i)/kT] + \sigma_n \exp[(E - E_i)/kT] \} \quad (5-6)$$

Figure 5-5 is a plot of the function  $G$  normalized to its peak value at  $t \rightarrow \infty$ , for the case where  $N_{ss}$  is independent of  $E$ , and illustrates the well-known fact that states lying near midgap are the dominant sources of free-carrier generation. The important feature of this plot for CCDs is that the generation rate requires several milliseconds at  $T = 300$  K to recover to its steady-state value. This suggests that carrier generation can be suppressed to a low value in a CCD by periodically shuffling the charge packets back and forth between gates within a cell, provided each gate holds the charge for a time that is short in comparison with the recovery time.

We have performed measurements on a CCD that confirm the theory described above. The device is a  $420 \times 420$ -pixel, three-phase, triple-polysilicon imager which has been described in detail elsewhere.<sup>8</sup> For the device used in the measurements, a gate voltage below  $-4$  V was sufficient to invert the surface, and gate voltages of  $-7$  and  $+2$  V were used for the low and high levels. The measurement procedure consisted of holding phases 1 and 3 low (in inversion), while phase 2 was high and collected dark current. Periodically, the charge would be transferred to phase 1 and then returned to phase 2. During this transfer, the surface under phase 2 would momentarily invert and the generation rate would be forced to zero. After the transfer, the phase 2 surface would return to a depleted condition and the generation process would begin its recovery. We measured the average dark current  $J_D$  at various temperatures as a function of the time between transfers, and the results are shown in Figure 5-6. The calculated curve is given by the following expression:

$$J_D = \frac{1}{T_0} \int_0^{T_0} J_D(t) dt + J_{bulk} = \frac{q}{T_0} \int_0^{T_0} \int_0^{E_g} G(E, t) dE dt + J_{bulk} \quad (5-7)$$

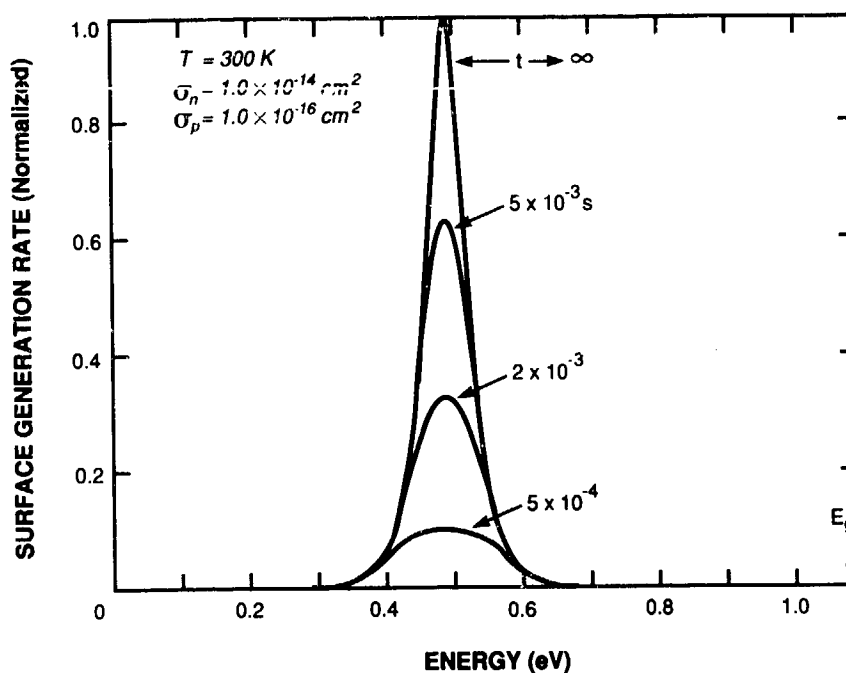


Figure 5-5. Normalized surface-state generation rate vs surface-state energy in the forbidden gap for various values of time after the surface is switched from inversion to depletion. Energy is measured from the valence-band edge.

where  $T_0$  is the time between transfers, and  $q$  is the electron charge. For short values of  $T_0$  only the bulk dark current  $J_{\text{bulk}}$  is present, while at long  $T_0$  the dark current asymptotically approaches the steady-state value of the surface-state dark current under phase 2 plus  $J_{\text{bulk}}$ . It can be shown that the integral of  $G(E, t)$  over the bandgap produces an expression containing only the geometric mean of the capture cross sections  $\sigma = \sqrt{\sigma_n \sigma_p}$  and not the individual cross sections  $\sigma_n$  and  $\sigma_p$ . The expression for  $J_D$  then contains only three adjustable parameters: the bulk dark-current density  $J_{\text{bulk}}$ , the midgap surface-state density  $N_{\text{ss}}$ , and the product  $\sigma n_i v_{\text{th}}$ . We used  $v_{\text{th}} = 1.0 \times 10^7$  cm/s, as is usually assumed<sup>9</sup>;  $n_i = 3.10 \times 10^{16} T^{1.5} \exp(-0.603/kT)$  cm<sup>-3</sup>, where  $T$  and  $kT$  are in units of K and eV, respectively<sup>10</sup>; and treated  $\sigma$  as the adjustable parameter. We were able to obtain a good fit between theory and experiment at all temperatures by using  $N_{\text{ss}} = 1.11 \times 10^9$  cm<sup>-2</sup> eV<sup>-1</sup>,  $\sigma = 1.0 \times 10^{-15}$  cm<sup>2</sup>, and determining  $J_{\text{bulk}}$  by matching the data at small  $T_0$  for each temperature.

The results of Figure 5-6 show that this technique can substantially reduce device dark current. For the device used in these measurements, the dark current at room temperature was reduced from 200 pA/cm<sup>2</sup> without the transfer process, to the bulk dark-current level of 20 pA/cm<sup>2</sup> with transfers occurring every 100  $\mu$ s or less. When all three phases are in depletion, the dark current increases to 600 pA/cm<sup>2</sup>, so a factor-of-30 reduction is gained by eliminating surface-generated dark current. The data also show that, as the temperature is decreased, the value of  $T_0$  needed to suppress surface-state dark current increases rapidly. This is a consequence of the strong temperature dependence of  $n_i$  in

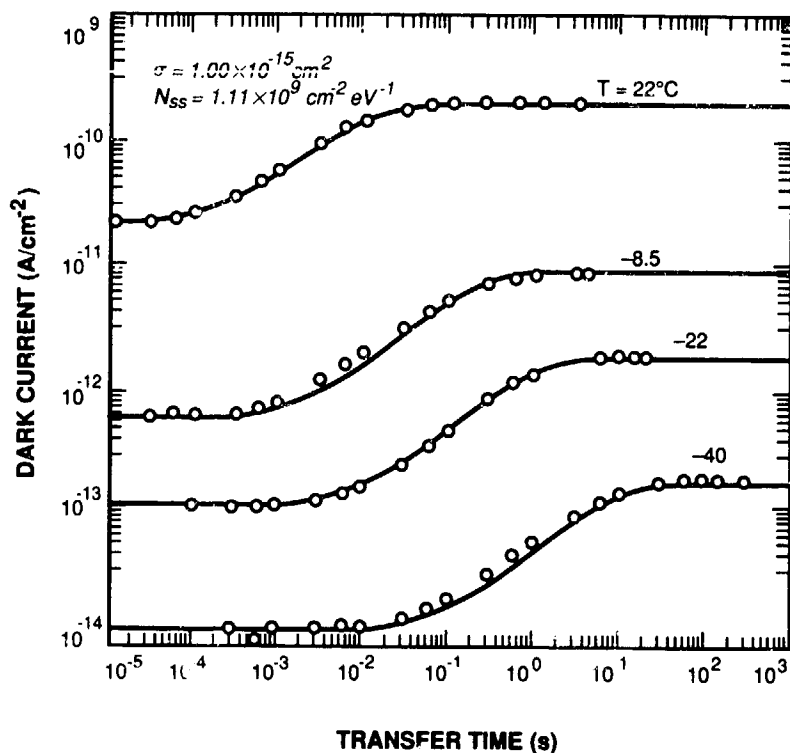


Figure 5-6. Measured and calculated dark current from a three-phase CCD imager vs time that one phase spends in depletion with the remaining two phases in inversion.

the function  $P(E)$  which determines the recovery rate of  $G(E,t)$ . Many scientific and military applications of CCD imagers require operation at low temperatures, and the results here show that at  $-40^\circ\text{C}$  the charge shuffling need be done at rates of only 10 times per second to maintain bulk-limited dark current.

B.E. Burke  
S.A. Gajar

### 5.3 PERMEABLE BASE TRANSISTOR TRACK-AND-HOLD CIRCUITS

Multiple wideband track-and-hold circuits are required to record the transient output of a superconductive chirp-transform spectrum analyzer. This transient recorder and a high- $T_c$  thin-film superconductive circuit will be integrated on a single GaAs substrate cooled to a temperature of 50 K. Each track-and-hold circuit consists of a very fast switch, a hold capacitor, and input and output impedance buffering stages. The permeable base transistor (PBT) with its low on-state resistance and fast switching speed is an ideal candidate for this application. The initial goals for the PBT track-and-hold portion of the program are to evaluate existing PBTs as candidates for this function

and to design, build, and test hybrid track-and-hold circuits using existing discrete PBTs to perform input and output impedance buffering functions as well as the switching function. The performance specifications for the spectrum analyzer are a 2.6-GHz bandwidth, a 45-MHz frequency resolution, and a 45-dB dynamic range at a 50-K operating temperature.

A basic track-and-hold circuit is shown in Figure 5-7. During the time that the switch is on, the voltage on the hold capacitor tracks the input voltage waveform. At a particular point in time, the switch is turned off. If the transition time of the switch between its on and off states is much shorter than the time taken for a significant change of the input waveform, then the voltage existing on the hold capacitor after turnoff is a representation of the input voltage at the instant the switch is turned off. The voltage on the hold capacitor remains approximately constant during the period that the switch is off, and can be measured or otherwise processed by circuits following the output buffer. A typical track-and-hold sequence is shown in Figure 5-8. Multiple track-and-hold circuits, which are triggered in such a way as to provide hold voltages at  $N$  increments of time along the input waveform, can be used to produce an  $N$ -sampled output representation of the input waveform.

Candidate PBTs were characterized using a dc current-voltage parameter analyzer, both at room temperature and 50 K. Measurements of the device's on- and off-mode resistance were made with the collector-emitter voltage both positive and negative. Typical results at 50 K obtained on PBTs from wafer Spare 1 are shown in Table 5-1. Parameters required to define PBTs in the circuit simulation program SPICE were obtained by linear-regression fitting of measured dc PBT characteristics to the equations defining the MESFET model in SPICE. As is true for all three-terminal semiconductor devices, the internal capacitances of the PBT vary nonlinearly with terminal voltages. For a circuit-simulation program, such as SPICE, to accurately predict the performance of a highly nonlinear circuit such as a track-and-hold, information about this variation must be obtained. The large-signal nonlinear behavior of the device capacitance can be determined from a series of small-signal measurements. By making small-signal S-parameter measurements for each of a series of

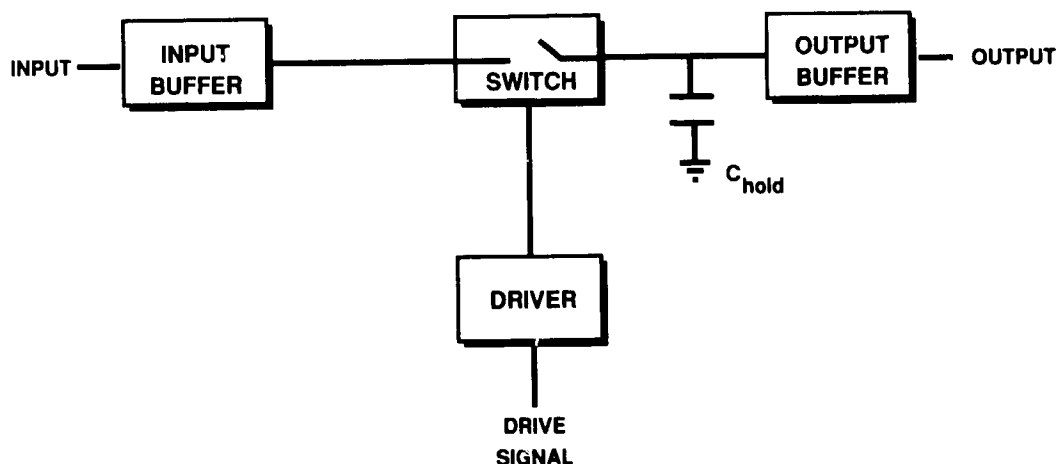


Figure 5-7. Basic track-and-hold circuit.



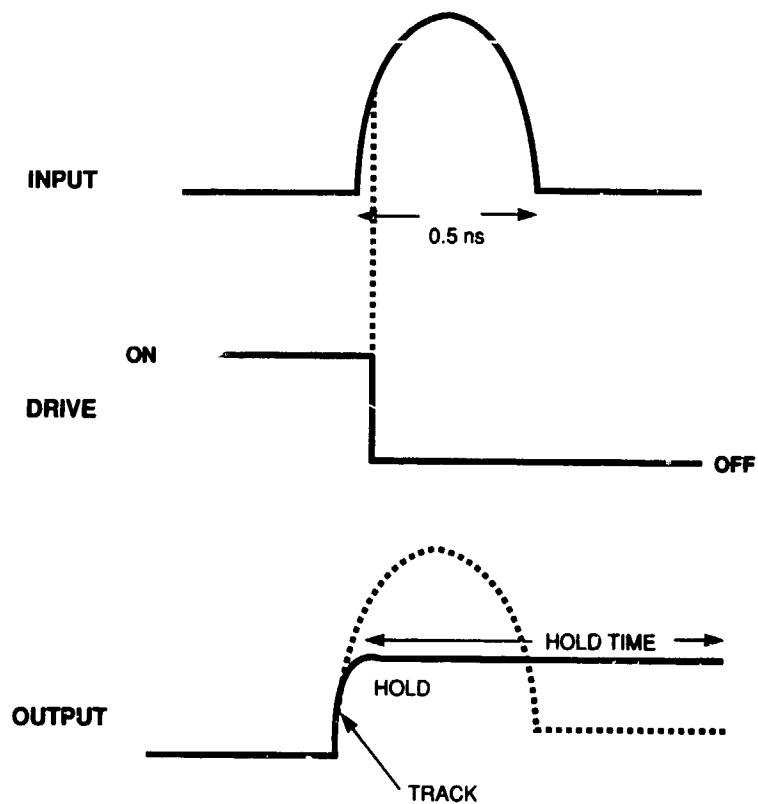


Figure 5-8. Track-and-hold waveforms.

<b>TABLE 5-1</b> <b>Typical Results at 50 K for PBTs</b> <b>from Wafer Spare 1</b>	
$R_{\text{ON}}$	$(V_{\text{BE}} = +0.5 \text{ V}) \sim 4.5 \Omega$
$R_{\text{OFF}}$	$(V_{\text{BE}} = -1.6 \text{ V}) > 1 \text{ M}\Omega$
$I_{\text{C}}$	$(V_{\text{BE}} = -1.6 \text{ V}) \sim -0.2 \mu\text{A}$

different dc voltages on the device terminals, the variation of the internal device capacitance was determined as a function of those voltages. SPICE simulations were used to investigate various circuit configurations. One goal of these simulations was to understand the degradation of the signal due to parasitic feedthrough associated with the PBT and to determine the adequacy of the present PBT design for this track-and-hold circuit application. Circuit techniques for conditioning the switch-control signal were also studied.

Two versions of a microstrip hybrid track-and-hold circuit (H1 and H2) have been designed and fabricated. Both were packaged in an existing test fixture which could also accommodate a superconducting companion circuit. The track-and-hold circuits consist of three parts: the input buffer, the switch, and the output buffer. The input-buffer circuit performs two roles. It provides a low source resistance to the switch, and it reduces the loading of the individual track-and-hold circuits on the detected output from the superconducting circuit. Circuit H1 used a resistive divider to achieve the first goal. Its source resistance was  $5\ \Omega$ , about the same resistance as the switch in the on-state. The performance of the divider, however, varied with frequency within the tracking bandwidth of the circuit, probably due to the lengths of transmission lines connecting the various components. This situation was remedied in the second hybrid circuit, H2, shown schematically in Figure 5-9, where an emitter-follower circuit was employed to provide both a low source resistance to the switch and a high impedance at the input.  $50\text{-}\Omega$  microstrip lines were used to couple both the input signal and the track-and-hold drive signal to the base of the respective PBTs. Since the impedance looking into the base of a PBT is high, a  $50\text{-}\Omega$  terminating resistance was provided to reduce the reflections on these lines. Both H1 and H2 used a single PBT as a switch whose on- or off-state is controlled by the track-and-hold drive signal applied to the base, and both had the same output emitter-follower buffer circuit.

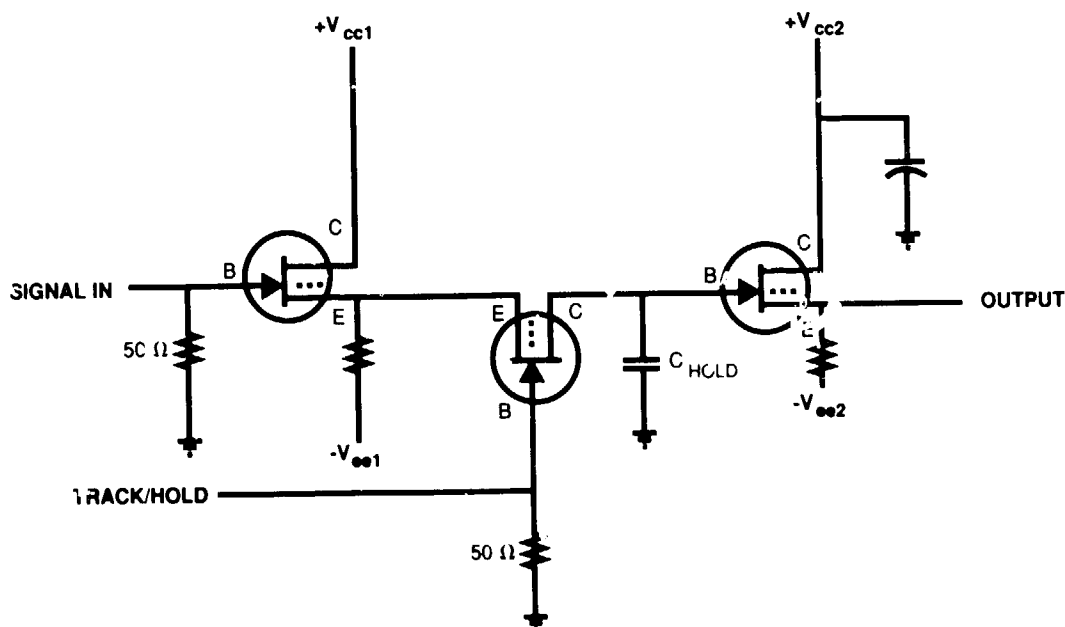


Figure 5-9. Schematic of track-and-hold circuit H2.

The hybrid track-and-hold circuits were fabricated on 0.5-mm alumina substrates to be compatible with the cryogenic fixture available; one side of the substrate had a wraparound ground. Thin film resistors were epoxied in place and wire-bonded to the circuit. The PBTs were soldered down and mesh bonds connected the PBT bonding pads to the circuit. Finally, a ceramic hold capacitor was attached to the circuit using conductive epoxy. Photographs of circuit H2 are shown in Figure 5-10.

Measurements were made on circuit H2 in the time domain with both standard and sampling oscilloscopes. By examining the trace during times associated with the hold mode, the circuit could be evaluated in terms of ripple due to reflections on various lines, droop, and feedthrough. The minimum track time required was measured to be  $<1$  ns. Droop was not measurable. Because of the nature of the present circuit needs, feedthrough and its effect on isolation may not be an issue. The signal to be sampled is present for approximately 38 ns, followed by a quiescent period of equal time. The A/D conversion, or a second sampling process, can occur during the quiescent period when there is no signal to feed through.

Scalar measurements in the frequency domain indicated a tracking bandwidth of 2.4 GHz for hybrid circuit H2, as shown in Figure 5-11. A dynamic range of approximately 30 dB was obtained from spectrum-analyzer measurements shown in Figure 5-12. In addition, cryogenic measurements in both the time and frequency domains (spectrum analyzer) were made on H2 while it was submerged in liquid nitrogen.

Existing discrete PBTs have been shown to be suitable candidates for use in track-and-hold circuits and are close to meeting the performance requirements for the proposed spectrum analyzer. However, oscillations occurred for a certain range of bias points, including biases that appeared to be desirable operating points. The reported results were taken at nonoscillating bias points. A new layout of the circuit, H3, will spread out circuit elements which on H2 were quite close together. This should reduce coupling between circuit elements. Work will commence to implement a monolithic version of circuit H3. Initial designs will use identical PBTs for switching and buffer functions.

Because of the cryogenic nature of the present application, power consumption is a primary concern. To implement a spectrum analyzer based on the proposed technology would involve perhaps 64 identical track-and-hold circuits operating at 50 K. The thermal load due to excessive power consumption could easily overwhelm the capacity of the cooling system. While preliminary hybrid designs involving single track-and-hold circuits for concept testing are able to dissipate several hundred milliwatts of power even in a cooled environment, the planned monolithic circuits that will have multiple track-and-hold cells must probably dissipate less than 10 mW per cell to be usable in a low-capacity cryogenic cooler. This would seem to imply that circuit complexity must be minimized. Low power consumption may be the most difficult requirement to meet.

B.J. Clifton	M.A. Hollis
R.H. Mathews	R.A. Murphy

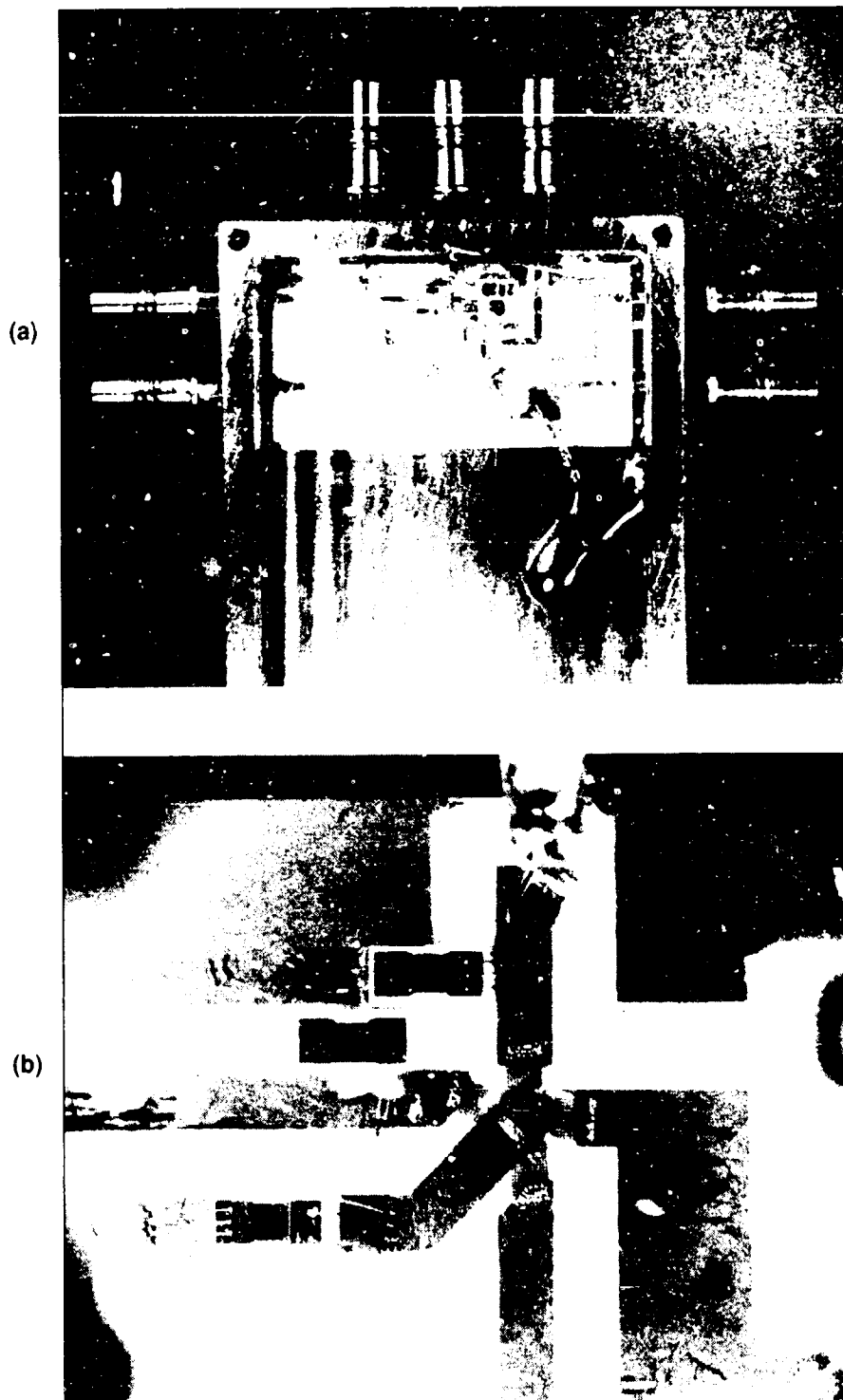


Figure 5-10. (a) Track-and-hold circuit H2 in cryogenic test fixture, and (b) closeup of H2.

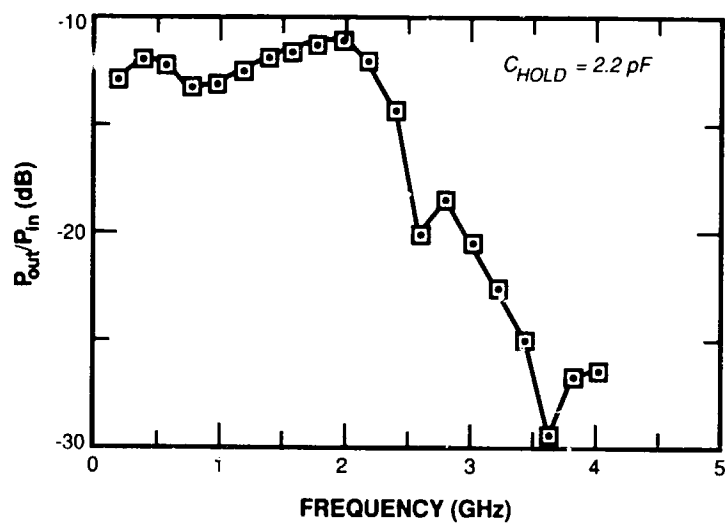


Figure 5-11. Tracking bandwidth of circuit H2 in sampling mode.

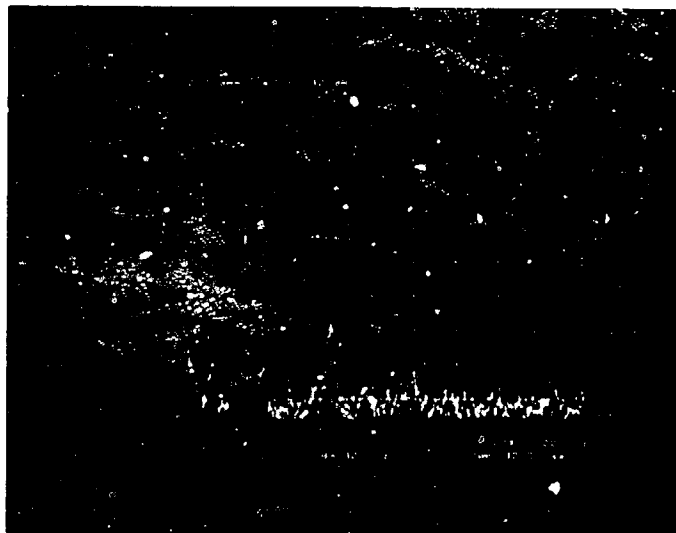


Figure 5-12. Spectrum-analyzer data for circuit H2.

## REFERENCES

1. R.R. Parenti, Proc. SPIE **1000**, 101 (1988).
2. Solid State Research Report, Lincoln Laboratory, MIT (1988:4), p. 47, DTIC AD-A209969.
3. *Ibid.* (1988:2), p. 51, DTIC AD-A204718.
4. C.M. Huang, B.E. Burke, B.B. Kosicki, R.W. Mountain, P.J. Daniels, D.C. Harrison, G.A. Lincoln, N. Usiak, M.A. Kaplan, and A.R. Forte, Proceedings of the International Symposium on VLSI Technology, Systems, and Applications, 17-19 May 1989, Taipei, Taiwan (IEEE Catalog No. 89-CH2631-0), p. 98 (1989).
5. N.S. Saks, J. Appl. Phys. **53**, 1745 (1982).
6. J. Janesick, T. Elliott, R. Bredthauer, C. Chandler, and B. Burke, Proc. SPIE **982**, 70 (1988).
7. D.G. Ong and R.F. Pierret, IEEE Trans. Electron Devices **ED-22**, 593 (1975).
8. B.E. Burke, R.W. Mountain, P.J. Daniels, and D.C. Harrison, Opt. Eng. **26**, 896 (1987), DTIC AD-A187551.
9. R.F. Pierret and G.W. Neudeck, *Modular Series on Solid State Devices* (Addison Wesley, Reading, Massachusetts, 1987), Vol. VI, p. 158.
10. H.D. Barber, Solid-State Electron. **10**, 1039 (1967).

## 6. ANALOG DEVICE TECHNOLOGY

### 6.1 LOW-LOSS SUBSTRATES FOR HIGH-TEMPERATURE SUPERCONDUCTORS

The newly discovered copper-oxide superconductors afford the exciting possibility of superconductor applications at liquid-nitrogen temperatures. These high-temperature superconductors (HTS) will require compatible substrate materials for thin-film deposition if any of the envisioned electronic applications are to be brought to fruition. In particular, microwave devices require a low loss dielectric material with a reasonably low loss tangent and a frequency-independent dielectric constant. Several candidate materials with attractive properties have appeared in the literature. The perovskites lanthanum gallate ( $\text{LaGaO}_3$ ) (see Reference 1) and lanthanum aluminate ( $\text{LaAlO}_3$ ) (see Reference 2) provide a good lattice match to the HTS  $\text{Y}_1\text{Ba}_2\text{Cu}_3\text{O}_x$  (but with desirable compressive HTS film stress), can be grown in large crystal sizes, are compatible with high-temperature film processing, and have a good thermal expansion match to  $\text{Y}_1\text{Ba}_2\text{Cu}_3\text{O}_x$ . High critical current ( $J_c > 10^6 \text{ A/cm}^2$ ) films of  $\text{Y}_1\text{Ba}_2\text{Cu}_3\text{O}_x$  have been demonstrated on both substrate materials. However, no data have been published on the microwave properties of  $\text{LaGaO}_3$ , and conflicting reports have appeared on the microwave properties of  $\text{LaAlO}_3$  (see References 2 and 3). Furthermore, these perovskite materials undergo structural phase transitions at high temperature and therefore often grow as heavily twinned crystals. The potential effects of twinning on HTS films and circuit fabrication required a close examination.

The current growth technique for these materials is Czochralski, and a surface suitable for epitaxial deposition is obtained using colloidal silica (Syton) polish. Substrates were obtained commercially as 1.0-in-diam., 500- $\mu\text{m}$ -thick wafers of  $\text{LaGaO}_3$  and 1.5-in-diam., 550- $\mu\text{m}$ -thick wafers of  $\text{LaAlO}_3$ . These substrates were then cut into the  $0.9 \times 0.5$ -in rectangles required for microwave characterization. Microwave dielectric properties were measured using a stripline resonator technique previously used to measure the surface resistance of  $\text{Y}_1\text{Ba}_2\text{Cu}_3\text{O}_x$  films.<sup>4</sup> For this study, niobium was deposited on the perovskite substrate materials. The low loss of the superconducting niobium at 4.2 K and its known quality factor allowed the small values of the dielectric loss tangent to be extracted as a function of frequency from the measured resonator quality factors. Since these dielectrics do not have a cubic lattice structure, the dielectric constant may be anisotropic. Measurements of the resonant frequencies of stripline resonators on such crystals, especially heavily twinned crystals such as those used in this study, will yield an effective dielectric constant which is an average of the dielectric constants along the principal crystallographic axes.

Values of the effective relative dielectric constant as a function of frequency obtained from such measurements are shown in Figure 6-1. The values are essentially frequency independent with mean values of 25.0 for  $\text{LaGaO}_3$  and 24.5 for  $\text{LaAlO}_3$ . This result for  $\text{LaGaO}_3$  agrees well with the reported value at 1 MHz (Reference 1), but the result for  $\text{LaAlO}_3$  is much larger than the first reported value of 15.3 (Reference 2) and in good agreement with a value of 26.0 inferred from transmission line measurements.<sup>3</sup> Measured values of the loss tangent are shown in Figure 6-2. The values are in the low  $10^{-6}$  range and are almost independent of frequency. The loss tangent results demonstrate that these materials are excellent dielectrics with low loss characteristics.

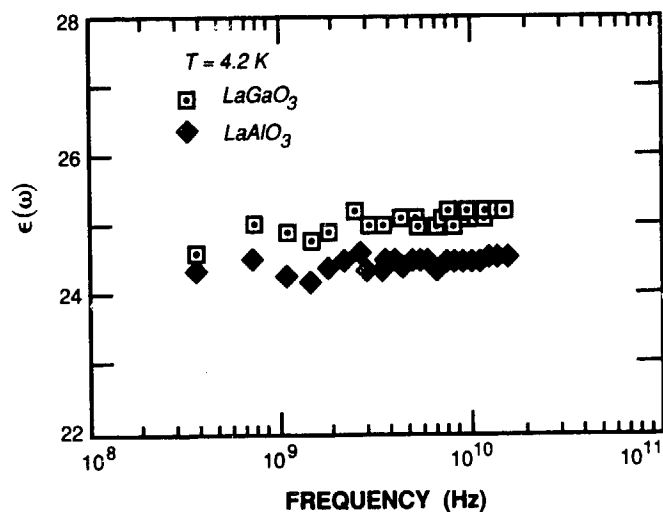


Figure 6-1. Relative dielectric constant as a function of frequency for  $\text{LaAlO}_3$  and  $\text{LaGaO}_3$  measured at 4.2 K with a stripline resonator.

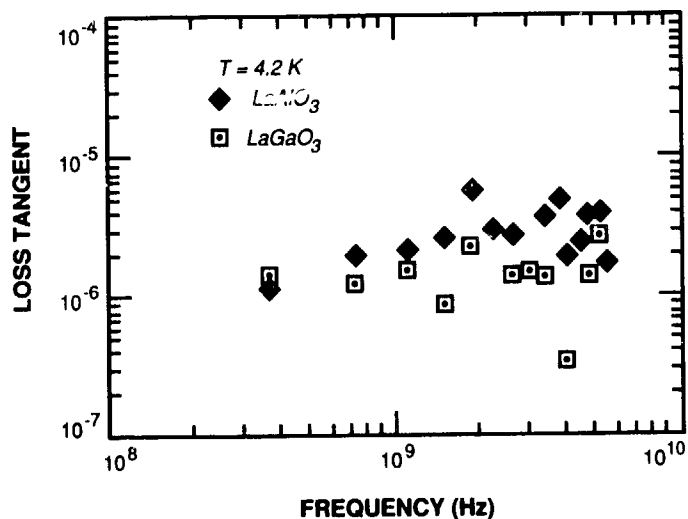


Figure 6-2. Dielectric loss tangent as a function of frequency for  $\text{LaAlO}_3$  and  $\text{LaGaO}_3$  measured at 4.2 K with a stripline resonator.



Twinning formation and motion of twins occur in both  $\text{LaAlO}_3$  and  $\text{LaGaO}_3$  because of lattice instability and corresponding structural phase transitions. A transition from rhombohedral to cubic takes place at  $435^\circ\text{C}$  in  $\text{LaAlO}_3$ , and a transition from orthorhombic to rhombohedral takes place at  $150^\circ\text{C}$  in  $\text{LaGaO}_3$ . Figure 6-3 clearly shows the twins that appear in as-grown  $\text{LaGaO}_3$  substrates. In order to characterize the effects of twins and twin motion on surface roughness, a high-temperature ( $850^\circ\text{C}$ ) annealing study was performed on the polished substrates alone. Optical micrographs and Dektak surface profiles were used to characterize the surfaces before and after annealing. The



Figure 6-3. Photograph taken in transmitted light of a (100)-oriented  $\text{LaGaO}_3$  substrate showing the twin planes perpendicular to the substrate surface.

annealing study revealed significant twin motion and surface structure for both materials after heating above the phase transitions. At  $850^\circ\text{C}$ , steps were generated in the surface as large as  $1\ \mu\text{m}$ , but the steps were not very abrupt, having a maximum aspect ratio of 0.01 (vertical/lateral dimension). Because of the small aspect ratio, circuit fabrication should not be inhibited. Based on changes observed with the optical microscope, the steps appeared to correspond to regions of the crystal where the twin planes, whose intersections with the crystal surface had initially been polished flat, were partially annealed out. Typical surface roughness generated by the steps was on the order of 200 nm. HTS film quality may be degraded somewhat by twin motion in the underlying substrate, and substrate twins are reportedly replicated in HTS films, reducing the critical current of the superconductor.<sup>5</sup> Twin formation has been reported to be significantly reduced in doped gallate substrates (e.g.,  $\text{La}_{0.95}\text{Gd}_{0.05}\text{GaO}_3$ ) (see Reference 5). Doping serves the dual role of increasing the structural phase transition temperature and pinning in place any twins that develop.<sup>6</sup> Current efforts in crystal growth of these materials are focusing on doping.

W.G. Lyons

## 6.2 MULTITARGET COSPUTTERING OF $Y_1Ba_2Cu_3O_x$ SUPERCONDUCTING FILMS

Superconducting films of  $Y_1Ba_2Cu_3O_x$  have been deposited by multitarget cosputtering from the elemental targets of Y, Ba, and Cu in a partial pressure of oxygen. Figure 6-4 shows a schematic of the sputtering system. Multitarget sputtering offers the distinct advantage of independent control over the composition of each of the components of the 123 compound. The importance of maintaining independent control over each of the sputtering rates becomes evident when one considers that the sticking coefficients of these elements is dependent on such parameters as substrate temperature and type of substrate. The flexibility offered by multitarget sputtering is therefore extremely useful in thin-film studies where control over processing variables is required.

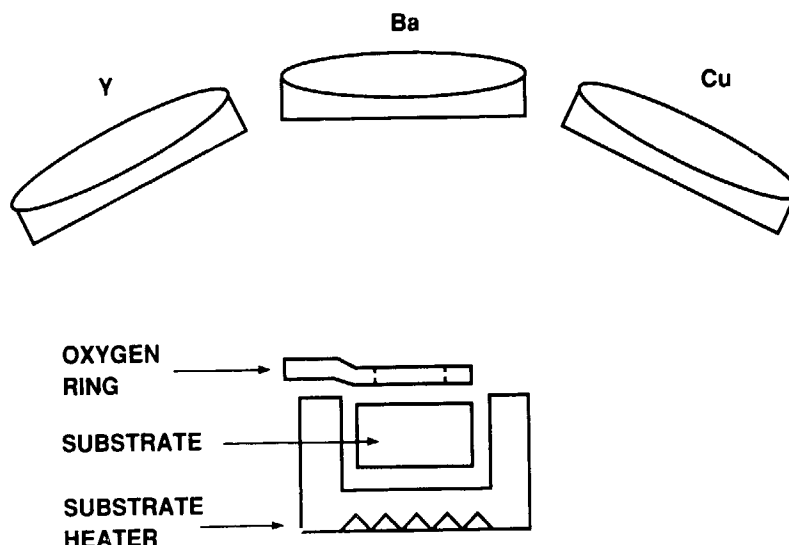


Figure 6-4. Schematic of multitarget cosputtering system for deposition of superconducting  $Y_1Ba_2Cu_3O_x$  films.

The limitations to this technique stem mostly from the reactivity of Ba and Y with oxygen. In the presence of oxygen, the sputtering rate from the Ba target becomes small and unstable. The sputtering rate from the Y target actually approaches zero in the presence of oxygen. In the latter case, we believe that the large secondary-electron yield from  $Y_2O_3$  contributes to lowering the plasma impedance around the target to a point where the target voltage is less than the threshold voltage for sputtering. For these reasons, it is necessary to maintain a low partial pressure of oxygen at the target.

The three magnetron targets are operated in the RF mode, with the three power supplies phase-locked to eliminate the possibility of plasma interactions between the targets. The sputtering ambient is argon, typically at pressures of 2 to 3 mTorr. The substrates are heated using a radiant heater located directly below the substrate. To maintain a low partial pressure of oxygen in the chamber,  $O_2$  is injected locally near the substrate so that a relatively higher pressure of oxygen is above the

substrate. Effective pumping by the cryopump helps to prevent the oxygen from reaching the targets, but naturally there is a maximum pressure limit set by the system geometry and the oxygen pumping speed. The films are annealed after deposition for 1 h at 850°C in flowing oxygen to crystallize the superconducting phase.

The effects of substrate temperature on the dc electrical characteristics of multitarget-sputtered 123 films have been studied for substrate temperatures between 460° and 690°C. Figure 6-5 shows the resistivity-vs-temperature curve for a sample deposited at a temperature of 680°C. The curve shows a semiconductor-like behavior above the transition, and a rather broad transition to zero resistance. X-ray diffraction data for this sample show the coexistence of the superconducting phase with such unwanted phases as  $\text{BaCuO}_2$  and the semiconducting  $\text{Y}_2\text{Ba}_1\text{Cu}_1\text{O}_5$ , also known as the "211" or "green" phase.

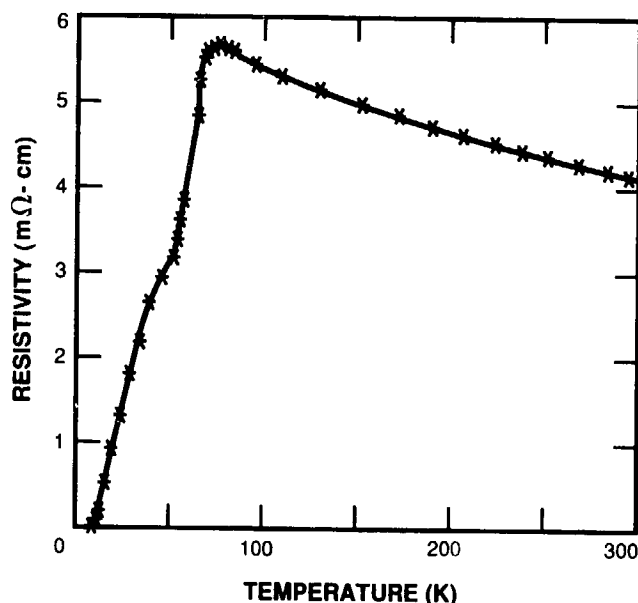


Figure 6-5. Resistivity vs temperature ( $\rho$  vs  $T$ ) curve for Y-Ba-Cu-O film deposited at a substrate temperature of 680°C. The semiconductor-like trend above the transition is attributed to the presence of the  $\text{Y}_2\text{Ba}_1\text{Cu}_1\text{O}_5$  "green" phase.

Films deposited at a slightly lower substrate temperature of 600°C show a more metal-like behavior above the transition, as can be seen in Figure 6-6. The transition becomes narrower, although a significant foot is present which lowers the  $T_c$  (at  $\rho = 0$ ) to approximately 50 K.

A drastic reduction of the substrate temperature to a value of 460°C causes a dramatic improvement in the electrical characteristics, as is evident in Figure 6-7. The transition becomes extremely sharp with a  $T_c$  (at  $\rho = 0$ ) of approximately 88 K. Figure 6-8 shows the behavior of the critical current density  $J_c$  and resistivity as a function of temperature for a film deposited at a temperature of 495°C. At 4 K, the value of  $J_c$  is approximately  $10^6$  A/cm<sup>2</sup>.

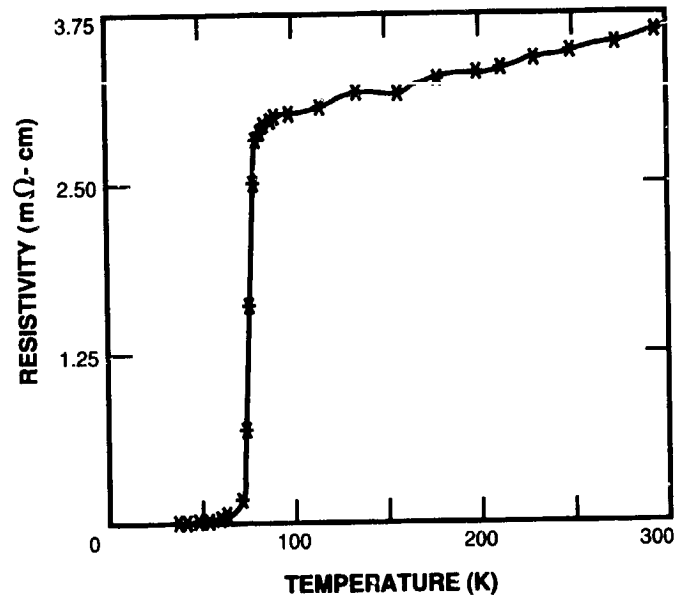


Figure 6-6.  $\rho$  vs  $T$  curve for a Y-Ba-Cu-O film deposited at 600°C.

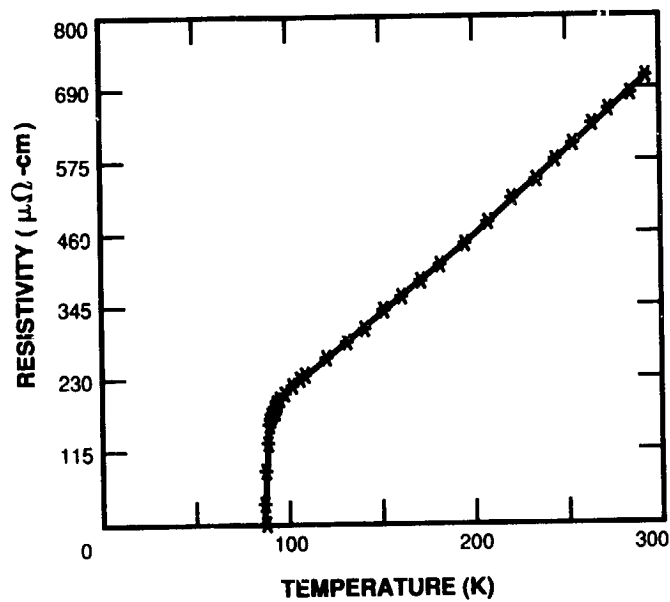


Figure 6-7.  $\rho$  vs  $T$  curve for a Y-Ba-Cu-O film deposited at 460°C. Lower substrate temperatures prevent the formation of unwanted phases.

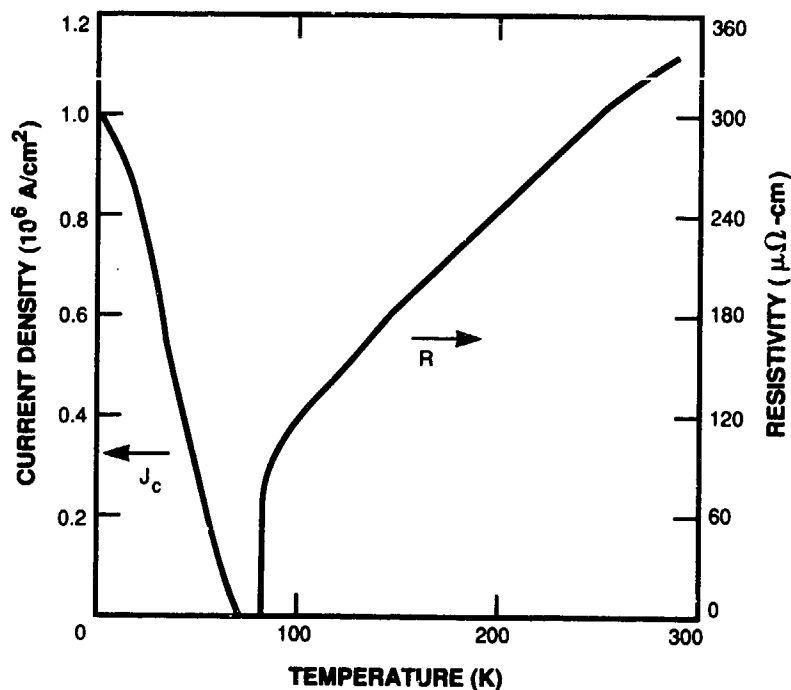


Figure 6-8.  $J_c$  and  $\rho$  vs  $T$  curves for a Y-Ba-Cu-O film deposited at 495°C.  $J_c \approx 10^6$  A/cm $^2$  at 4 K.

The improvement in the electrical properties of the 123 films as the substrate temperature is lowered can be understood by referring to the stability diagram for this material in the presence of  $O_2$ . Figure 6-9 is adapted from work by Bormann and Nölting<sup>7</sup> which shows the line of stability for the perovskite phase. Also shown is the line for the maximum  $O_2$  pressure tolerable for stable target operation. To the left of the line, the perovskite structure cannot form because of the lack of oxygen necessary to stabilize that phase. However, unwanted phases such as  $BaCuO_2$  and the 211 are kinetically favored to form under those conditions. Operation to the right of the line ensures the stability of the perovskite phase, although the actual formation of this phase also requires adequate heating of the film to provide sufficient atom mobility to prevent an amorphous state from being quenched in.

For the case of multitarget sputtering from the elements, operation is confined to the region below the maximum allowable  $O_2$  pressure. Substrate temperatures to the left of the line of stability result in curves similar to that in Figure 6-5, where there was sufficient heating to form crystalline phases but insufficient oxygen to form the superconducting perovskite phase. Substrate temperatures to the right of the line of stability result in amorphous films which crystallize to the superconducting phase upon annealing at 850°C. Under the present  $O_2$  pressure limitations, it is not possible during deposition to form the crystalline perovskite phase without also forming the unwanted 211 and  $BaCuO_2$  phases.

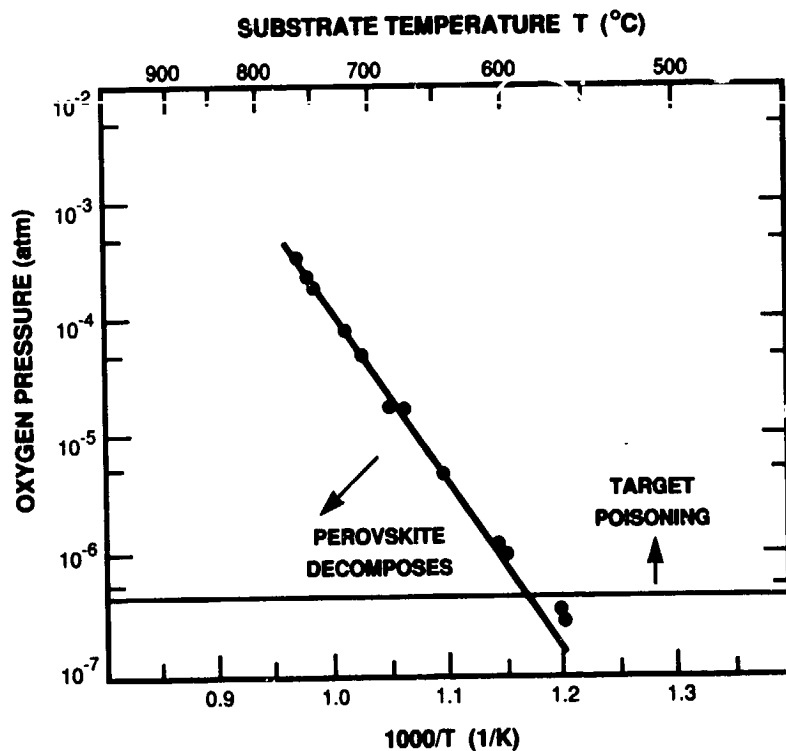


Figure 6-9. Critical oxygen partial pressure for the decomposition of the perovskite structure. The horizontal line marks the maximum oxygen pressure tolerable for sputtering from elemental Ba and Y targets. (Adapted from Reference 7.)

The use of activated or excited oxygen in the form of ozone or atomic oxygen is currently being evaluated in an effort to move the line of stability for the perovskite to higher temperatures, so that for the same oxygen pressures the perovskite is stable in a temperature range in which crystallization of the film is possible.

L.S. Yu-Jahnes  
A.C. Anderson

## REFERENCES

1. R.L. Sandstrom, E.A. Giess, W.J. Gallagher, A. Segmüller, E.I. Cooper, M.F. Chisholm, A. Gupta, S. Shinde, and R.B. Laibowitz, *Appl. Phys. Lett.* **53**, 1874 (1988).
2. R.W. Simon, C.E. Platt, A.E. Lee, G.S. Lee, K.P. Daly, M.S. Wire, J.A. Luine, and M. Urbanik, *Appl. Phys. Lett.* **53**, 2677 (1988).
3. M.C. Nuss, P.M. Mankiewich, R.E. Howard, B.L. Straughn, T.E. Harvey, C.D. Brandle, G.W. Berkstresser, K.W. Goossen, and P.R. Smith, *Appl. Phys. Lett.* **54**, 2265 (1989).
4. M.S. DiIorio, A.C. Anderson, and B-Y. Tsaur, *Phys. Rev. B* **38**, 7019 (1988).
5. G. Koren, A. Gupta, E.A. Giess, A. Segmüller, and R.B. Laibowitz, *Appl. Phys. Lett.* **54**, 1054 (1989).
6. E.A. Giess, private communication.
7. R. Bormann and J. Nölting, *Appl. Phys. Lett.* **54**, 2148 (1989).

